CENTRO DE INVESTIGACIONES
EN ÓPTICA, A.C.

Fiber optic Fabry-Perot interferometer for contactless sensing

DOCTORADO EN CIENCIAS (ÓPTICA)

Asesores: Dr. David Monzón Hernández

Prof. Joel Villatoro

Estudiante: José Carlos Moreno Hernández

Octubre de 2016
León, Guanajuato, México

A mis padres, a Elisa y Julia.

ACKNOWLEDGEMENTS

I want to express my gratitude to all the people who helped me to complete this work. First to my main advisor Dr. David Monzón that gave me the chance to propose and develop this project, product of an extraordinary teamwork always encouraging me to achieve a better understanding of what scientific research should be. Dr. Joel Villatoro, my other advisor, that showed me the importance of being meticulous in manuscript writing, and being thorough in the experimental work at the laboratory. Dr. Alejandro Martínez for sharing the initial proofs of tapered fiber tips Fabry-Perot interferometers and for the useful discussions about the fiber effective refractive index evolution when tapering down optical fibers. Dr. Olivier Pottiez, for his optoelectronics course that was one of the most useful courses I have taken in my life. He showed me the theoretical path to understand optical fiber waveguides. Dr. David Moreno Hernández, for sharing his experience in Matlab programming, so i could make some of the simulations. M. Eng. Myriam Jiménez, for all the technical support concerning the equipment, but most importantly for being always willing to help. I want to thank Lic.Marlen Tenango for helping along this years, making the paperwork something ligther. And last but not least to the Engineering department, the Mechanics and Optical workshops for fabrication of fiber, sample holders and glass samples used along this project.

I want to show my gratitude to Consejo Nacional de Ciencia y Tecnología for the scholarship received to achieve this degree and to the Dirección de Formación Académica of this institution for the financial support to attend the conferences.

ABSTRACT

Since the publication of the paper where the first fiber Fabry-Perot interferometer(FFPI) for sensing applications was demonstrated, more than thirty years ago, a number of configurations of this optical fiber interferometer have been proposed and used to detect physical, chemical and biological variables. Years of fruitful research activity has proven that FFPI sensors have significant advantages, such as high sensitivity, resolution, miniature size, and versatility besides the intrinsic assets of fiber optics. For refractive index sensing, FFPI sensors proposed so far have a common drawback and this is that the optical fiber has to be in direct contact with the sample or the material used as a transducer. This characteristic of the FFPI sensors is a disadvantage hard to overcome in order to fabricate, miniature, repeatable, reliable, and simple-to-use fiber sensors.

This dissertation proposes and demonstrates a contactless FFPI refractometer for solid and liquid samples; providing the necessary insight to understand the operation principle of an FFPI and how this interferometer was improved by replacing the lead-in fiber with an optimized diameter tapered-down fiber tip. This FFPI structure enhancement in parallel with a custom interrogation software routine allowed to increase considerably the extrinsic FFPI air cavity to 80mm, such cavity lengths can only be achieved using beam collimating lenses. The increased size of the cavity makes it possible to introduce inside it easy-to-handle transparent glass samples, of a couple of millimeters thick, to obtain its refractive index, geometrical thickness, and the distance to the lead-in fiber tip simultaneously and in real time.

The simultaneous thickness and refractive index measurements capacity of the FFPI sensor here proposed allowed us to obtain the thermo-optic coefficient and the thermal-expansion coefficient of a polydimethylsiloxane (PDMS) block, of one-centimeter-thick.

Lately, PDMS is commonly used to fabricate microfluidic chips for biomedical diagnosis, point-of-care testing and biochemical detection.

The proposed method also worked for liquid samples, we were able to detect different water contents in ethanol achieving a limit detection level of 0.5%. This interferometric technique can be used to develop a simple method to detect biofuels adulteration due to the presence of water.

OUTLINE OF THE DISSERTATION

The first chapter describes the advantages offered by fiber optic sensors, which together with the development of optoelectronic components demanded by the fiber telecommunication companies during the last three decades have allowed, in recent years, the emergence of small fiber sensing companies. Fiber Bragg grating sensors represent one of the first successfully commercialized technology and are still the sensing technique most used for civil structure monitoring.

The second chapter describes the fundamentals of the fiber Fabry-Perot interferometer structure and how make it suitable to achieve contactless measurements, also is included a briefly description of some interrogation schemes, where spectrometric interrogation algorithms offer the possibility to obtain higher resolution and even the possibility of instantaneous measurements. The third chapter covers the theoretical and experimental details of SMF tapers, the effect of introducing a lead-in fiber taper tip in the extrinsic fiber Fabry-Perot interferometer and how the optimal fiber taper diameter can be calculated. Theoretical and experimental comparison between the fringe visibility of an un-tapered and tapered lead-in fiber tip in an EFPI is reported in chapter 4.

Chapters 5 ,6 contain a description of the contactless measurements achieved. Long-range displacement, refractive index, thickness for solid samples and how these lead to obtain the thermal expansion coefficient and thermo-optic coefficient of a commonly used polymer(polydimethylsiloxane).

In chapter 7 we demonstrated how our sensing system described is capable of detecting the refractive index changes of liquid (water-ethanol) solutions.

PUBLICATIONS

JOURNALS

1. ***Carlos Moreno-Hernandez****; David Monzón-Hernandez; and Joel Villatoro, “Contactless biofuel adulteration detection using an optical fiber interferometer,” Sens. And Act.:B (Submitted,2016)*

2. *Iván Hernández-Romano, Miguel A. Cruz-Garcia,* ***Carlos Moreno-Hernández****, David Monzón-Hernández, Efraín O. López-Figueroa, Omar E. Paredes-Gallardo, Miguel Torres-Cisneros, and Joel Villatoro, "Optical fiber temperature sensor based on a microcavity with polymer overlay," Opt. Express 24, 5654-5661 (2016). doi: 10.1364/OE.24.005654*

3. *Iván Hernández-Romano, David Monzón-Hernández,* ***Carlos Moreno-Hernández****, David Moreno-Hernandez, and Joel Villatoro,” Highly Sensitive Temperature Sensor Based on a Polymer-Coated Microfiber Interferometer,” Photonics Technology Letters, IEEE, vol.27, no.24, pp.2591-2594, 2015. doi: 10.1109/LPT.2015.2478790*

4. ***Carlos Moreno-Hernández****, David Monzón-Hernández, Iván Hernández-Romano, Joel Villatoro, “Single tapered fiber tip for simultaneous measurements of thickness, refractive index and distance to a sample “Opt. Express, 23, 22141-22148, (2015). doi: 10.1364/OE.23.022141*

5. ***Carlos Moreno-Hernández****, David Monzón-Hernández, Alejandro Martinez-Rios, David Moreno-Hernandez, Joel Villatoro, "Long-Range Interferometric Displacement Sensing with Tapered Optical Fiber Tips," Photonics Technology Letters, IEEE, vol.27, no.4, pp.379-382, 2015. doi: 10.1109/LPT.2014.2375651*

CONFERENCES

ORAL PRESENTATION

CLEO/ECEQ 2015
Carlos Moreno-Hernández, D. Monzón-Hernández, and J. Villatoro, *"Highly functional interferometer built with tapered optical fibre tips,"* in 2015 European Conference on Lasers and Electro-Optics - European Quantum Electronics Conference, (Optical Society of America, 2015), paper CH_6_2.

POSTER PRESENTATION

IBERSENSOR 2016 X Congreso Iberoamericano de Sensores
Carlos Moreno-Hernández; D. Monzón-Hernández; Joel Villatoro," "Optical Fiber Fabry-Perot interferometer sensor to differentiate Tequilas". (Accepted) Oct.2016

EWOFS2016
Carlos Moreno-Hernández; D. Monzón-Hernández; Joel Villatoro*," Contactless optical fiber refractive index sensor for liquid and solid samples,"* Proc. SPIE 9916, Sixth European Workshop on Optical Fibre Sensors, 99161A (May 30, 2016); doi:10.1117/12.2236554.

LAOP2014
Carlos Moreno-Hernández, D. Monzón-Hernández, A. Martinez-Rios, D. Moreno-Hernandez, and J. Villatoro, *"Fabry-Perot interferometer with enhanced visibility with tapered fiber tips,"* in Latin America Optics and Photonics Conference, OSA Technical Digest (online) (Optical Society of America, 2014), paper LM4A.51;
doi: 10.1364/LAOP.2014.LM4A.51

CONTENTS

1 INTRODUCTION

The research on fiber optic sensors began in the late 1970´s, after fiber transmission loss reached the unprecedented mark of 0.2dB/km[1]. Fiber optics technology has revolutionized the sensing and imaging fields due to fibers' small size, kilometer range lengths, and flexibility. These characteristics are remarkable for endoscopic imaging and sensing devices. The fabrication of extra-long length fibers allows to design sensors with large interaction lengths that results in high sensitivity, e.g., fiber Sagnac loop-based sensors. And it is also advantageous for fiber distributed sensing. On the other hand, fibers' reduced diameter allows point sensing (fiber Fabry-Perot interferometers). Since fiber optics emergence, operation principles, applications and even patents for fiber interferometers have been published for more than 3 decades [2-6].

1.1 *FIBER OPTIC SENSING*

The first commercial fiber optic sensors emerged soon after the fiber telecommunications bubble collapsed in the late 90´s. When some companies that where fabricating optoelectronic devices for telecommunications decided to invest in development of fiber optic sensors. Even though some companies went bankrupt, they paved the road for improving technologies and minimizing costs and sizes of optoelectronics such as semiconductor laser diodes and photodiodes designed for the fiber transmission windows (between 1260-1675nm) that will be essential for the emerging sensing systems.

Reliable components at lower prices have provided the favorable conditions for the creation of optical fiber sensors companies first devoted to measure physical parameters, and some years later to chemical or even biological parameters detection [7-10]. Fiber optic sensors take advantages of optical fibers inherent properties, such as:

- *Immunity to electromagnetic interference*
- *High sensitivity*
- *Small size*
- *Capability of multiplexing*
- *Lightweight*
- *Passive (all dielectric)*
- *Complementary to telecom and its optoelectronics*
- *Harsh environment resistant*

Even though this advantages have raised the interest on this type of sensors, because of their enhanced performance in some areas, e.g.: temperature sensing on high voltage transformers, or electrical isolation of patients in medical treatments, there are challenges that have to be surpassed, if we consider that fiber Bragg grating (FBG) sensors are the most common fiber sensors and have been in the market since 1995. Twenty years after, fiber sensor sales have not taken off as expected.

It is a fact that some of the "market hurdles and barriers "as proposed by A. Méndez [11] remain unsolved , and here are some of this:

- *Unfamiliarity with the technology*
- *Conservative/no-risk attitude of industries & customers*
- *Need for a proven field record*
- *Cost*
- *Availability of trained personnel*
- *Turn-key type systems (complete sensing solution)*
- *Lack of standards*
- *Quality, performance, packaging & reliability deficiencies across vendors*

These are several unsolved problems that only a few active companies have managed in order to make the customers confident enough to buy their sensors. Although the objective of this thesis is not focused in the sensors market, it is important to take into account the actual context and aim for solutions to promote the growth of the optical fiber sensing field. The reality is that a vast majority of the sensors found reported in journals don't evolve to become market products, and that is an opportunity to take.

1.2 CLASSIFICATION OF FIBER OPTIC SENSORS

A general optical fiber sensors classification differentiates intrinsic and extrinsic types. When light is modified outside fiber´s material then it is called extrinsic, on the other hand when light is modified inside the fiber it is the intrinsic type of sensor. Intrinsic sensors are commonly used because they are monolithic, smaller and compact; but to achieve this, sometimes implies complex processes of micromachining [12].

Aside of extrinsic and intrinsic types there is a basic classification for optical fiber sensors(OFS) based on different aspects shown in Table1.

Table 1.Basic classification of OFS.

Operation principle	Spatial distribution	Detection parameters
Intensity modulated	Point	Physical
Wavelength modulated	Distributed	Chemical
Phase modulated	Quasi-distributed	Biosensors
Polarimetric		

A complete classification of OFS, and a broader description can be found in ref.[13].

The fiber Fabry-Perot interferometer (FFPI) sensor works by detecting the phase modulation of a light beam, but its performance depends more on the interrogation scheme that on the structure of the interferometer. Naturally, fiber interferometers are wavelength modulated sensors but they can be also interrogated in intensity; which is the simplest way of interrogation [14]. It can be a point sensor because of the reduced fiber's diameter and because in and extrinsic scheme it senses/detects with the tip of the fiber where most of the times is placed a transducing material (functionalized polymer), a capillary fiber, or a micro fabricated cavity in order to allow the interaction between the light and the transducing material and/or the sample of interest. Nowadays we can find reports on the use of FFPI to detect physical, chemical and biomolecules without needing fluorescence or bio markers [15]. The uses listed, the design, fabrication, and interrogation versatility made the FFPI the best starting point for this research.

1.3 MOTIVATION

Multi-parameter sensing capacity is lately one important characteristic of fiber sensors that has been investigated in order to develop the lab-in-a fiber technology. But also the importance of multi-parameter sensing lies in the possibility to accomplish a correct measurement of one variable by simultaneous monitoring of changes of another variable such as ambient or sample temperature; or sample position, for example. Most of the reported fiber sensors are capable of measuring two or more physical variables, e.g.: temperature and other variables such as pressure, strain, force, vibration, to mention a few.

The most recent optical fiber sensors reported are capable of refractive index measurements or biomolecules detection but they are not multi-parametric. Surface plasmon resonance (SPR)-based fiber optic refractometers are the most used for biological applications. For example, tapered fiber plasmonic refractometers have reported an experimental record sensitivity of 11,800 nm/RIU for biological sensing applications [16]. Even though its outstanding sensitivity these are extremely fragile and need to be cleaned or replaced after each measurement.

Fiber refractometric/bio-sensors have a common disadvantage: the optical fiber needs to be immersed (into liquids) or in contact(solids) with the sample to achieve the measurement. When the fiber contacts the sample both, sample and fiber, can be damaged. While measuring liquid samples, the task is more complicated because one has to clean the fiber between sample measurements to obtain again the reference or base signal. This procedure normally executed in preliminary lab test for characterizing sensor, and supposing that the fiber sensor is easily replicable and cheap to fabricate, is not practical for a commercial, industrial, or medical use.

This work began trying to solve the need for refractive index measures avoiding any contact between fiber and sample. After researching about fiber interferometers, an elegant/efficient solution was to have a fiber sensing tip that never contacts the sample, thus there is no fiber contamination or degradation during the test.

Along the development of this work, with a better understanding of the operating principle; the goals also evolved. Achieving multi-parametric measurements using the same experimental setup and with the same fiber tip. Broadening the horizon for future applications on industrial and biomedical areas.

2 FIBER FABRY-PEROT INTERFEROMETER

Fiber Fabry-Perot interferometer (FPI) setup is very simple, since it was demonstrated at the beginning of the 80´s [17] a myriad of different structures, of different grades of complexity, have been demonstrated. The simplest FPI structure can be built with just a cleaved optical fiber separated a distance L from a flat reflecting target. When it is made with the same fiber or the fiber has been modified to create an internal cavity then it is called intrinsic FPI (IFPI). When the cavity has air or a different material from the fiber, then is called extrinsic FPI(EFPI), see Fig.1. Independently of its cavity fabrication process or material composition, they share the same operating principle, even if they are used in transmission or reflection. This dissertation focuses on the analysis of the reflectivity of an EFPI formed by a lead-in fiber tip and an external reflective surface: optical fiber, polymer, polished glass, glass substrate coated with a gold layer and liquid surface.

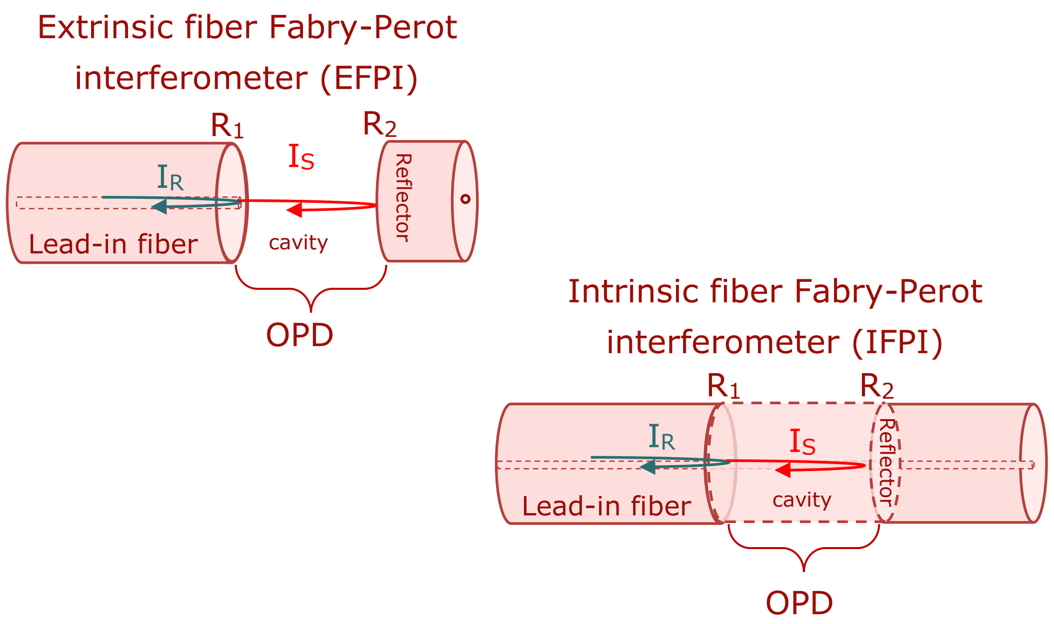

Figure 1.Types of fiber Fabry-Perot interferometers due to its fabrication. Optical path length difference between beams provide information for sensing applications. R_1 and R_2 are the reflective surfaces that limit the interferometer's cavity, OPD is the optical path difference between beams I_s and I_R.

Light enters the interferometer by the lead-in fiber(fig.1), at the fiber endface part of the incident light is reflected(I_R) the rest of the light enters the cavity and travels along it until is reflected back by the reflective surface. A portion of light traveling along the cavity is re-coupled into the fiber core (I_S) interfering with the previous beam I_R. The amount of light reflected at each surface depends on the reflection coefficient of the surfaces (R_1 *and* R_2). The optical path length difference between both beams is defined as $OPD = n * L$, where *n* is the refractive index of the material in the cavity and *L* the length of the interferometer's cavity. The two beam interference equation below describes this phenomenon, neglecting the resonance effect due to the low reflectance of R_1 and R_2 surfaces from fig.1, [17]:

$$I = I_R + I_S + 2\sqrt{(I_R I_S)} \cdot \cos\left(\frac{4\pi nL}{\lambda} + \varphi_0\right) \quad (1)$$

where I represents the intensity of the interference between beams I_R and I_S. λ is the wavelength of the light, and φ_0 stands for the initial phase difference between light beams. The resulting optical spectra shows a modulated signal that depends on interferometer´s cavity physical parameters such as refractive index, length, reflectivity of the mirrors and light source spectral characteristics. In these parameters lies the sensing flexibility of this device.

Although more complex models to describe this EFPI using for example Kirchoff's diffraction formalism have been proposed [18, 19], Santos and Jackson in [20] concluded that for some interrogation schemes like white light processing, assuming normal incidence and no absorption, the EFPI's formal transfer function can be simplified to obtain the eq.(1) written above.

In order to quantify the performance of this EFPI or other fiber interferometers, it is a must to know how to interrogate it. The next section of this document will describe the most common methods to obtain information from the fiber interferometer.

2.1 INTERROGATION SCHEMES

The basic setup to interrogate a single-mode fiber EFPI, where the lead-in fiber plays the role to deliver and collect the light from sensing area, is shown in Fig.2a. This is advantageous in sensing applications, because is more practical to use one fiber tip probe to measure a variable of interest, e.g. measuring temperature inside an oven. The broadband light source(BLS) could be a super luminescent light emitting diode which are fabricated with different bandwidths ranging from 20 to 100 nm and at different center wavelengths around 1310nm and 1550nm. But also a white light source or a swept laser source can be used. By means of a single mode fiber coupler (2:1) light from the BLS is fed to the EFPI lead-in fiber and carries the reflected light to the optical spectrum analyzer. The OSA has to be capable of measuring the light power in the complete wavelength span of the light source. The sensing application of the interferometer defines how broad the optical spectrum should be, and thus the light source to use.

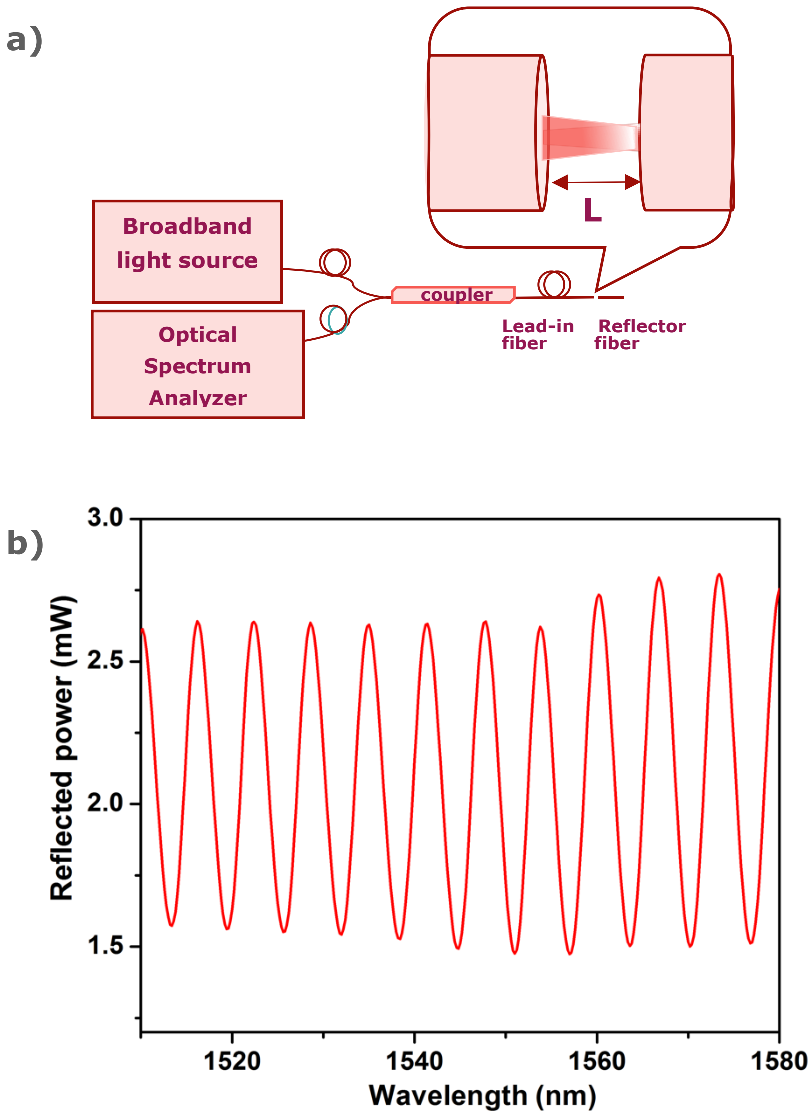

Figure 2. a) Components for an experimental setup of an EFPI. b) Reflection spectra of a single mode fiber EFPI with an air cavity length of 300 μm.

The previous scheme is not recommended to analyze the temporal evolution of an event, for example reflective surface vibration, in dynamical events one has to replace the BLS for a laser and a photodetector instead of the OSA. Modulation of light intensity due to the displacement of the reflecting surface will be detected by the photodetector and this intensity variation can be related to the vibration. But when determination of smaller cavities is needed, some have proposed to use a broader light source to minimize the uncertainty [21], where the modulation overall the optical spectrum is directly related to the cavity size. Fig.2b shows the optical spectrum of an EFPI, when this interferometer is built with a single mode fiber in front of the lead-in fiber. The graph shows the reflection spectra for an air cavity of 300 microns; it exhibits two valleys and a high modulation amplitude of approximately 1mW.

When the cavity length is increased the modulation period decreases inversely as well as the amplitude, this behavior was observed experimentally and is shown in fig.4, section 2.1.1.2. As in bulk optics interferometry, the fringe visibility is used to quantify the fringe modulation amplitude and helps to determine interferometer's performance [13].

These interrogation schemes are directly dependent on the two types of light sources available high-coherence and low- coherence. Laser sources in fiber interferometers have shown higher sensitivity and a faster response for dynamic measurements.

The inclusion of appropriate signal processing techniques applied to the optical spectrum analysis has demonstrated sensitivity/ resolution advantages [22]. These techniques are applicable to wavelength and phase modulated fiber sensors and will be described in the following section.

2.1.1 Spectrometric interrogation

The spectral interrogation methods described in this section are based on the acquisition of the optical spectrum by means of an OSA to analyze it by means of signal processing algorithms. These algorithm based methods comprise fringe visibility [23], wavelength tracking [24], and Fourier transform [25]. Due to the equipment needs these methods began to be more popular about ten years ago. Recently with the evolution and commercialization of distributed feedback semiconductor lasers (DFB) in parallel with faster electronics and computer communication protocols is more frequent to find systems that possess powerful laser sources (up to 20mW) and photo detection modules capable of acquiring an optical spectrum of 80nm at 5Khz [10]. Enabling and improving the way these signal processing algorithms aim to extract more information from optical spectra.

2.1.1.1 *Fringe visibility*

The fringe visibility is a parameter that assesses quantitatively the modulation amplitude produced by interference that is observable in the optical spectra, it is defined as:

$$Visibility = \frac{(I_{MAX} - \mathrm{I}_{\min})}{(I_{MAX} + \mathrm{I}_{\min})} \tag{2}$$

where I_{MAX} refers to the maximum and I_{min} to the minimum intensity values of the modulated signal in the optical spectrum. This is one of the simplest methods along with the wavelength tracking. The fringe visibility behavior of an EFPI built with two standard single mode fibers is shown in fig.3 below. While light travels through air the beam expands and light intensity decreases, this is described by the inverse square law where the intensity at a distance r from the source is proportional to I_{source}/r^2 ,[26]. In ref. [23], Chen proposes to use the EFPI's fringe visibility to relate it to the refractive index of different glasses but although the cavity size was constant, the fringe contrast changes with each sample, failing to achieve an absolute refractive index measurement.

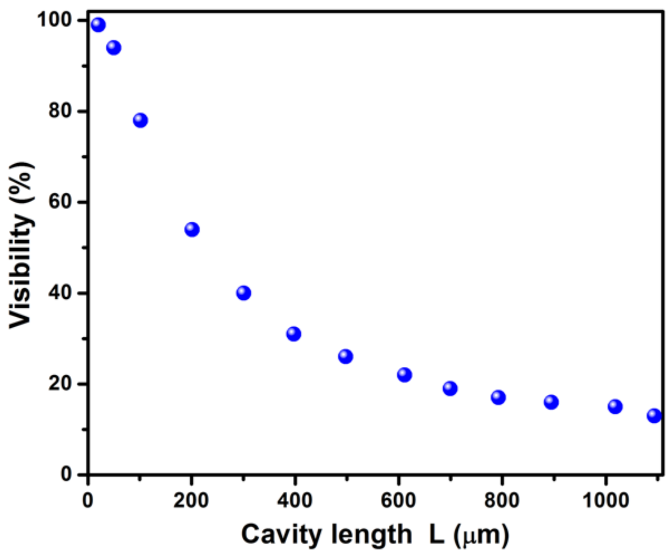

Figure 3. Visibility of the single mode fiber EFPI vs. gap between fibers.

2.1.1.2 *Two-point interrogation or period tracking*

When a FFPI is fed with a broadband light source as in fig.2a.and an OSA is used, it is possible to see a modulation as in fig.2b. When the sensing and reference beams interfere constructively is produced a maximum in the optical spectrum. The optical path length difference corresponds in this case to the gap length and is then determined from [27],

$$L = \frac{(\lambda_1 \lambda_2)}{2n(\lambda_2 - \lambda_1)} \tag{3}$$

where λ_1 , λ_2 represent the wavelengths of two consecutive peaks or dips of the spectrum($\lambda_2 > \lambda_1$) and *n* is the refractive index of the material in the cavity. This technique is also named period tracking because the period of a spectral interferogram (as in fig.2b) changes as the cavity of the EFPI changes.

Even though this is a simple way of calculate the absolute cavity length of an EFPI and has a broader linear range (compared to intensity modulated interrogation). The disadvantage consists in the determination of the peaks/valleys wavelengths, because a slight error in this values compromises the resolution and accuracy of the length measurement [22].

While the cavity of an EFPI is increased, the period of the modulation in the optical spectra observed in the OSA decreases inversely. The behavior shown in fig.4, clarifies the need of a complex detection system. The highest sensitivity lies at short cavities below 200 microns and for larger cavities higher wavelength resolution is needed to measure the period change in the OSA. On the other hand, by calculating the inverse of the period we obtain the frequency of this spectral modulation. Thus, the frequency has a linear trend that increases proportional to the increasing cavity length, see fig.5.

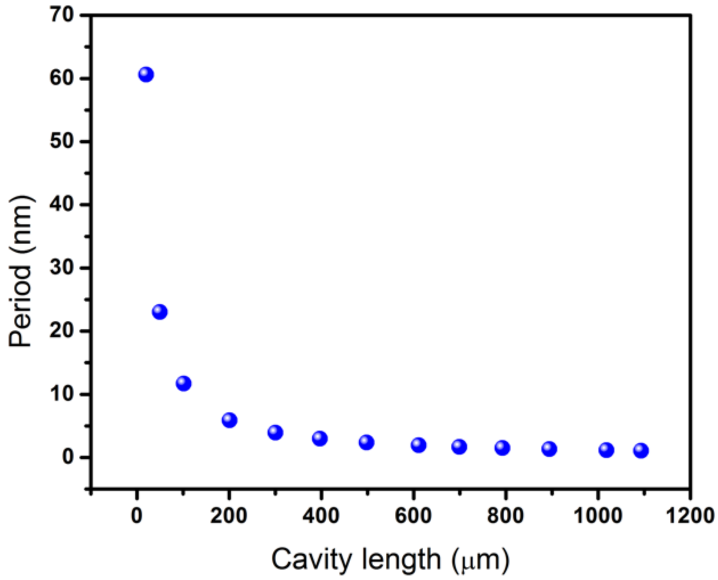

Figure 4. Period of the modulation in the optical spectrum vs. cavity length of an extrinsic fiber Fabry-Perot interferometer.

The Fourier transform method that will be described in the next section focuses on the determination of this spectral modulation frequency.

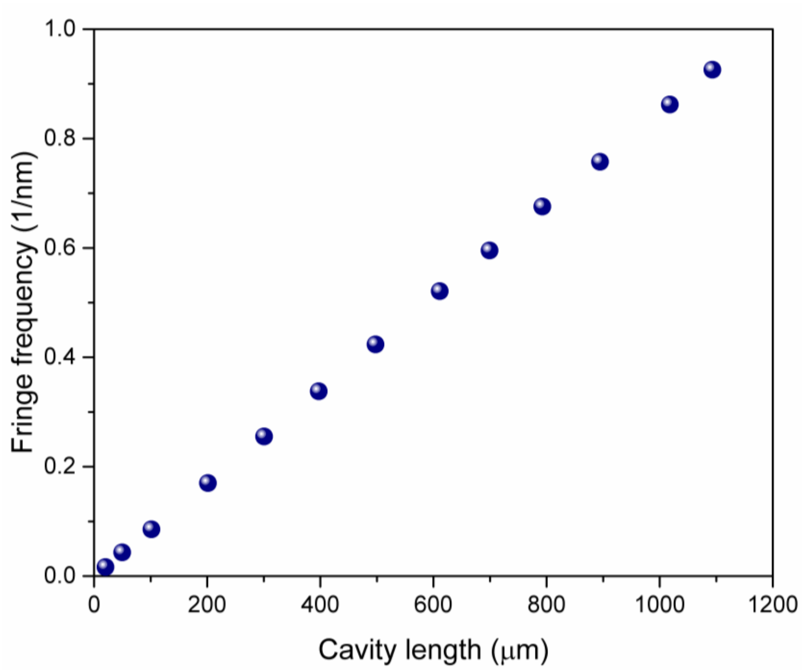

Figure 5. Fringe frequency vs. cavity length of an extrinsic fiber Fabry-Perot interferometer.

2.1.1.3 *Fourier transform method*

The gap length of the interferometer is obtained by applying the Fourier transform to the optical spectrum that outputs the interferometer. As stated in [22], for better results it is recommended to subtract the offset of the optical spectrum before applying the transform. The majority of spectrometers or OSA's acquire equally spaced discrete points to form the complete spectrum in the wavelength or frequency axis. But there are other FBG's interrogators recently popular because of its low cost, USB interface and portability named I-mon from Ibsen photonics [28], that acquire the spectrum with non-equally spaced points. In this case it is necessary to interpolate the points before changing the spectrum to Fourier domain. Another recommendation from Han [22], is to use a curve fitting method to the fringe spectrum in order to minimize the noise and to improve the FFT result, thus cavity length measurements result more accurate.

There are two ways of using the FFT, one is by applying it to the optical spectrum with wavelength in the X- axis; this leads to obtain a spatial fringe frequency in (1/nm) units. The other method is to acquire or convert the optical spectrum with X-axis in THz units and then apply the FFT. After doing this the Fourier domain X-axis will show the temporal fringe frequency with units in seconds while the peak position in this spectrum indicates the optical path length difference of light traveling a round trip through the interferometer's cavity.

Depending on the final application of the interferometer one can choose the method that suits best, this FFT method has a wide dynamic range, the more fringes the lower the error. The limit lies in the accessibility to a use a broader light source with good power uniformity and stability along its wavelength range. When high sensitivity is needed, and the phase shift is below 2π, then the wavelength tracking method described below is a better approach.

2.1.1.4 Wavelength or peak tracking

This method is based on tracking the shift produced by the OPD change in the interferometer pattern due to the external perturbation induced by the variable to measure. Even though following the displacement of a particular valley in the optical spectrum is simple and enables high resolution measurements, this method shares the disadvantages of intensity modulated interrogation: it is limited to phase changes smaller than 2∏ and also that is a relative measurement. Generally, in logarithmic scale, following valleys is better because they are narrower than the peaks. Otherwise, in linear scale the spectrum shows a sinusoidal wave. This method's measurement range is limited to the location of the valley inside the range of the window of the analyzer/spectrometer (see fig.6).

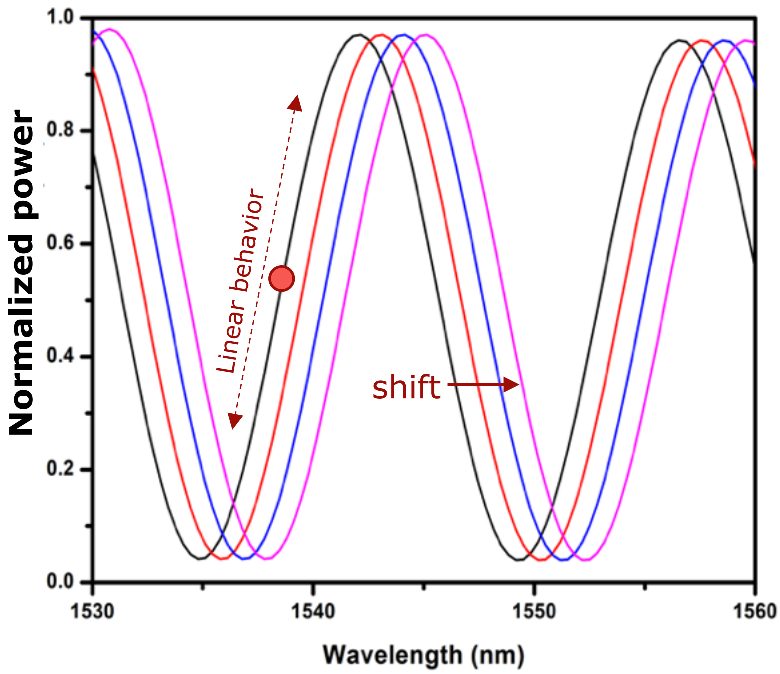

Figure 6. Example of interference fringes showing wavelength shift. The red circle represents a quadrature point.

These methods for interrogation are the most commonly found in the literature. To overcome its limitations and disadvantages along the past years, modifications have been proposed including combinations of them, like the one proposed by Ushakov in ref. [29] for picometer resolution.

2.1.2 *Intensity modulation*

Intensity modulated fiber sensing devices have the advantage of needing the simplest detection setup, that is a light source and a power meter or photodetector. The linear operation of the sensor interrogated by intensity depends of positioning the wavelength of the laser source at a quadrature point (see Fig.6), where a limited linear response is possible (slope of a fringe). This detection setup has been studied and implemented for distance/displacement, vibration, pressure, temperature sensing since the 80's, using single mode or multimode fibers or even bundles of emitter-receiver fibers[13]. Intensity modulated schemes are not capable of absolute phase measurements and they are limited to phase shifts of less than 2Π.

Based on a Fabry-Perot structure or micro-bending, this type of detection scheme was so popular that there is a broad classification of variations of it and proposed solutions to overcome light source intensity instability and relative measurements [30]. Fig.7. shows a fiber optic intensity modulated sensor for displacement detection, two receiver fibers where used to achieve a linear response over a limited range of about 60 microns.

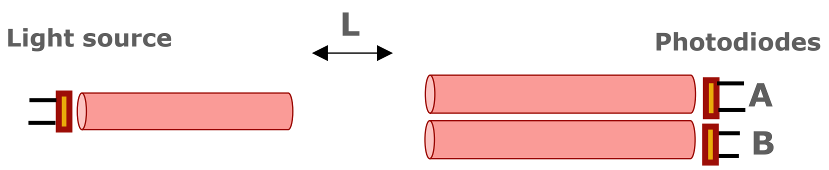

Figure 7. Setup for a fiber differential intensity displacement sensor.

2.2 *HOW TO INCREASE EFPI'S CAVITY LENGTH?*

The first step was to overcome EFPI's main disadvantage; the reduced length dynamic range since fringe visibility decrease as the cavity length increases. The second step is related to the EFPI capacity to achieve multi-parameter sensing, and it relies on the interrogation method. The goal was divided in two parts: structure modification and adequate spectrometric interrogation scheme.

Bing Yu, et al. in ref. [31] presented a detailed theoretical analysis of fiber fabry-Perot interferometers for sensing applications. They analyzed the sensitivity, visibility and dynamic range of intrinsic and extrinsic FFPI; comparing sources of different bandwidths, symmetric and asymmetric reflectivity on both mirrors. Is important to highlight the theoretical results they presented for an EFPI (unguided FFPI model) with asymmetric mirrors. The curves they presented for peak sensitivity, fringe visibility and dynamic range converge at large cavities "because the interference behaves closer to two beam interference at larger OPD" and tend to maintain the same value for cavities larger than 30 microns (220nm) even with a reflectivity difference between mirrors of about 70%. After simulating angular misalignments of both mirrors they had to consider a zero angular misalignment, because even for cavities smaller than 20 microns but with a misalignment of 6 degrees the sensitivity and fringe contrast drops to zero, demonstrating that in an EFPI this is a critical parameter and its effects are more accentuated for larger cavities. Along with mirrors misalignment, the beam divergence, and cavity length contribute to the losses.

In summary, increasing cavity length of an EFPI to tens of millimeters requires to increase as much as possible the reflective surface of the second mirror (R_2) to achieve a specular reflection trying to avoid misalignments between the lead-in fiber and the mirror. To probe the enhancement reached when increasing R_2 in an EFPI setup the experiment was arranged using the equipment shown in fig.2a. and the EFPI as shown in fig.8a. The resulting fringe visibility behavior against gap length is found in fig. 8b. Visibility is increased more than four times at the largest cavity, which is a good starting point. These measurements of visibility vs. EFPI gap length using a high reflectance mirror are also reported by Thurner [32], obtaining similar results for a smf-28–EFPI.

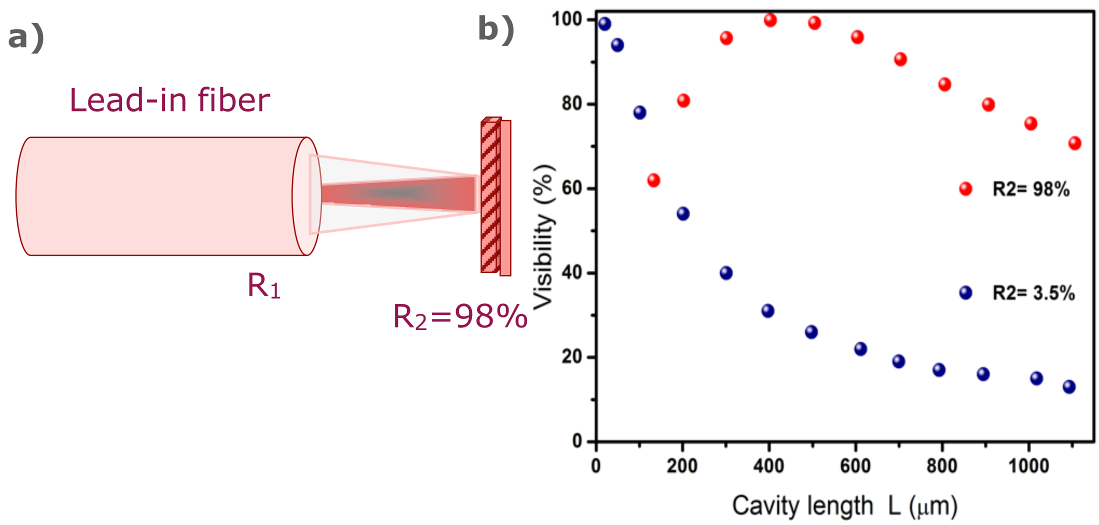

Figure 8. (a) EFPI with smf28 lead-in fiber and gold thin film mirror as the second reflective surface. (b) Graph of fringe visibility vs. cavity length resulting from the EFPI in (a).

But that is only half of the solution, the other part consists in improving the lead-in fiber. One part of the light is lost owing to the beam divergence exiting the lead-in fiber while propagates along the EFPI's cavity. Increasing the amount of light that can't be coupled back into the lead-in fiber[31]. The ideal solution would be to have a lead-in fiber that launches a collimated beam to the cavity and also couples light reflected efficiently.

The quest for enhancing the performance of the lead-in fiber is an old unsolved problem, although, some practical proposals in terms of ease as well as cost-effective fabrication process have proposed. Here they are briefly discussed:

2.2.1 *Graded index fiber collimator*

Zhang et al. [33], reported a visibility enhancement 4 times higher compared to smf-28 fiber EFPI at 500 µm by splicing a calculated length of graded index multimode fiber at the tip of a single mode fiber it is possible to modify the beam divergence at the lead-in fiber of an EFPI [33, 34]. They demonstrated that the visibility enhancement was caused by the reduction of the beam divergence angle that exits the lead-in fiber. For SMF-28e fiber the measured divergence angle reported was 7.7°, value in compliance with the one provided by the manufacturer($NA = 0.14\,, \theta = 8°$), [35]. The divergence angle that they report for the graded index fiber collimator is $\theta = 2.3°$ with a corresponding NA=0.04, a representation of this scheme is shown in fig.9. The best performance was achieved with a graded index fiber length of 310µm, probably the most complicated part of replicating this lead-in fiber structure would be to measure and cleave at the right length after the splice with the smf fiber.

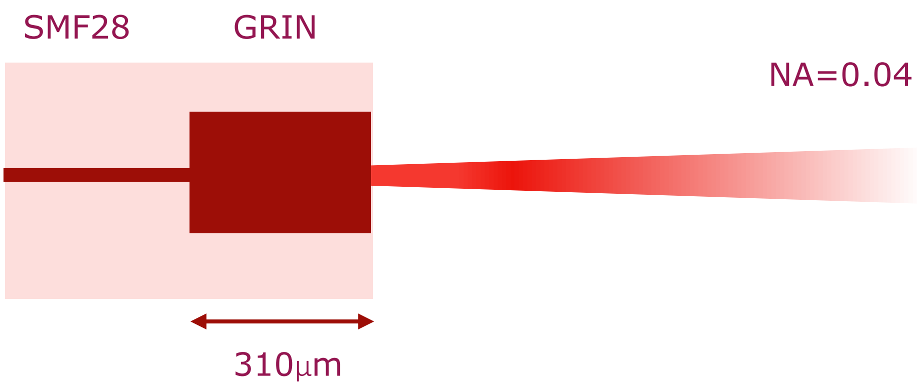

Figure 9. Scheme of the graded index fiber collimator from [33].

They compare and make use of theoretical model calculations and analysis based on the EFPI cavity plane wave propagation[36], and also the Gaussian beam profile considered in ref. [18]. The results presented suggest that the Gaussian beam propagation model gives results closer to the experimental values presented for an EFPI built with single mode standard fiber. On the other hand, for the graded index fiber EFPI, the ray matrix simulation seems to approach better.

2.2.2 Collimating lens

Thurner et al., used an optimized aspheric collimating lens to extend, for at least 100mm, the EFPI cavity [32]. Their objective was to measure displacement of high and low reflectivity objects, they used a lens with focal length of $f \approx 8mm$ and NA=0.5. The theoretical model presented is based in Gaussian beam propagation, they propose a coupling efficiency calculation to find the fringe contrast of the EFPI, which shows a good agreement with the experimental results. They noticed that EFPI gap can be increased even more by inserting the smf fiber in a ferule before the lens and by inducing an angle $\alpha = 0.2°$ to the reflecting mirror, multiple reflections created on-axis constructive interference; allowing to increase the separation between lens and mirror up to 400mm (Fig.10).

A remarkable achievement is that for a distance equal to 100mm the fringe visibility is higher than 60%. Even though their results are hard to overpass using a different method; the design and fabrication of the lens needed and the housing to fix the lens and the fiber seems to be much more complicated than splicing a graded index multimode fiber.

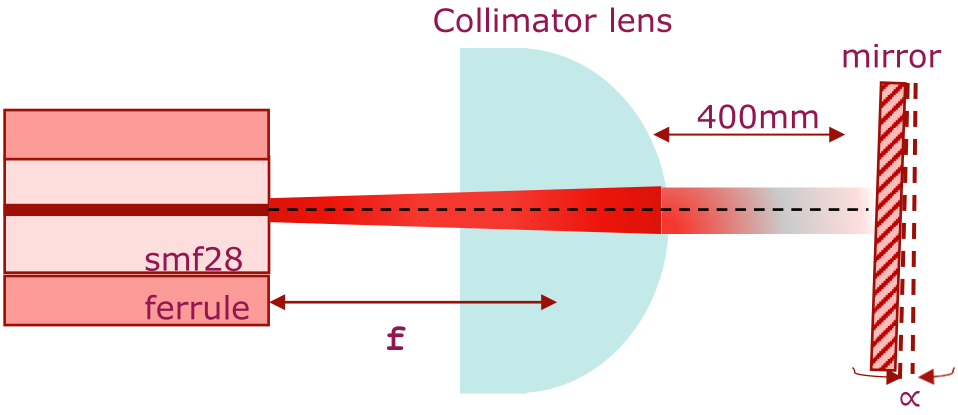

Figure 10. EFPI with collimator lens setup proposed to increase the cavity length up to 400mm [32].

2.2.3 Tapered fiber tip

The early research in fiber optic communications had the challenge of reducing coupling losses between fibers and light sources or detectors. The obvious solution where to use couple lenses, but also different approaches were proposed, for example fiber taper beam expander proposed by Jedrzejewski et al. in ref. [37]. This interesting report showed that by introducing a single mode fiber inside a capillary tube and then tapering it down from 350 to 40μm, the mode field diameter of the propagating fundamental mode was expanded at the taper waist more than two times from 2.6 up to 6μm. After tapering the fiber, they cleaved it at the center of the waist to obtain two tapered fiber tips. To demonstrate the enhancement, they used one tapered fiber tip as lead-in fiber and the other as a receiver, shown in fig.11, that was coupled to a power meter and then they compared the power of the light coupled by the tapered tip versus an unmodified fiber tip. They observed that the amount of light transmitted is more than 8 times higher with the tapered ones for a 500-micron gap. When both tips are separated 1mm, light is still transmitted, while with standard fiber it is not possible.

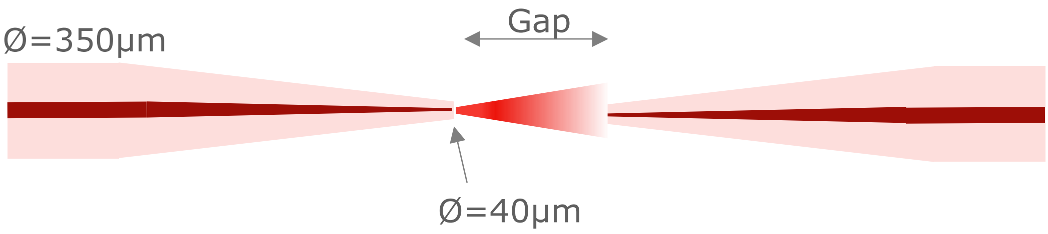

Figure 11. EFPI in transmission scheme with two taper beam expanders.

The results exposed above for the three different methods of beam collimation/expanding from the lead-in fiber show that the best option is the lens to enlarge the cavity at the maximum range reported for an EFPI. Since the objective was to realize refractometric measurements of small samples around 1 cm thick, it was decided to try first to replicate the results of the taper beam expander and if they were not sufficient for this application then the graded index collimator option would have been implemented. The next chapter will focus on the design and fabrication of the optimized fiber taper diameter in order to achieve the maximum beam expansion to increase the cavity length of EFPI.

3 TAPERED FIBER TIPS

This chapter is meant to describe the theoretical and practical details to fabricate the optimized waist diameter of the tapered fiber tip to enhance the EFPI measurement capabilities. But first it is necessary to present some basic concepts referring to fiber optic as dielectric cylindrical waveguides.

Fiber optics are dielectric passive devices that propagate light along its symmetrical axis by total internal reflection, z-axis of the step index profile fiber depicted in fig.12. The core's refractive index has to be higher than the cladding's in order to confine light along the fiber core. Both refractive indexes along with the core/cladding dimensions' ratio are directly related with the number of modes propagating in the fiber. Fiber specifications like the *V parameter*, also known as the normalized frequency, indicate the number of modes that a fiber can propagate and is defined as

$$V = \frac{2\pi a}{\lambda}\sqrt{(n_{co}^2 - n_{cl}^2)} \qquad (5)$$

where n_{co} is the refractive index of the core, n_{cl} the refractive index of the cladding, *a* the core radius. When $V \gg 1$, the waveguide has multimode propagation. For a step index profile fiber, when $V < 2.405$, the waveguide allows propagation of only the fundamental mode for a limited range of wavelengths.

3.1 THEORETICAL MODEL FOR TAPERED FIBER OPTIC WAVEGUIDES

The standard commercial fibers are designed to minimize transmission losses; to achieve this, the most amount of light propagates confined to the fiber core. From the core, light never "sees" cladding external boundary. This is why is possible to model fiber optic waveguides as 2 cylindrical layers. Snyder and Love [38], presented a detailed theoretical treatment for optical waveguides in general and also in specific cases as optical fibers, absorbing, non-absorbing mediums or even bending in optical fibers. By solving the Maxwell's equations with their corresponding and specific initial and boundary conditions is possible to get the eigenvalue equation. The numerical solution of the eigenvalue equation leads to obtain the value for the propagation constant (β). Knowing β, the electromagnetic field distribution of each mode that can propagate in the waveguide is solved analytically. These solutions are called modal solutions; when obtained by scalar mathematics the modes are called scalar modes or LP modes, since they are approximations for exact HE, EH, TE and TM solutions. The exact solutions require vector calculus treatment, thus are called vector modes.

A simplification of the eigenvalue equation is made when the core-cladding refractive index difference is small (Δn_{12}<<1). It is an efficient and cost-effective design condition to produce commercial fibers [35]. And it also gives the name to the theory of "weakly guiding". It simplifies the eigenvalue equation derived from the scalar waveguide equation and allows the use of its solutions (LP modes) as a valid approach. The resulting eigenvalue equation is [40]

$$ua\frac{J_{l+1}(ua)}{J_l(ua)} - wa\frac{K_{l+1}(wa)}{K_l(wa)} = 0$$

$where\ u^2 = n_{co}^2 k_0^2 - \beta^2,\quad w^2 = \beta^2 - n_{cl}^2 k_0^2,\ J_l \text{and}\ K_l$, are Bessel and modified Bessel functions, a the core radius, n_{co} is the refractive index of the core, n_{cl} the refractive index of the cladding, $k_0 = 2\pi/\lambda_0$, the wave number of the wavelength in vacuum, and l the azimuthal mode index. Every l index have various roots that are indexed (l, k) and each one of those $\beta_{l,k}$ will correspond to a transversal mode.

The propagation constant β is real for propagating a mode; imaginary in case of lossy or radiation modes. Lossy modes are correct solutions of the wave equation but physically light is radiated outside the waveguide.

The relation between the propagation constant and the waveguide's effective index is as follows

$$\beta = k * n_{eff}; \qquad v_{phase} = \frac{c}{n_{eff}}; \tag{7}$$

where n_{eff} refers to the effective refractive index of the propagating mode in the waveguide. $k = \frac{2\pi}{\lambda}$ *, is the wavenumber,* λ the wavelength and *c* the speed of light in vacuum. In order to describe the propagation of light along a fiber it is necessary to calculate the modal field distribution, the propagation constant and/or its corresponding effective index. The eigenvalue equation is used for mode dispersion calculation of fiber optics as waveguides and lead to perform simulations for the fundamental mode behavior when fiber's structure is modified.

In the scope of this dissertation the fundamental mode corresponds to HE_{11} mode or its associated LP_{01} scalar approximation. The adiabatic down-tapering process should ensure that no other mode than the fundamental is excited and propagated. This fundamental mode will be expanded due to the decreasing *effective refractive index*(n_{eff}) of the fiber while tapered. In order to determine the theoretical optimum diameter to achieve the maximum beam size by tapering a fiber, the calculation of the fundamental mode dispersion n_{eff} vs. fiber diameter is needed.

The fiber optic waveguide shown in fig.12-left represents the two-layer structure, that is useful for standard fibers when light travels confined inside the core and a small fraction in the cladding. On the other hand, when fibers are down-tapered to microns or even nanometers, the core material can be neglected to use the two-layer model; or the three-layer model that takes on account the surrounding medium.

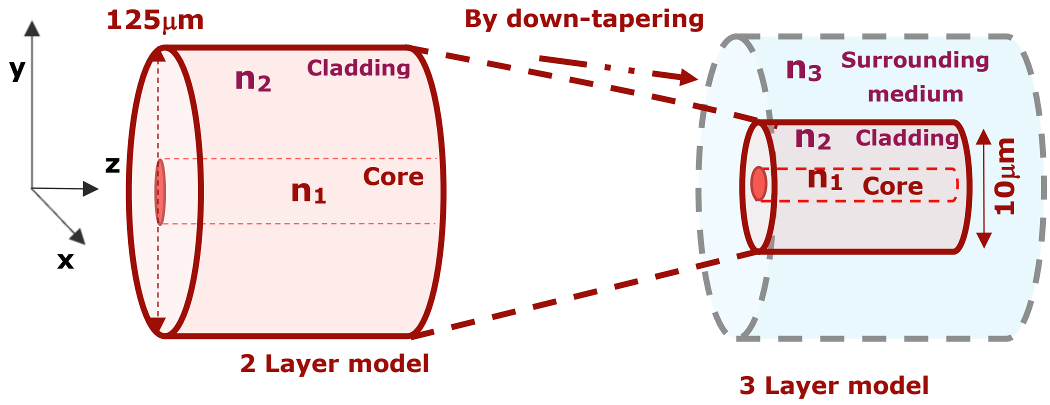

Figure 12. Structure of the fiber optic 2- layer and 3- layer models, they have common core and cladding layers but the 3rd layer is the surrounding medium with refractive index n_3.

The 3-layer models are useful to understand what happens to the propagating modes along the un-tapered, transition and tapered parts of fibers, see for example ref.[39].

Even though this models where proposed by researchers in the field like Belanov, Monerie, Erdogan and Zhang [40-44], none of them present the explicit complete solutions for each one of the TE, TM, and the hybrid modes. Based on this publications, K. Karapetyan et al. implemented a compilation of functions for MATLAB® and was called "Optical fiber toolbox(OFT)". The OFT provides functions to solve the guided modes in optical fibers. Where the exact solutions for weak and strong guiding cases are provided, taking on account the material dispersion. Appendix A of this document contains the equations for the calculations made in the Optical fiber toolbox and the applicability of the functions. In the next section will be explained how OFT was used to obtain the theoretical tapering-down diameter for the smf-28 fiber used.

3.2 USING THE OPTICAL FIBER TOOLBOX

The toolbox contains a vast number of functions whose objective is to find the modes (scalar and exact) for a given cylindrical waveguide with dimensions and materials. After studying the references and the support information from the webpage is possible to understand in a short time how to use these functions for a specific need.

The first step was to look for the specifications for smf-28 fiber, from [35]. The manufacturer gives a fiber core/cladding ratio=8.2/125μm, and for λ=1550nm, the mode field diameter MFD=10.4μm with an effective group index of refraction N_{EFF}=1.4682, this value corresponds to an n_{eff} =1.4539(for the fundamental mode LP_{01}/EH_{11}). Because this are weakly guiding fibers, where typical values are between:Δn=0.002-0.008; the starting values proposed for the calculations where n_{clad}=1.4522, n_{core}=1.4572. After some iterations using the function *oftDemo.m, which calculates the mode effective refractive index,* the corresponding values *of* n_{clad}=1.4512, n_{core}=1.457 result in an n_{eff} =1.45389.

In order to compare the results that the toolbox gives, the first test was made with the function **oftDemo.m**, and the input values used where

Table 2. Input parameters for smf-28 simulation using the Optical fiber toolbox.

	core	cladding	medium
Layers refractive index:	1.457	1.4512	'air'
Fiber core/cladding ratio:	8.2/125		
Lambda:	1550nm		

This function solves for all the modes that can propagate in a fiber with the introduced values, and then gives the value for the n_{eff} of the mode of interest (the fundamental mode in this case) at the specific wavelength. With this value solves and displays a graph with the intensity distribution of fundamental mode field. Fig.13(a) shows the results for $n_{eff}LP_{01}$ mode, the black circle represents the fiber core and in (b) the mode field diameter measured from the data obtained from the simulation. The mode field diameter(MFD) was obtained after normalization of the mode field intensity and locating the points where the intensity was $1/e^2$ of the maximum.

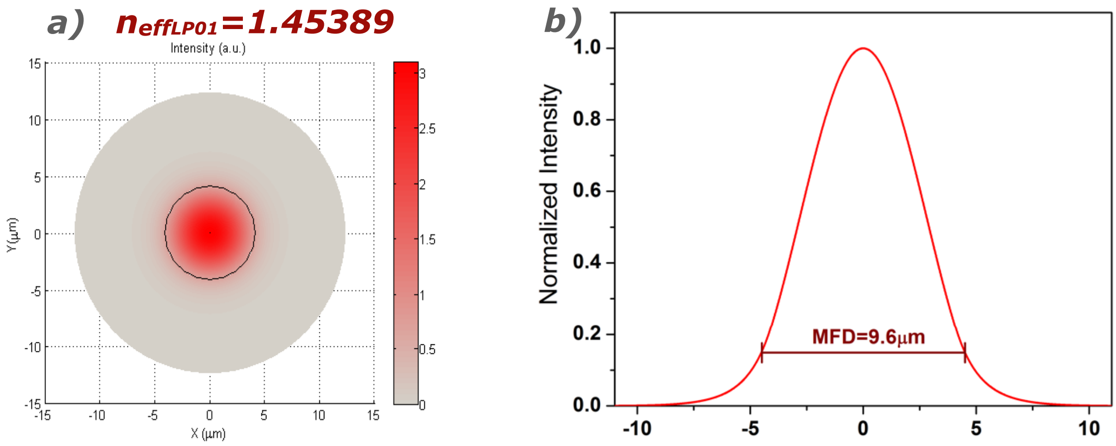

Figure 13. (a) Numerical results obtained from OFT for an smf28 fiber for the LP_{01} mode field. (b) Mode field diameter calculated from the numerical mode field distribution.

The value obtained for the $n_{effLP01}$ and the calculated MFD show complete agreement with the specifications given by the smf-28 fiber manufacturer (Corning). After validation of the results from OFT, the next step was to obtain the $n_{effLP01}$ curve for the different taper-down diameters of this fiber. The function named **tutorial3ls.m** calculates this by solving the different equations found in appendix a, same values to describe the fiber, corresponding results are shown in fig.14.

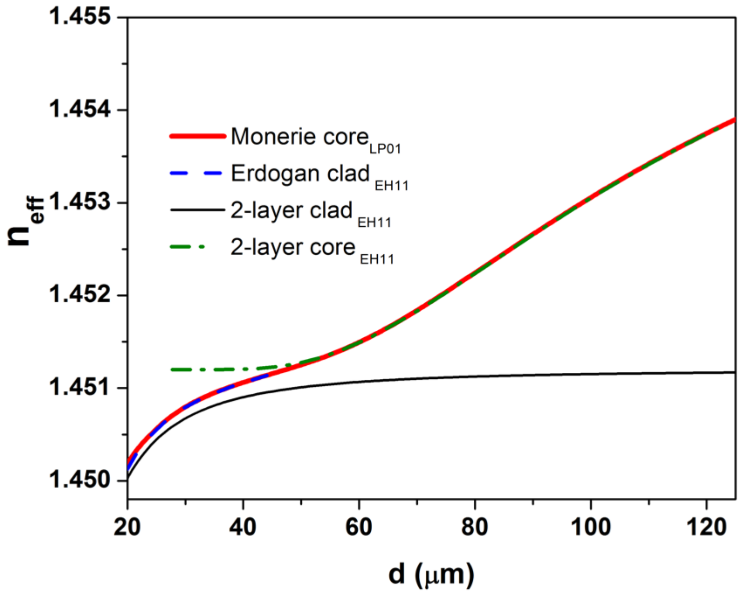

Figure 14. Fundamental mode vs. fiber taper-down diameter for smf28 fiber for λ=1550nm.

Fig.14 shows the curve of n_{eff} vs. diameter for the fundamental mode (LP_{01}, EH_{11}) solved using the 3-layer and 2-layer models in OFT for SMF-28 fiber. It is observable that for the 2-layer model, either for the core or cladding-guided fundamental mode (green and black lines, respectively) there is a gap between them. This discontinuity is because the value of n_{eff} approximates to n_{clad} value. The transition between core-cladding fundamental mode guiding is of interest in other cases for designing tapered fiber modal interferometers because by down-tapering a fiber is possible to excite the next mode to the fundamental one (LP_{02}) and produce interference between them [41]. Karapetyan[45], recommends to use the Monérie [45] scalar solution to calculate the modal dispersion curve avoiding the mentioned discontinuity.

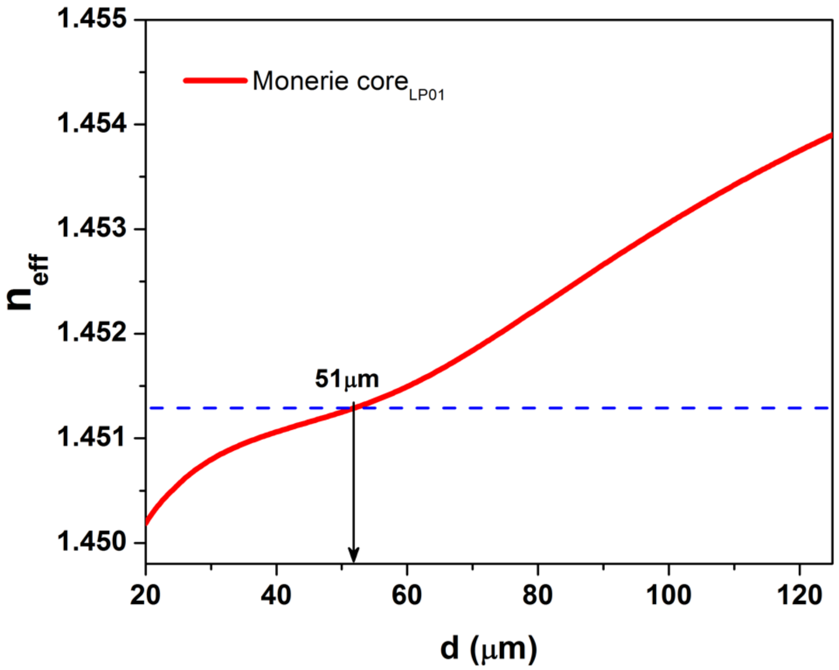

Figure 15. Fundamental mode (LP_{01}) effective refractive index vs. smf28 fiber taper-down diameter using Monérie scalar solution in OFT.

Solving $neff_{LP01}$ vs. diameter, with the fiber parameters stated in table 2, the curve of fig.15 was obtained. The blue dashed line indicates the cladding refractive index, and according to Love in [48], where both (red and blue) lines intersect is when the maximum beam expansion for a core guided fundamental mode is reached. Lines intersect when the diameter decreases to 51 μm.

To complete the characterization of the expected tapered fiber tip, Fig. 16 shows in (a) the calculated $n_{effLP01}$ with the field intensity distribution, notice that n_{eff} coincides with n_{clad} from table 2. In (b) the expected beam profile and $_{MFD}$=13.44 microns. The numerical results show an increment of 40% for the fundamental mode for a tapered-down diameter of 51 µm.

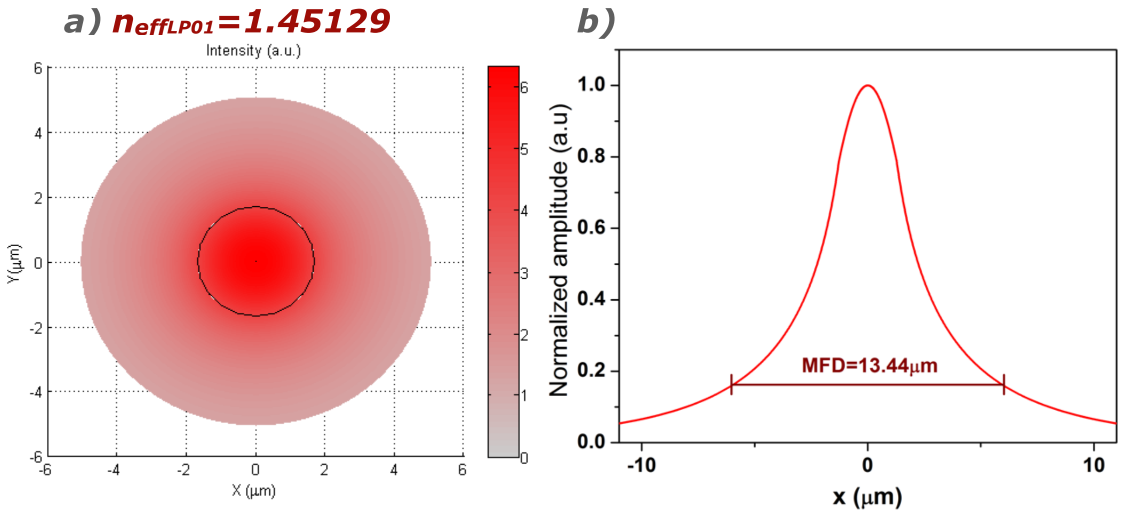

Figure 16. (a) Numerical results obtained from OFT for an smf28 fiber tapered-down diameter of 51 µm for the LP_{01} mode field. (b) Mode field diameter calculated from the numerical mode field distribution.

The numerical results show that the beam expansion works for tapering-down a standard telecommunications mono mode fiber such as smf-28 in contrast with was reported by Jedrzejewski, et al. in [37], they though this worked because of the Vycor capillary fiber they use to taper the mono-mode fiber.

Before fabrication of the tapered fiber tips, it was necessary to determine the taper slope angle that these tapers should have. When tapering-down a mono-mode fiber, the light guided as the HE_{11} can be coupled to the next HE_{12} mode depending on the critical slope angle. This analysis is developed in the following section.

3.3 TAPER ADIABATICITY CRITERIA

The critical angle criteria for fiber tapers was proposed by Love et al[46]. It states that when the taper slope angle (Ω) is lower than the critical angle (Ω_{crit}) calculated for two modes, then there is no coupling between them.

$$\Omega_{crit} = \frac{\rho(\beta_1 - \beta_2)}{2\pi} = \frac{d(z)\Delta n_{eff}}{2\lambda} \tag{8}$$

where ρ is the fiber radius, β_1 and β_2 are the propagation constants of the first and second modes of interest, *d(z)* is the tapered fiber local diameter, Δn_{eff} represents the effective refractive index difference between modes, λ is the wavelength in vacuum.

To get the curves of n_{eff_EH11} and n_{eff_EH12} vs. diameter, the OFT function **tutorial3ls.m** with parameters of table 2 was used. The graph in fig.17 shows the curve for the critical angle considering the two closer modes HE_{11} and HE_{12} that can be coupled by tapering at the transition $n_{eff}=n_{clad}$. With the n_{eff} curves of each one, the critical slope angle according to eq. (8) was calculated for λ=1550nm.

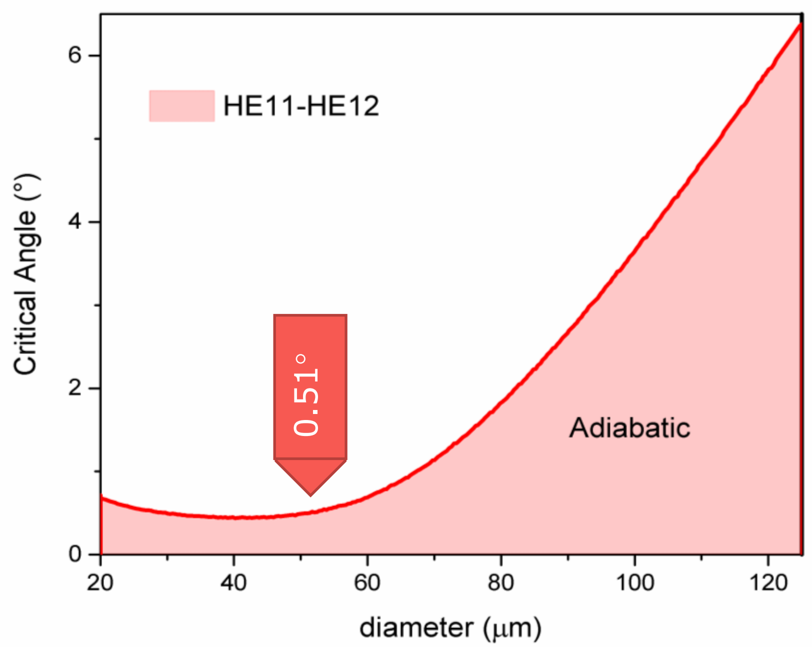

Figure 17. Critical angle (Ω_{crit}) vs. taper diameter for EH_{11} and EH_{12} modes with smf28 fiber specifications.

The graph in fig.17 shows that for a taper with a waist diameter of 51 microns the taper slope should be below 0.51°, this means that the slope should be smoother to avoid losses. So, to achieve this the taper should be linear with transitions of at least 4 mm to avoid getting close to the critical slope angle.

3.4 FABRICATION OF TAPERED FIBER OPTIC TIPS

Fiber optics have been tapered since the 80's , the first tapered fiber tips were used as beam expanders; fiber tapers can be fabricated by two distinctive methods: by heating and stretching the fiber [37, 47], or by etching with hydrofluoric acid(HF) [48]. A different successful application of the tapering technique was for coupling light between two or more fibers (fiber couplers) [49]. These tapered fibers where made with custom built machines, consisting of two translation stages in the same axis, one at each side of a flame burner.

The most complicated part of fabricating the fiber tapers is to match the designed taper shape. The expected shape is shown in fig.18 considering the critical angle restriction. The transition length was established to be of 5mm to assure a smooth transition avoiding any losses by tapering (at least from design).

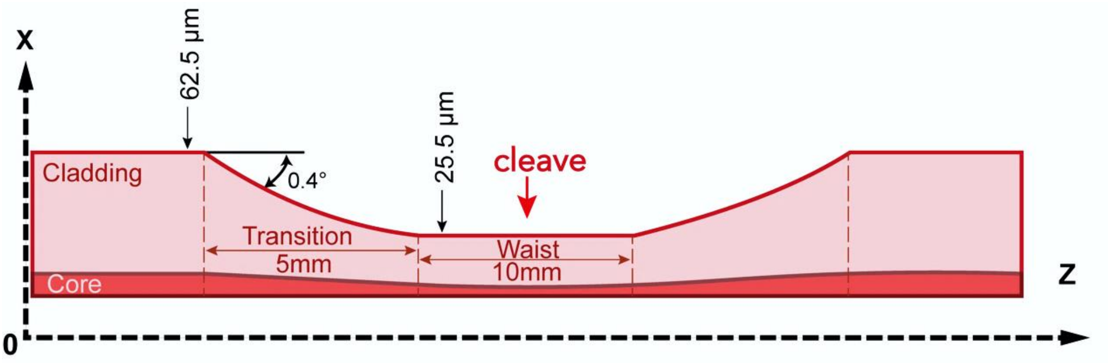

Figure 18. Shape of the designed symmetric adiabatic taper to fabricate the fiber tips.

3.4.1 Vytran glass processing unit GPX-3000

This machine is capable of producing fiber splices, combiners, couplers, and endcaps. As can be seen in the drawing of fig. 19 the user accessible part consist of two fiber holding blocks, uses a tungsten filament micro-heater to soften a section of the optical fiber while the mechanical mounts pull the fiber to create the taper [50]. It is controlled by software from a desktop computer allowing repeatable results to fabricate low-loss fiber tapers with a desired profile, as long as a correct filament normalization process was performed. After tapering process, the fiber taper profile can be inspected by an optical system. The operation of this machine is very simple, the user has to perform the filament power normalization before starting the tapers processing. The software that controls the machine has the option of customize the taper design to meet specific design parameters. In order to confirm the beam expansion at the tapered fiber waist, tapers with waist diameter of 50, 55, 70, and 85 micrometers were made. The fiber tips were obtained after cleaving the tapers at the middle of the waist length. The next section contains a table with the corresponding parameters.

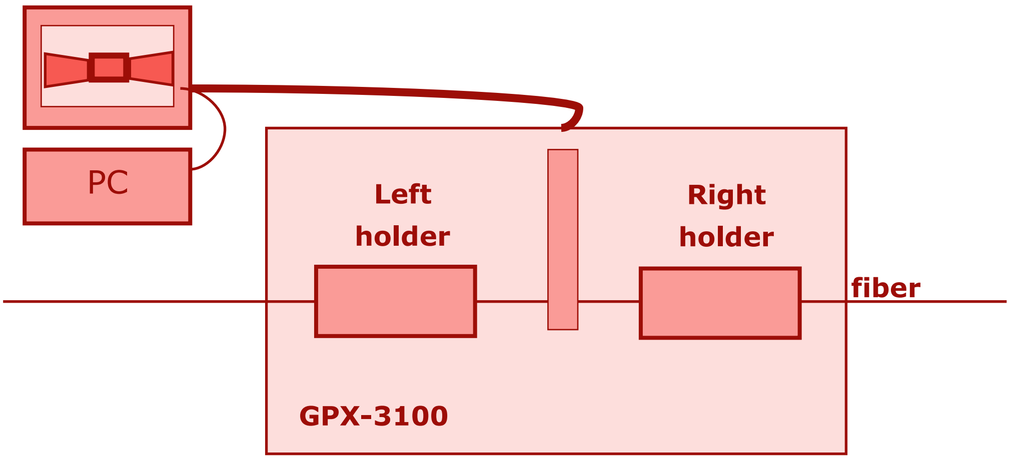

Figure 19. Vytran glass processing machine GPX3000 used to fabricate the tapered fibers required.

3.4.2 Parameters for fabricating the tapers with the Vytran GPX-3000

Table 3. These parameters where used for different taper waist diameters achieving losses below 0.5dB

Taper waist diameter [μm]	Norm. Power[W]	Tapering Power[W]	Transition length[mm]	Waist Length[mm]
50	60.2	50.2	5	10
55	72.5	63	5	10
70	60.2	46.9	5	10
85	60.2	46.2	5	10

3.4.3 Parameters for cleaving at the taper waist with the Vytran LDC-200

Based on the cleaving parameters for a fiber with diameter of 125 microns the modified parameters are shown in table 4 below.

Table 4.Parameters used to cleave the waist of the tapers with the LDC-200

Taper waist diameter [μm]	Cleaving Tension[gr.]	Cleave Fwd. steps	Cleave osc. counter
50	56	35	70
55	56	35	70
70	80	35	70
85	100	35	70

4 EFPI WITH TAPERED LEAD-IN FIBER TIPS

This section describes the experimental setup used to measure the mode field diameter of fiber tapers fabricated. The optimum tapered diameter obtained by numerical calculations was compared with the experiments.

4.1 Visibility characterization of tapered fiber tips EFPI

Fiber taper tips were used to build the EFPIs. First, each fiber taper tip was spliced to the output port of a 3-dB coupler, the BSL and OSA were connected to the input ports. Light spectra reflected from the fiber taper tips were measured and no modulation were observed. After holding the lead-in fiber taper tip, as well as the reflecting fiber, on a three-axis translation stages, fiber endfaces were aligned and placed in close contact. Light emitted by a super-luminescent led centered at 1550 nm and a bandwidth of 100 nm is launched in one of the coupler inputs. Half of the fiber-coupled intensity reaches the lead-in fiber taper tip and approximately 4% of that is internally reflected. The exiting beam propagates along the cavity and reaches the reflecting fiber. When fibers are in close contact, the intensity of the light coupled into the reflecting fiber core, measured by the power meter, is maximum if fibers are perfectly aligned. The setup used for the measurements is shown in figure 20(a). Taking advantage of the PC connectivity that the motorized XYZ stages, the power meter, and the OSA had; a custom LabVIEW® program was developed for these measurements. To assure that fibers were perfectly aligned, the program made an XY scan to find the fiber position (coordinates) in which the transmitted amplitude is maximum and proceed to align both fibers(fig.20b), then acquired the spectrum from the OSA and calculated the visibility for each tapered EFPI cavity length. These steps were repeated with 4 different taper diameters and a standard fiber until the visibility dropped below 20 %.

a)

b)

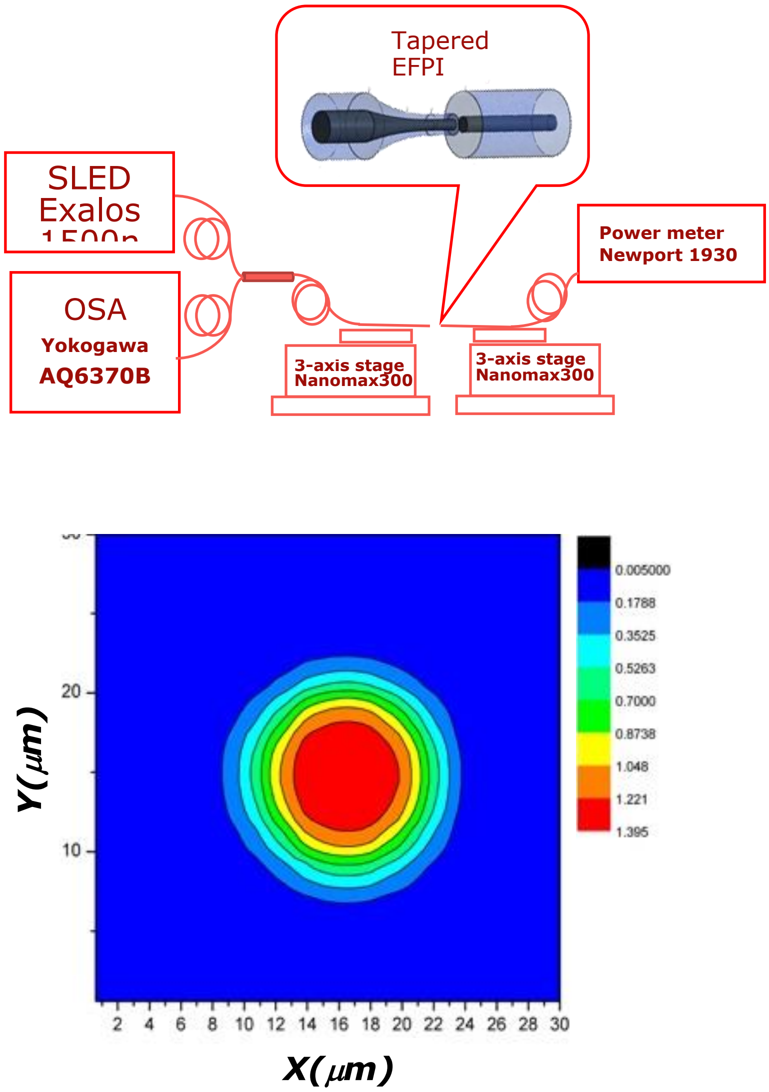

Figure 20. (a) Experimental setup used for the tapered EFPI visibility measurements. (b) Intensity pattern of the XY scan for alignment between two smf-28 fibers.

The transmitted light intensity pattern between two aligned smf-28 fibers is shown in fig.20b.When the lead-in fiber is tapered down to 55 μm the fringe visibility curve is almost linear, in the cavity range between 500 and 2500 μm(see fig.19). A straightforward application of this interferometer is to measure the longitudinal displacement by analyzing the fringe visibility. The main advantages of this displacement sensing technique are the simplicity, the long range displacement measurement, and thermal stability of the sensor since the fringe visibility is a temperature-independent parameter.

a)

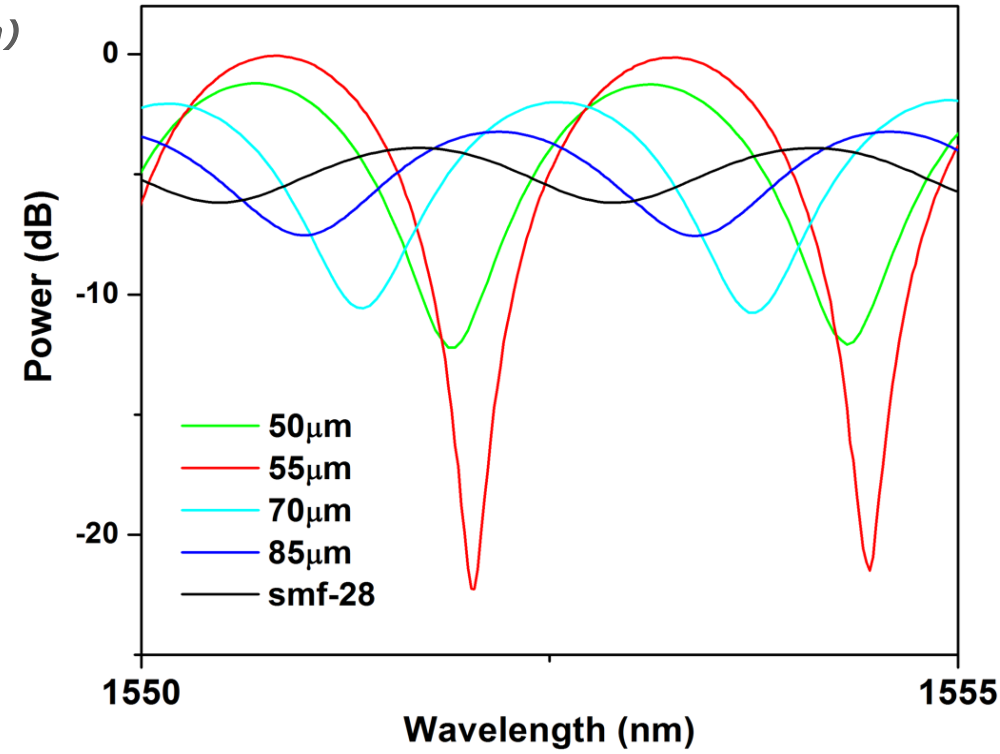

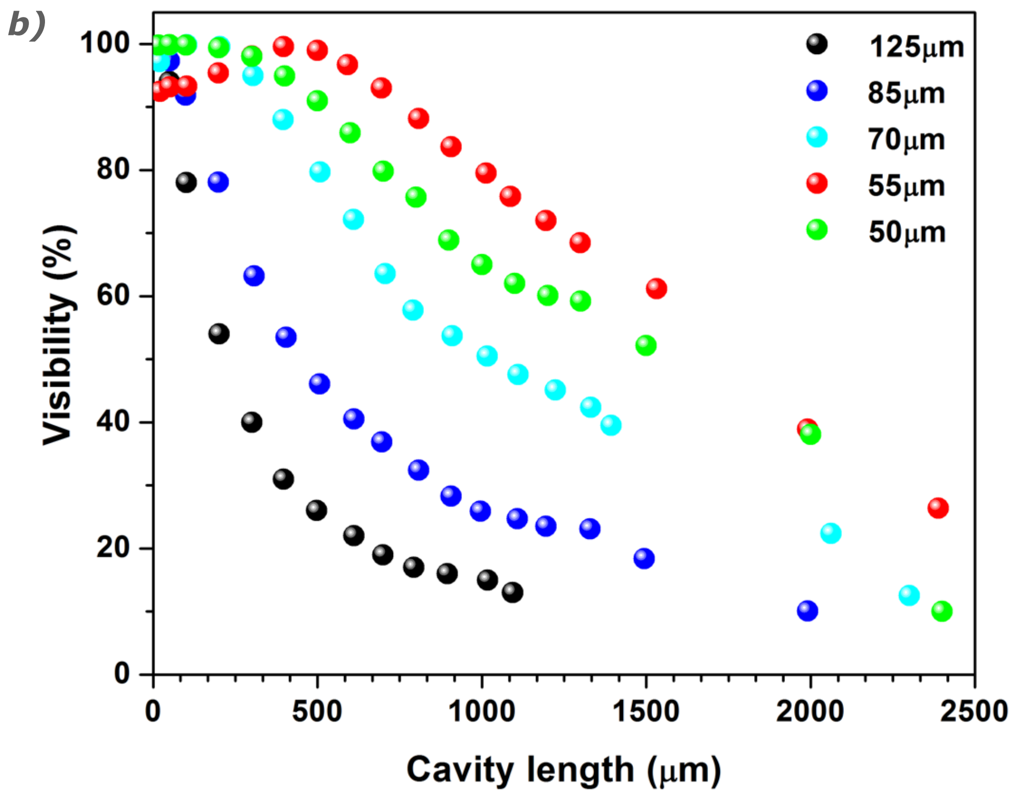

Figure 21. (a)Experimental spectra observed when the diameter of the lead-in fiber was 125, 85, 70, 55 and 50 μm. In all cases the air gap was 500 μm approximately. (b) Results showing the effect of the lead-in fiber tip diameter in the fringe visibility evolution as a function of the cavity length.

The experimental results shown in fig. 21a and 21b, are a proof that is possible to improve the spectral fringe visibility in an air-cavity Fabry-Perot single-mode fiber interferometer, by tapering the lead-in fiber. The divergence of the beam exiting the lead-in fiber decreases as the fiber taper diameter decreases, this behavior can be observed from fig.21a. For a fixed 500μm cavity, the tapered tips enhance the visibility until the 55μm diameter is reached; after that, the visibility decreases again (50μm tip), because it exceeds the core-mode cutoff diameter. The highest modulation amplitude of around 22dB corresponds to the 55μm tip, followed by the one with 50μm. This confirms the numerical results obtained in section 3.2 and shown in figs.15 and 16. Even though, best results were obtained with 55-micron diameter tip than with 50micron diameter; at first we thought this may be due to the fabrication or to the cleaving process but after repeating more than 20 times both processes the behavior is the same. The experimental and numerical diameter difference could be due to the proposed refractive indexes, because those are not provided by the fiber's manufacturer. For this dissertation these results were sufficiently close enough and useful to try to explain what was physically happening while tapering-down and why there is an optimum tapering diameter.

After observing the experimental results with the 55μm diameter tip, attempts to obtain better results using tapered tips with diameters around that value (55±4μm) were made, but after the visibility characterization none of them were superior. Then, it was stated that for this work the 55-micron diameter tapered tip was the best option.

4.2 55-micron tapered tip EFPI with different reflectors

In the first experiment a polished fused silica glass window, 25 mm diameter and 1.8 mm width and a reflectance of 4.2%, was used as a reflective surface. In the second one a gold thin film mirror was used, the film was deposited by physical vapor deposition over a borosilicate glass slide with a resulting reflectance > 98% at 1550 nm. Both samples were fabricated at the optical workshop of the C.I.O., A.C. [51]. The experimental setup is shown in fig.22a, the fiber tip and the target were mounted on a precision translation stage (Thorlabs, NRT-150M). The tapered fiber tip in one extreme was fusion spliced to a FC patchcord and was connected to an FBG interrogator (Micron Optics, SM-125). The FBG interrogator has an Ethernet port to communicate with a computer, multi-channel capability and a sampling speed of 500Hz. Since the interrogator and translation stage were capable of being controlled by the PC, a custom LabVIEW® routine was developed to displace the mirror, acquire the optical spectra and to calculate the fringe visibility.

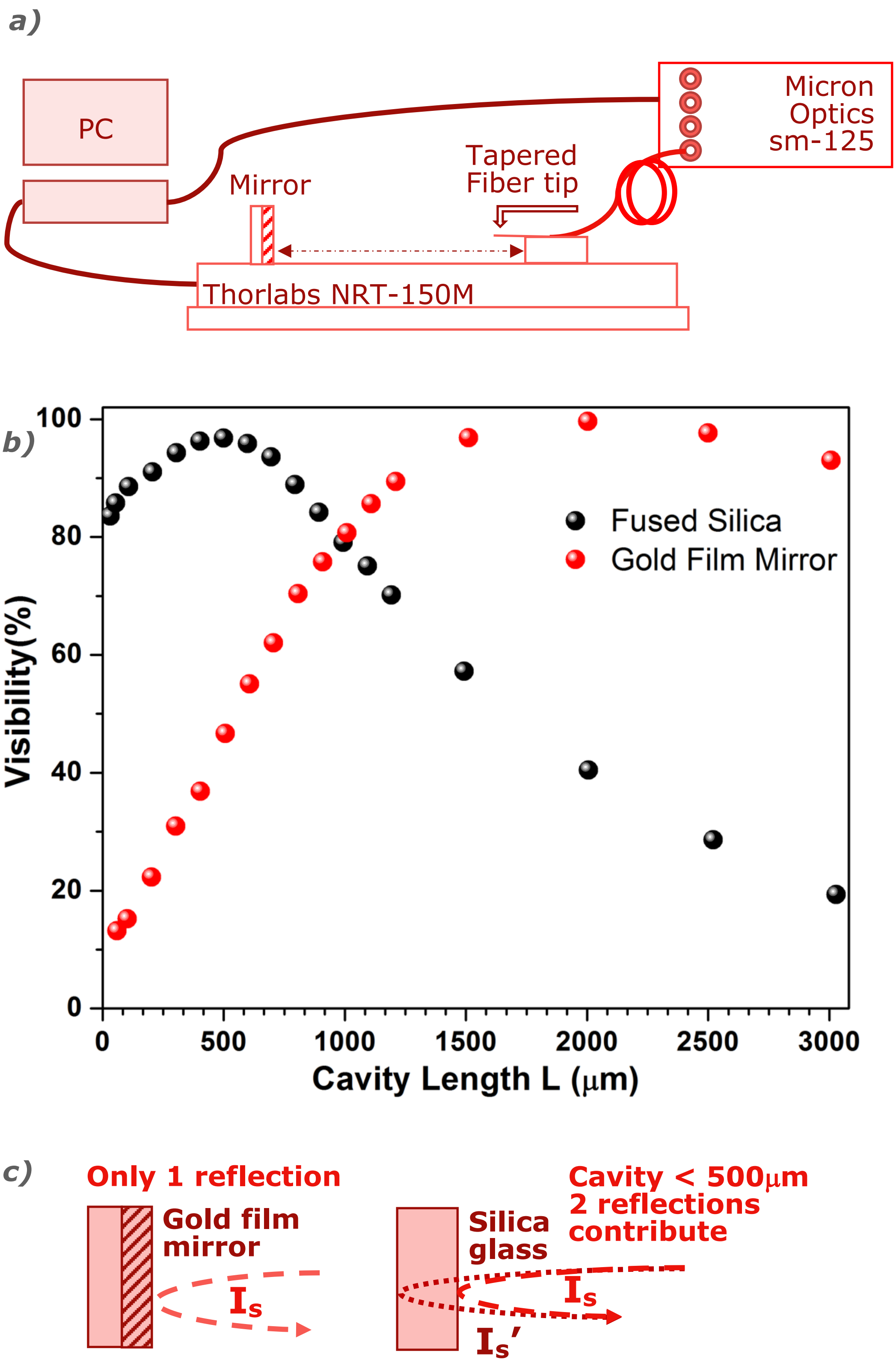

Figure 22. (a) Schematic diagram for the measurement of fringe visibility vs. cavity length with two reflective surface with different reflectivity. (b) Visibility results for fused silica and gold film mirror for EFPI cavities up to 3mm.(c) When using a glass window as reflector, beams reflected from each surface contribute to the interference at small cavities, maintaining the high visibility.

The fiber tip and reflector surface were placed parallel to each other at the minimum distance about 50-microns, then the reflector was moved away from the fiber tip in steps of 100-microns up to 3mm. In each step the optical spectrum was saved in a .csv file with the corresponding value for the cavity length and fringe visibility, obtained results are shown in fig.22b.

While the reflectivity of the mirror increases, the maximum visibility peak is displaced to larger cavities and becomes broader. This happens due to the high reflectance of the mirror; improving the visibility at large cavities but decreasing it greatly at smaller ones. Because the launched light intensity and reflection coefficients are constant (fiber≈4%, mirror≈98%), while cavity is increased at some point, the intensity of the beam Is of fig.22c (that travels a larger distance over the air) gets closer to the intensity of the beam reflected at the fiber endface which is around 25 times smaller than the one of the gold mirror. And only at that cavity length the maximum visibility is achieved. This demonstrates that by changing the reflection coefficients of both surfaces is possible to tune the maximum visibility peak between a 0-2mm range.

Otherwise, with the silica glass window used as reflector, the visibility maintains a high value for small cavities, this happens because there is one more interfering beam (I_s', fig.22c) that was not present when the metallic film mirror was used. The intensity of the third beam contributes only when mirror is close to the fiber tip, by superposing another sinusoidal modulation to the single reflector optical spectrum. When the silica reflector is far, I_s' light is lost before being coupled back to the fiber. It seems that this alters the behavior below visibility maxima, when L=500μm. Then, visibility decreases faster than when the mirror is used.

This leads to think about the properties that an ideal reflector for measuring small and large displacements using an EFPI should have. If this objective is of interest, then reflection and transmission coefficients value should start around 50% to allow the emergence of the second beam (I_s') and try to maintain high visibility on short and large ranges.

5 LONG-RANGE DISPLACEMENT SENSING

Since, the objective of this dissertation was to achieve contactless measurements using and EFPI, distance sensing was considered as the first step. In fact, the results obtained and described in this section were part of the first publication product of this research [52]. Distance measurement is important in industrial and scientific applications, including for example, precision alignment, position monitoring, atomic force microscopy, vibration analysis, and robotics, between others. This is not a new topic; several optical techniques have proposed to accomplish displacement sensing [53]. However, those based on optical fibers have several distinctive advantages, such as fast and contactless measurements, high resolution, and others mentioned in section 1.1, [32, 33, 54-65]. A great number of fiber optic displacement sensors have been reported in the literature, the most popular ones are based on intensity modulation and interferometry. Intensity modulated typically use optical fibers with high numerical aperture or fiber bundles to collect as much reflected light as possible from a flat reflecting target [54, 60, 65].

On the other hand, interferometric sensors detect changes of the optical path difference between two interfering beams, which result in a detectable change of the optical spectrum.

Intensity modulated sensors offer low resolution and large measuring range. However, their accuracy is affected by random fluctuations of the optical source or uncontrollable attenuations in the optical fiber junctions. Interferometric displacement sensors offer ultra-high precision but the measuring range is typically limited to few millimeters [58, 61, 62, 64], and they tend to be more complex.

Fabry-Perot interferometry offers one of the simplest approaches to sense displacement [32, 33, 58, 61, 62, 64]. In an EFPI, the period, amplitude and/or wavelength position of the peaks and notches of the interference pattern depend on its cavity optical path properties; but for this specific application just the cavity length. As period, phase, or shift of the interference pattern can be measured with high accuracy, sub-nanometer displacements can be sensed with an optical fiber FPI [61, 64].

5.1 MEASUREMENTS

To determine the cavity length (L in this case) the fast Fourier transform (FFT) of the interference pattern was calculated. It is known that the FFT of a sinusoidal pattern with period P (fig.23a) exhibits a single peak at a spatial frequency (υ). The FFT provides cavity length information by locating the X-axis position of the peak with high precision (fig.23b), even when the interference pattern exhibits poor visibility. Fig.23c shows the behavior of the fringe period and spatial frequency in the Fourier domain versus L, as the length increases, the period of the interference fringes decreases exponentially. In contrast the analysis of interference pattern in Fourier domain exhibits a linear relation between length and frequency peak of the FFT modulus, as is shown in the inset of fig.23c.

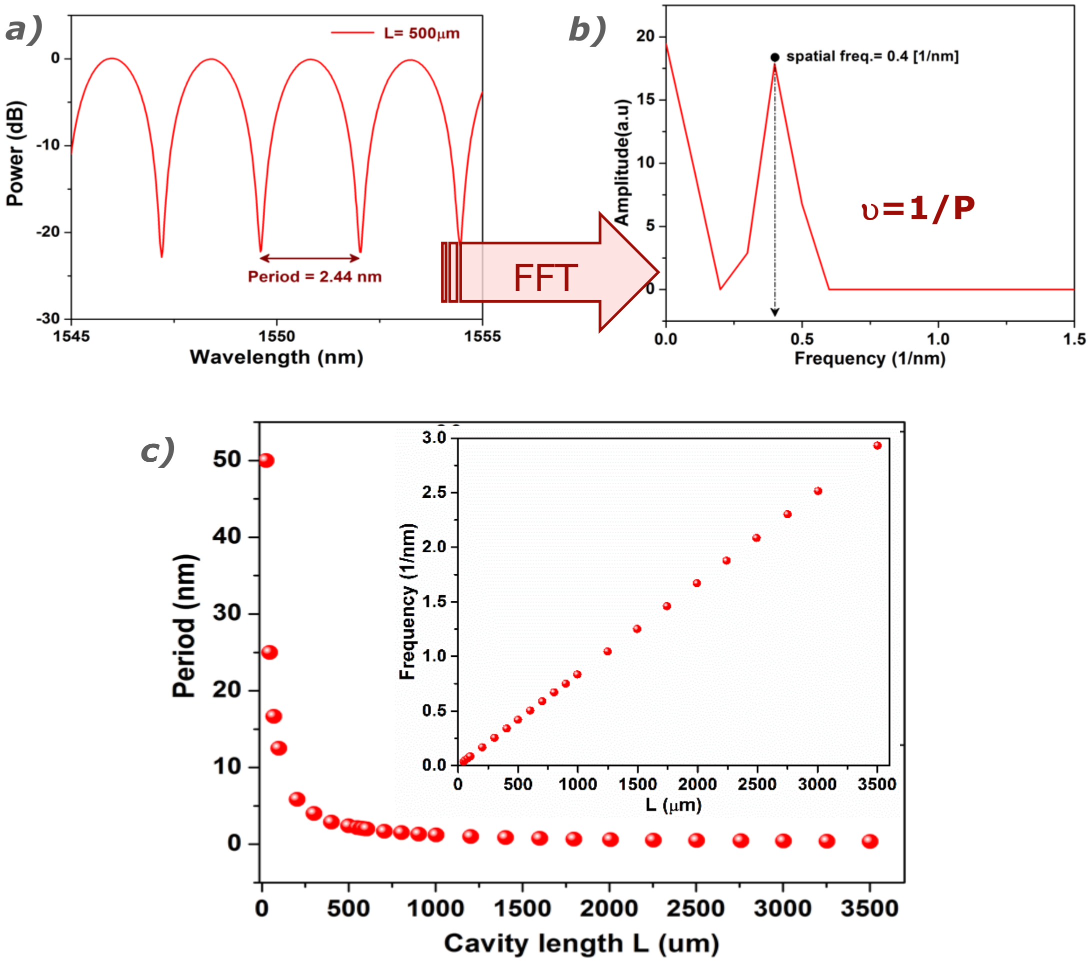

Figure 23. (a)Optical spectrum interference fringes for L=500-microns with its fringe period in nanometers. (b) Spectra of (a) in Fourier domain. (c)Trend of the fringe period and frequency versus length.

We used the experimental setup described in fig. 22a of the previous chapter to calculate the FFT of the reflection spectra from the FBG interrogator and an ad hoc LabVIEW program was developed. Fig.24a shows an image of the screen of this program, the optical spectrum acquired has a wavelength span of 80nm where the points are uniformly spaced each 5 pm (graph at the top), then the FFT is displayed in the central graph, and at the bottom the same optical spectrum showed in a shorter wavelength span converted from dBm to mW. The tapered-EFPI cavity length was acquired and displayed at a rate of 10 Hz in the screen of the computer. Two visibility vs. length measurements were made, one using the fused silica glass and the second with the gold film mirror in order to compare them.

a)

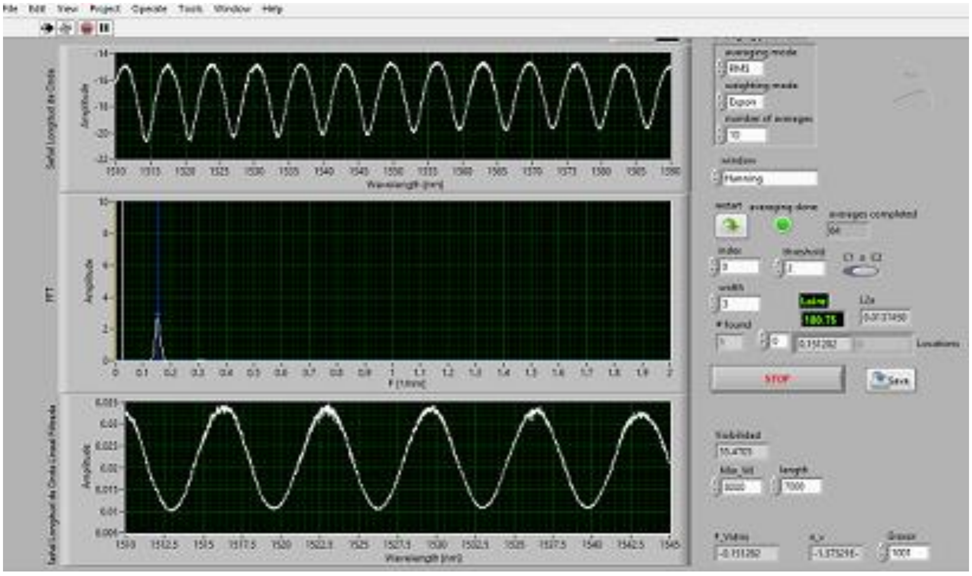

b)

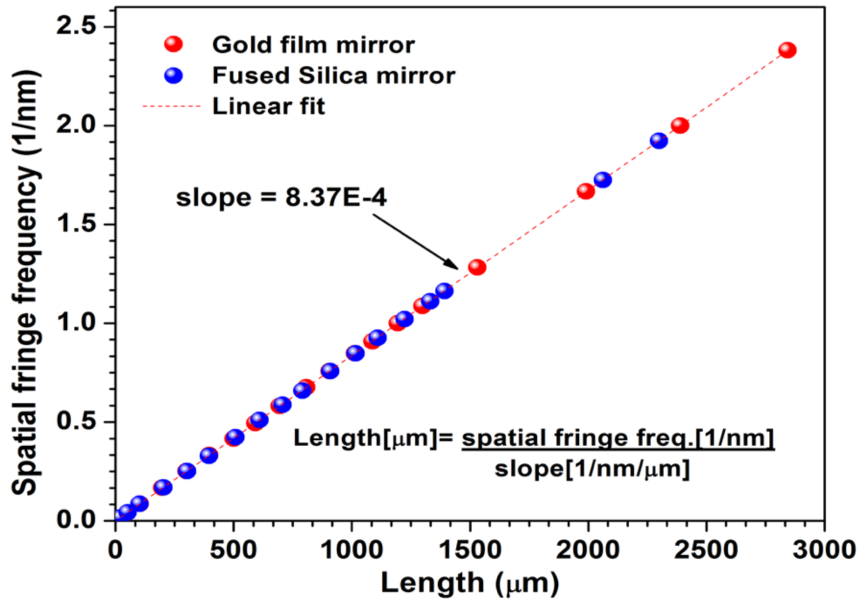

Figure 24. (a) Screen of the custom program used to measure displacement with the tapered fiber tip EFPI. (b)Spatial fringe frequency (relation obtained experimentally) vs. Cavity length.

5.2 Results and discussion

The slope of the linear fit of the experimental points is 8.37E-4 (fig.24b), so it is possible to stablish a direct relation between the spatial domain (Length-axis) and spatial frequency domain of the FFT (X-axis) than can be expressed as

$$L = \frac{spatial\ freq.}{8.37E-4}(in\ \mu m) \tag{9}$$

This is a very simple method to measure the distance between the fiber tip and a target because the frequency peaks of the FFT modulus can be directly related with the air cavity length.

The results shown in fig.25b also demonstrate that the reflectance change of the cavity reflector, neither the interference fringe visibility alter the spatial fringe frequency vs. length relation, thus it was concluded that this calibration is valid for distance measurement independently of the reflection coefficient of the object used as reflective surface, or even if the reflectivity varies along the measurements. On the other hand, the reflection coefficient of the mirror impacts directly on the maximum visibility peak position; this is shown in fig.25a and b. For lower reflectance targets the visibility´s maximum peak locates at a medium length (500-microns), but the peak of the visibility graph shifts to larger cavity length as the reflectivity increases(2mm). Since the reflectivity of the Au mirror was around 98%, almost 100%, the maximum visibility was obtained for a cavity length of L=2mm, (about 1.5mm more than with the low-reflectivity target).

For a low-reflectivity target such as glass (around R=4%) measured visibility can be obtained for cavity lengths L<3mm (fig.25a). However, for the gold film mirror, the measuring range was extended up to 80mm (fig.25b) making evident the advantages of using a higher reflectance surface to build a large cavity tapered-EFPI. Fig.25c shows the linear relation between measured positions vs. translational stage positions for 100-micron steps, the maximum difference between the calculated value and the stage position was ±

0.7%, but this combines the error from the stage and the calculated cavity. The highest resolution (1μm) was achieved when the visibility was also high (about 99%). On the opposite, when the visibility<10% the measurement error was around ± 100μm at 80mm. At the end it all depends on the requirements for the specific application.

a)

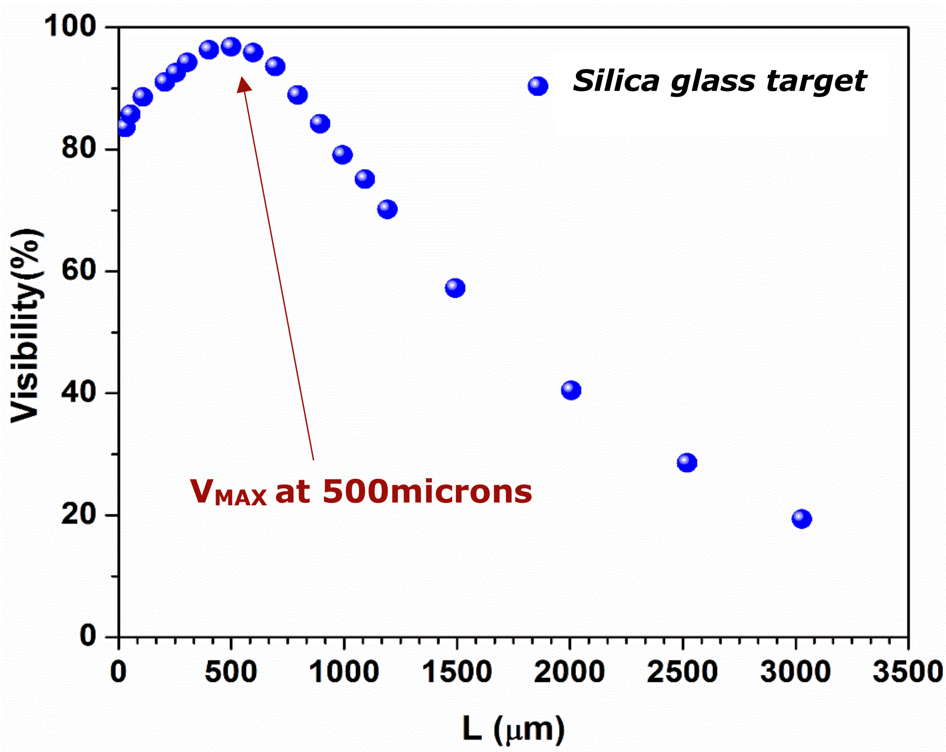

Silica glass target
VMAX at 500microns
Visibility(%)
L (μm)
0
20
40
60
80
100
0
500
1000
1500
2000
2500
3000
3500

b)

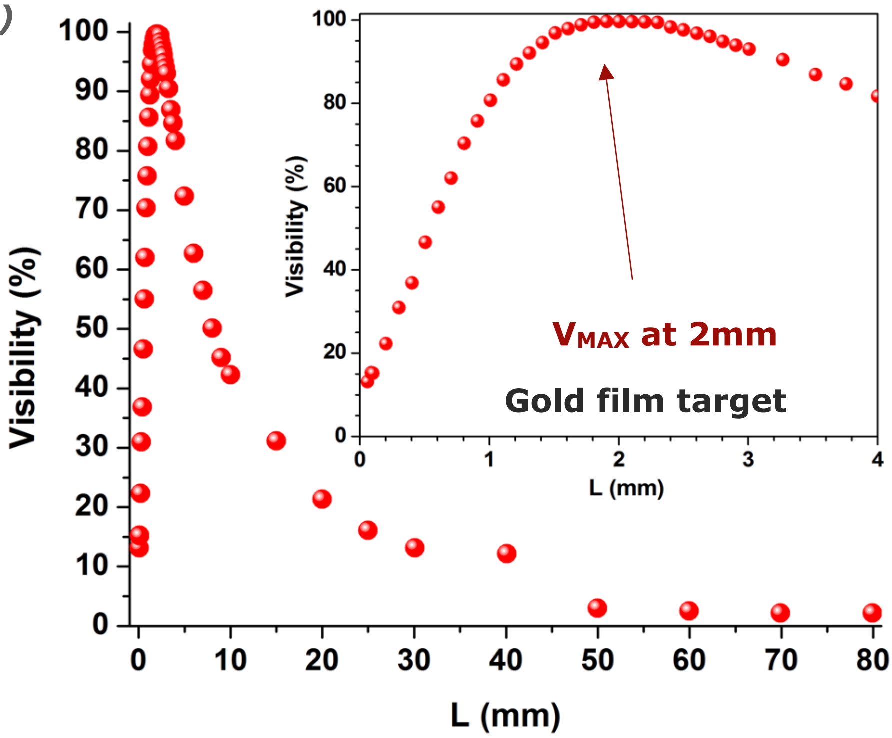

Visibility (%)
L (mm)
VMAX at 2mm
Gold film target
Visibility (%)
L (mm)

c)

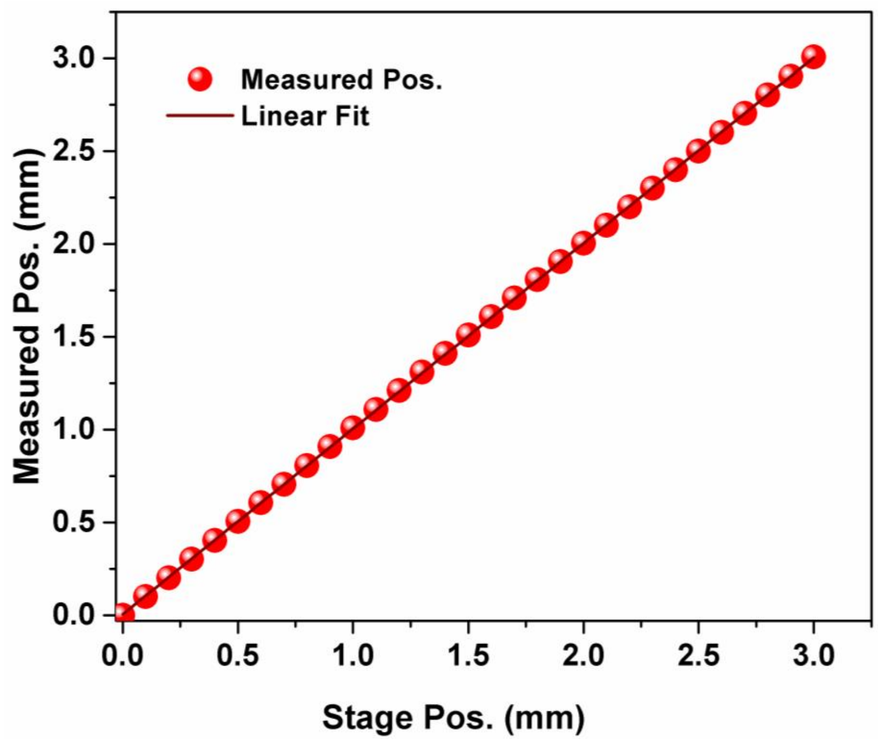

Figure 25. Result of visibility vs. cavity length L for the tapered-EFPI using (a) a fused silica glass window as reflector. (b) a high-reflectivity mirror. (c) Measured position vs. position of the translation stage in 100μm steps.

5.3 Numerical simulation

To complete this work and set the basis on future developments about long-range detection using tapered-EFPIs, a mathematical model to simulate its fringe visibility behavior with a highly reflecting target was implemented in MATLAB. The model was based on the one proposed by Zhang et al. in [33] and the equations used to run the simulations can be found in appendix B of this dissertation. It is based on the two-beam interference equation and neglects the multiple reflections that may be present in the EFPI cavity, thus it was expected to fail simulating the case of silica glass target. Fig.26 shows this, but it is worth noting that beyond the maximum visibility, the simulation approaches fairly well to the experimental results. This confirms that second reflection from the back-surface of the glass contributes improving the visibility at short lengths. Including this new reflection would be an interesting addition to the simulation for future projects.

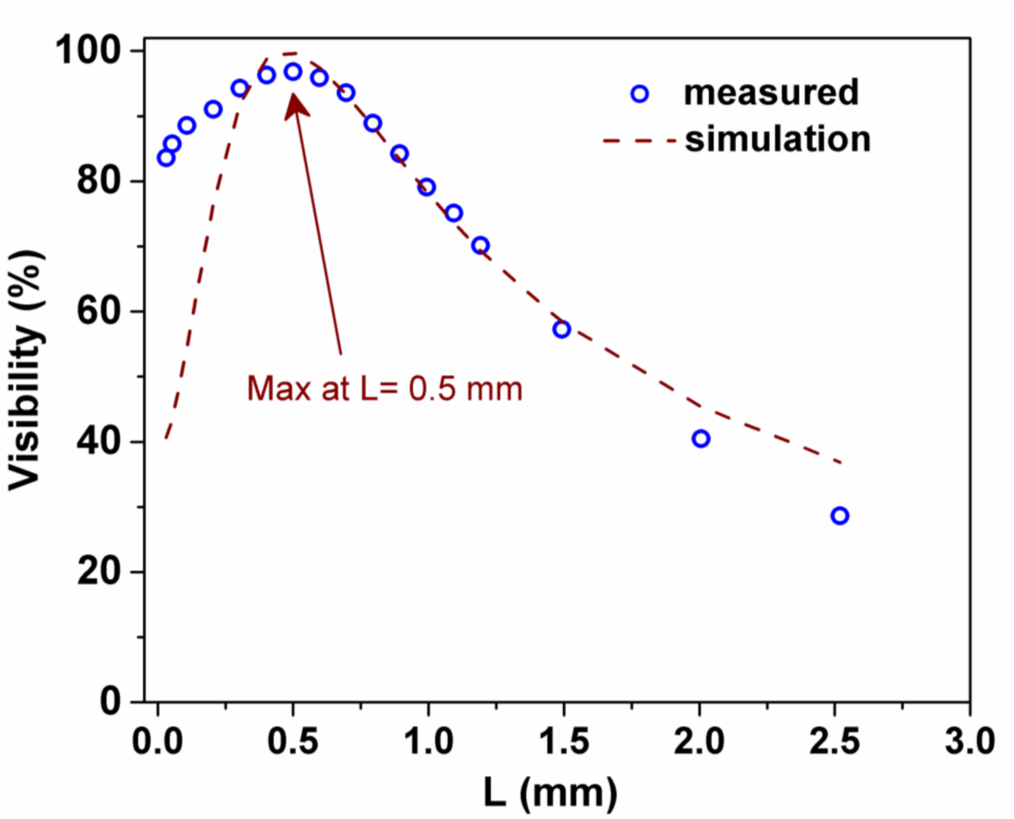

Figure 26. Theoretical visibility vs. length compared to the experimental measurements for fused silica target.

On the other side, the simulation for the tapered EFPI with a gold thin film mirror target, gave a good result. This can be appreciated in fig.27 were the visibility's simulation approaches perfectly to the experimental points represented by the light red circles. To achieve the fit from the simulation, the mode field diameter value used was 14.8μm. This value is 1.4μm higher than the one obtained using the optical fiber toolbox described in sec.3.2.

The simulation helped to confirm indirectly that the beam is expanded to a diameter closer to 14-microns, but to obtain a precise mode field diameter value it is necessary to measure it with a beam profiler (this measurement was not possible to achieve). Moreover, this simulation can help with future work concerning refractive index measurements inside the EFPI's cavity or reflectivity changes at the reflector target.

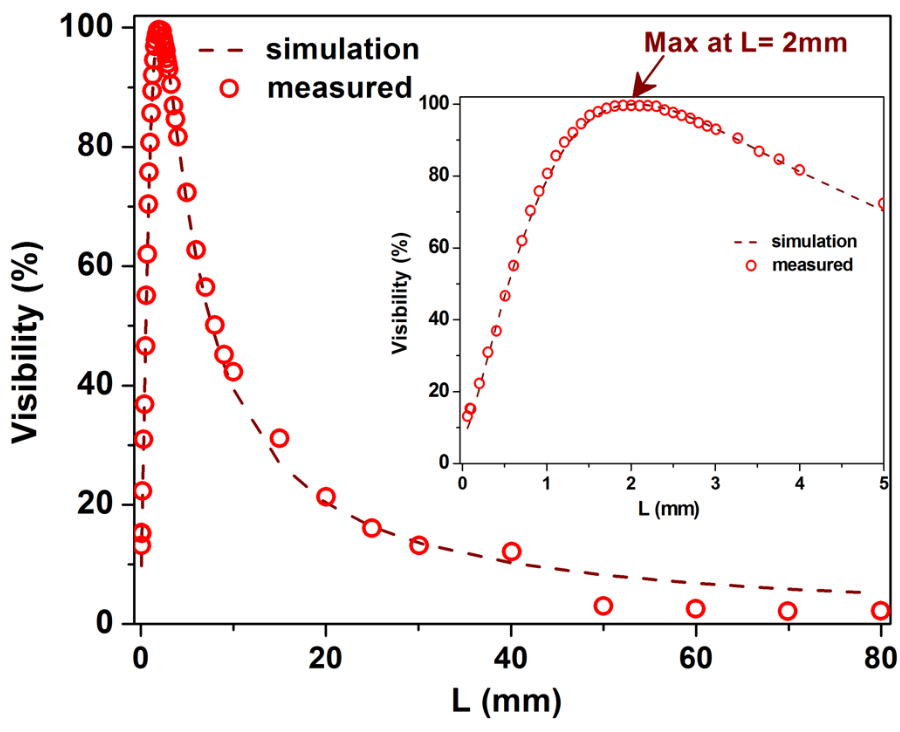

Figure 27. Theoretical visibility vs. length compared to the experimental measurements for a high-reflectivity target.

6 MEASUREMENTS OF RI AND THICKNESS OF SOLIDS

Refractive index sensing has gradually become in a powerful tool for a large range of applications in different industrial and scientific fields. Since RI is a fundamental material property[26], it can be used for identification of a specific substance, to determine the quality of a sample, or more recently, for detection of a biological agent, just to mention a few. Refractometric techniques have also experienced a rapid evolution in simplicity and performance.

Refractometers have been improved from bulky systems, whose complex optical alignment requirements make obligatory the use of high precision mechanical mounts and special laboratory conditions, to practically plug-and-play systems assembled in monolithic alignment-free structures capable of indoor/outdoor measurements. Regarding performance, modern refractometric techniques have reached a resolution of around 3 orders of magnitude higher than that of conventional Abbe refractometer. Some of the simplest, and yet highly-sensitive refractometers reported so far are built with optical fibers. Standard fibers are composed of chemically inert and bio-compatible materials, their small dimension allows to minimize the volume of sample and reactive agents, that in turn reduces the cost of each test and more important the waste of residues.

In this chapter the capability of the tapered EFPI to measure three parameters simultaneously, distance, group refractive index and thickness of transparent samples introduced in its air cavity (between fiber tip and mirror) is demonstrated. The majority of EFPIs reported in the literature so far are capable of monitoring a single parameter only [32, 52, 64, 66-70]. However, it is possible to micro-machine the fiber that forms a FPI to make it capable of monitoring or sensing two parameters, see for example [71-73]. The disadvantage in the latter case is the multistep process needed to machine the optical fiber tip. Another limitation of most EFPIs reported until now is the fact that the performance of the interferometer can be compromised with residues of liquids or polymers left on the facet of the optical fiber. Contamination of the fiber tip will perturb the reference beam, and consequently, the performance of the interferometer. In many sensing architectures reported until now the end of the optical fiber that forms the FPI cannot be completely isolated, particularly in those designed to measure refractive index of liquids. Such measurement is crucial in a number of industrial processes, analytical chemistry or biomedical analysis. A number of schemes based on optical fibers have been proposed to measure refractive index of solid, liquids, or gases. In the latter two cases, typically the optical fiber is in immersed into the sample under test [71, 72]. In contrast, for the measurement of refractive index of solid samples the use of non-contact approaches based on interferometry are widely extended. For solid samples the use of non-contact optical fiber interferometers is very common, most of these techniques have the capacity to measure refractive index group (n_g) and geometrical thickness (t)

simultaneously. Sorin and Gray proposed for the first time the use of an optical fiber Michelson interferometer to perform optical low-coherence reflectometry (OLCR) measurement to determine the t and n_g of a Tygon tubing [74]. Later, Tearney et al. [75], implemented an OCT system based on a fiber Michelson interferometer and reported measurement of refractive indexes of *in vitro* and *in vivo* human tissue. Fukano and Yamaguchi with a more complex setup proposed a combination of low-coherence interferometry (LCI) and a confocal microscope to obtain simultaneous measurements of the refractive index and thickness of a sample made of 7 cover slips with thickness of 150μm each [76]. After them S. R. Chinn et al. [77] presented a high resolution OCT system that had a fixed reference arm and a tunable source with a span of 25nm. By applying optical Fourier domain reflectometry (OFDR) they related the peak Fourier frequency, obtained from the interference spectra, with the mirror position achieving a depth resolution of 38μm. They concluded that resolution can be improved by increasing the tunable source wavelength span. Some other setups have been proposed for absolute and relative measurements of these parameters [23, 78-82]. The work of S. Kim et al. [83] consisting on a combination of a low coherence interferometer and confocal optics has become a reference since they measured the n_g and t of different glasses and films samples, at three different wavelengths, achieving errors of 0.106% and 0.123% , respectively. A simpler approach was proposed by S. C. Zilio [84], he used a single arm low coherence interferometer with a fixed reference mirror. The sample under test only covers half of the beam wave-front so the same beam is used as testing and reference signal.

The majority of the aforementioned techniques use fiber optics to carry and collect the testing beam light. Since the beam exiting the fiber rapidly diverges, thus collimating lenses are necessary. Precise translation mounts are also necessary to adjust the lenses and mirrors position for optical path difference determination [74-76].

To measure simultaneously the distance (from fiber tip), thickness, and refractive index of a solid dielectric sample, the tapered fiber tip described along the previous chapters plays a triple role in the interferometer. It provides the reference beam for the FPI, minimizes the divergence of the output beam and couples more efficiently the reflected light. By analyzing the Fourier domain reflection spectra of a FFPI, as widely explained in refs.[71, 74, 84] and in the next section, is described the possibility to establish simple relationships to calculate the n_g and t of samples of different types of glasses. Furthermore, using this EFPI is possible to measure in near real-time (10Hz data acquisition) the changes in the thickness and RI of a polymer block (Polydimethylsiloxane, PDMS,11mm thick) due to temperature changes. With this information, determination of the coefficient of the thermal expansion (CTE) and thermo-optic coefficient (TOC) of the block is possible. An important advantage of the tapered-EFPI is that it can be used to test samples composed by a stack of layers of different refractive indices and thicknesses.

6.1 Fourier domain interferometric analysis

EFPIs with long cavities make possible to introduce small dielectric blocks in them, hence it is possible to measure parameters such as thickness, roughness, or refractive index of the sample inside the cavity. The representation of an extrinsic fiber FPI in which a dielectric solid dielectric sample is inserted between the lead-in fiber and the mirrored surface is shown in fig.28a below.

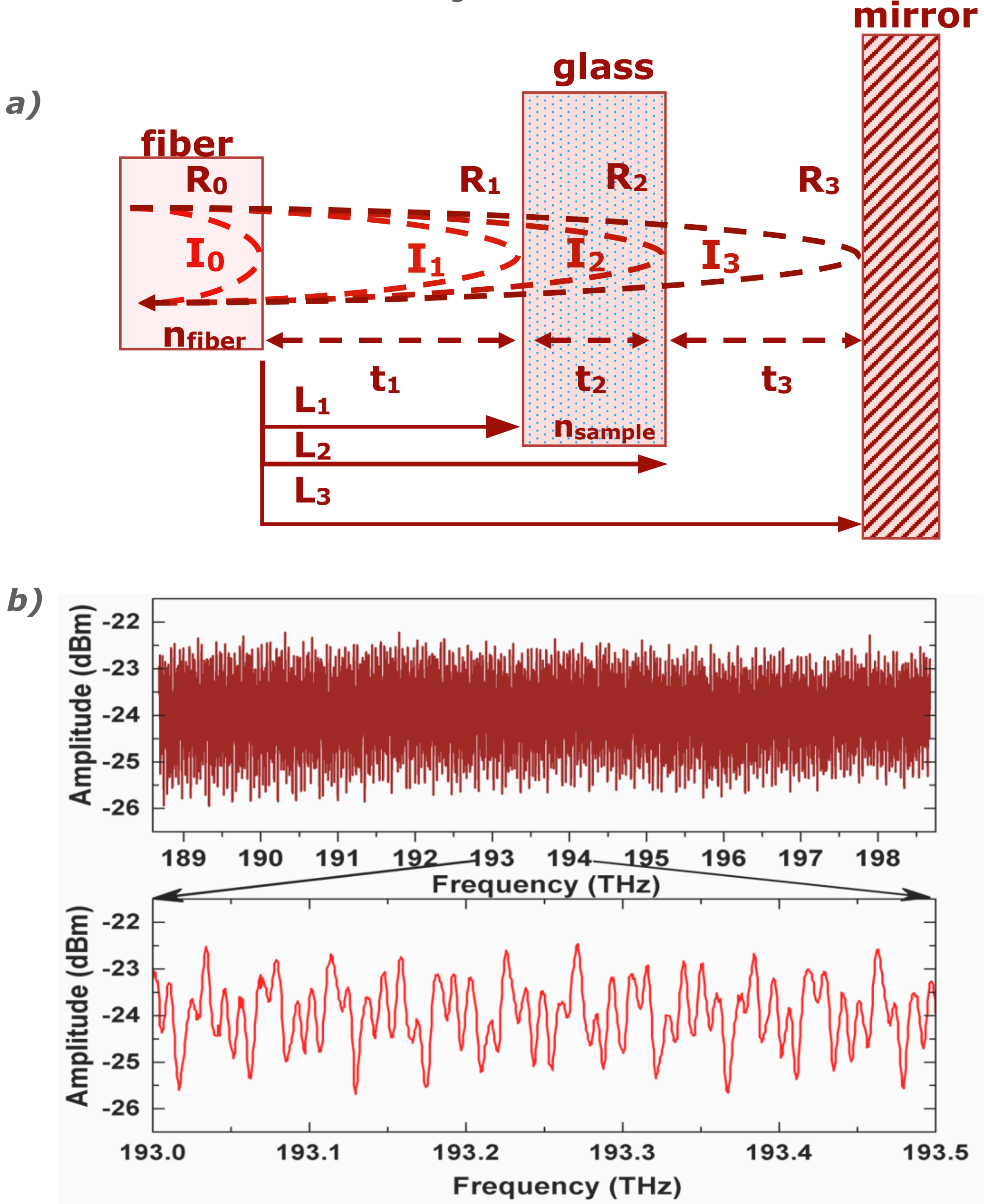

Figure 28. (a) Schematic representation of multi-cavity EFPI. I_0, I_1, I_2, and I_3 are the beams reflected from the fiber end face and the multiple interfaces. (b) Acquired optical spectrum corresponding to SF-15 glass sample showing superposition of various sinusoidal waves.

The intensity of the fundamental core mode is divided at the end-face of the fiber, about 4% of the incident intensity is internally reflected (I_0) and the rest leaves the fiber. The intensity of the transmitted beam is successively divided at each interface, whose Fresnel reflection coefficients at each interface are R_i ($i = 0, 1, 2, 3$), in reflected and transmitted signals. Each reflected beam, traveling backwards and if some conditions are met, will eventually couple back into the lead-in fiber core and interfere. In the scheme represented in fig.28a there are three interfaces inside the cavity, so three beams will return and re-couple into the fiber core (I_1, I_2, I_3). Graph in fig.28b shows the optical spectrum of the back-reflected light. The normalized reflection spectrum of the light re-coupled at the fiber core can be expressed as the interference of four beams,

$$\begin{aligned} R_{FP} = {} & R_0 + (1-A_0)^2(1-R_0)^2R_1 + (1-A_0)^2(1-A_1)^2(1-\alpha)^2(1-R_0)^2(1-R_1)^2R_2 + \\ & (1-A_0)^2(1-A_1)^2(1-A_2)^2(1-\alpha)^2(1-R_0)^2(1-R_1)^2(1-R_2)^2R_3 + 2\sqrt{R_0R_2}(1- \\ & A_0)(1-A_1)(1-\alpha)(1-R_0)(1-R_1)\cos\left[\frac{4\pi}{\lambda}(L_1+nL_2)\right] + 2\sqrt{R_1R_3}(1-A_0)^2(1-A_1)(1- \\ & A_2)(1-\alpha)(1-R_0)^2(1-R_1)(1-R_2)\cos\left[\frac{4\pi}{\lambda}(L_3+nL_2)\right] - 2\sqrt{R_0R_1}(1-A_0)(1- \\ & R_0)\cos\left[\frac{4\pi}{\lambda}L_1\right] - 2\sqrt{R_0R_3}(1-A_0)(1-A_1)(1-A_2)(1-\alpha)(1-R_0)(1-R_1)(1- \\ & R_2)\cos\left[\frac{4\pi}{\lambda}(L_1+nL_2+L_3)\right] - 2\sqrt{R_1R_2}(1-A_0)^2(1-A_1)(1-A_2)(1-\alpha)(1-R_0)^2(1- \\ & R_1)(1-R_2)\cos\left[\frac{4\pi}{\lambda}(2L_1+nL_2)\right] - 2\sqrt{R_2R_3}(1-A_0)^2(1-A_1)^2(1-A_2)(1-\alpha)^2(1- \\ & R_0)^2(1-R_1)^2(1-R_2)\cos\left[\frac{4\pi}{\lambda}(2L_1+2nL_2+L_3)\right] \end{aligned} \quad \textbf{(9)}$$

It is evident that the interference spectrum is composed by at least 6 different individual sinusoidal interference signals. In these signals, is codified the optical path difference (*OPD*) of each cavity. The *OPD* comprises the distance of each surface from the fiber facet (L_1, L_2, L_3), the thickness (t_1, t_2, t_3) and RI ($n_1=n_{air}=1$, $n_2=n_{sample}=n$, $n_3=n_{air}=1$) of each of the interferometer cavities. The power reflection coefficients at surfaces *0, 1, 2* and *3* are R_0, R_1, R_2 and R_3, respectively. $R_0 = (n_{fiber}-1)^2/(n_{fiber}+1)^2$ and $R_1=R_2=(n_{sample}-1)^2/(n_{sample}+1)^2$. A_0, A_1, A_2, and A_3 are the transmission loss factors at reflection surfaces *0, 1, 2,* and *3,* respectively. α is loss factor of the glass.

The interference pattern of the fiber FPI is wavelength codified, as it can be seen in the spectra shown in fig. 28b, the characteristics of these spectra such as fringe period and visibility mainly depend on the air-cavity optical path length.

Based on this principle, and mainly in refs. [71, 74, 84] a method was developed to measure thickness and group refractive index (n_g) of dielectric samples, glasses and polymers, using the tapered-EFPI. First, as explained in chapter 5, the interference spectra when fiber tip and mirror are separated a distance L produces a single peak in Fourier domain (spatial frequency). But, according to Pevec and Donlagic [71], when acquiring an optical spectrum in optical frequency units (e.g. THz) instead of wavelength in nanometers. And then, by applying the inverse FFT, it is obtained a temporal frequency spectrum with X-axis units in seconds. Then, the position of a peak in X-axis represents the round optical path length measured in time. Something similar to the time-of-flight (TOF) concept, used in other fields, such as acoustics or single photon detection. So, using the files of the spectra acquired for long-range measurements (fiber tip and mirror), fig.29 shows the direct relation between X-axis peak's position and optical path length. Where $OPL = \frac{c*t}{2}$, and $c = 3E8(m/s)$, without making any previous calibration.

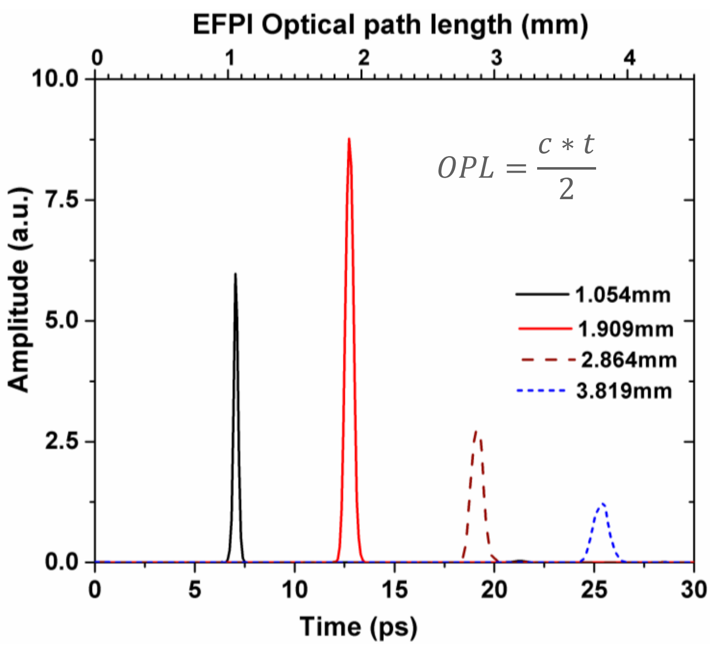

Figure 29. Temporal fringe frequency spectrum obtained for different tapered-EFPI air-cavity lengths that shows the optical path length in time(ps) and (mm).

The Fourier domain spectra (temporal fringe frequency) exhibits three peaks when a piece of SF-15 glass is introduced in the cavity (graph of fig.30). By analyzing the X-axis position of the three peaks it is possible to know the corresponding optical path lengths (related to L_1, L_2, and L_3 of schematic in fig.28a) and called X_1, X_2, X_4. After introducing the glass sample, the original peak position of the mirror, X_3 shifts right to a new position X_4. And two extra peaks appear X_1 and X_2, which represent the OPL from the fiber tip to the first and second faces of the dielectric sample, respectively.

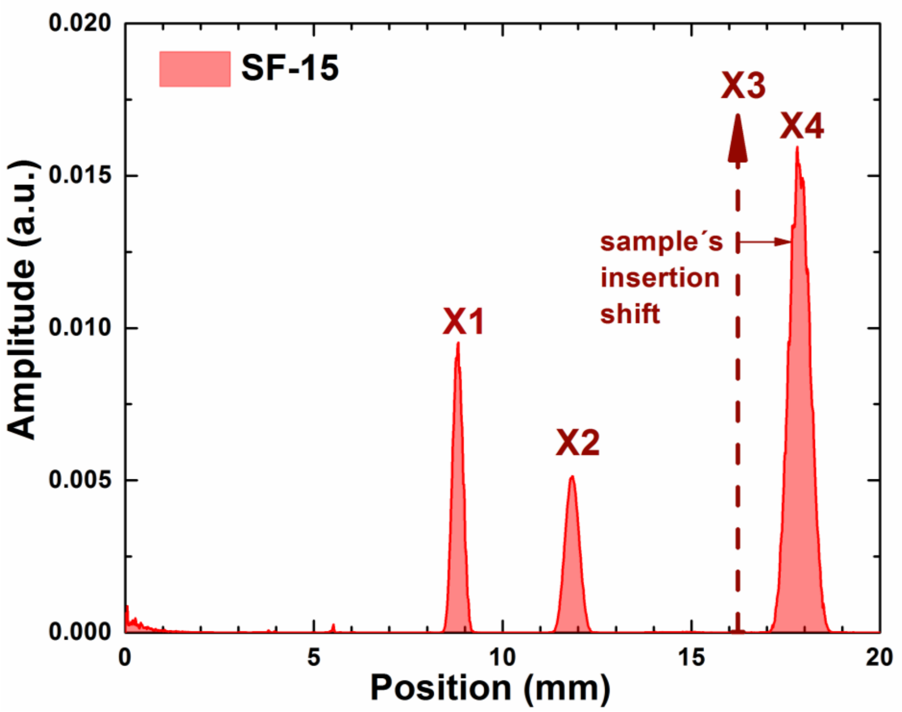

Figure 30. FFT of the optical spectrum shown in fig.27b that corresponds to an SF-15 glass sample. The X3 peak corresponds to the OPL of the air cavity (before introducing the sample in the EFPI's cavity).

Based on the analysis reported in [74] and the graph of fig.30, the optical path length difference added by the sample is as follows:

$$\mathrm{X}_1 = \mathrm{L}_1 * \mathrm{n}_{\mathrm{air}}; \quad since\ \mathrm{n}_{\mathrm{air}} \approx 1 \tag{10}$$

X_1 is the distance to the sample.

$$X_2 - X_1 = (L_2 - L_1) * n_{sample} \tag{11}$$

where the $thickness_{sample}$ = (L_2-L_1), before introducing the sample, there was only air inside the cavity. Thus the X_3 shift to X_4 is due to the refractive index change from n_{air} to n_{sample}, giving:

$$(L_2 - L_1) \cdot (n_{sample} - n_{air}) = X_4 - X_3 \tag{12}$$

and to obtain the sample's geometrical thickness,

$$thickness = (X_2 - X_1) - (X_4 - X_3) \tag{13}$$

Using the definition of optical path length difference between two beams interfering in both edges of the sample,

$$OPD = X_2 - X_1 = n_g * thickness \tag{14}$$

then the group refractive index of the sample is obtained with

$$n_g = \frac{X_2 - X_1}{thickness} \tag{15}$$

6.2 *Glasses measurements and results*

Using the setup shown in fig. 31, the fiber tip was mounted in a translation stage (NanoMax-343M/Thorlabs) at approximately 14mm from the mirror, the swept-laser light source and photodetector are inside the FBG interrogator (sm-125, Micron Optics). The stage and interrogator were controlled by the computer using a customized LabVIEW program.

A set of round windows with 2.5mm in diameter and thickness≈1.8mm made with 6 different types of glass, machined and polished in the facilities of the C.I.O.,A.C. [51]; fused silica, BK7, BalF5, SF2, BaF51, SF15, and a glass slide and glass cover made by Corning were used to test the tapered-EFPI.

The measurement procedure starts with the empty cavity, then acquiring the optical spectrum, apply the FFT and save the X_3 position value. Next, insert the glass sample, acquire the spectrum, apply the FFT, saving X_1, X_2, X_4 *position values*. Finally, with this values and the relations (10)-(15), the distance to sample, geometrical thickness and the group refractive index of the glass were calculated. This process was also included in the LabVIEW program.

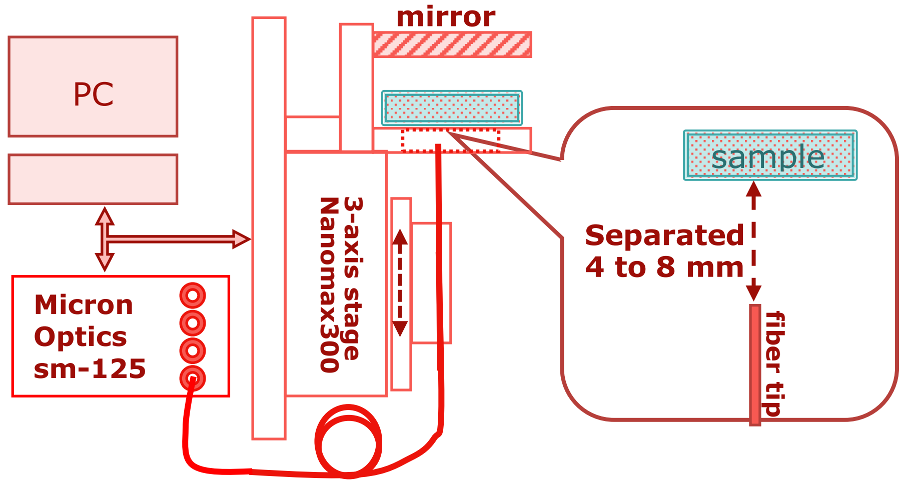

Figure 31. Schematic experimental setup for glass samples measurement.

The values measured are shown in Table 5. Each value in the table represents the average of the 9 measurements obtained for two samples of each type in a range from 4 to 8 mm separation from fiber tip to sample with steps of 500-microns.

Table 5. Results for thickness measurements compared with a micrometer reading. Results for group refractive index measurements obtained with the method proposed compared to the theoretical ng at λ=1550nm.

¶

Thickness (mm)

Glass	Sample	Reference	%Error
Silica	1.8088	1.809	0.025
BK7	1.8074	1.808	0.059
BaLF-5	1.7964	1.797	0.060
SF-2	1.7686	1.769	0.045
BaF-51	1.8231	1.823	0.012
SF-15	1.7959	1.796	0.010
Glass Cover	0.1941	0.194	0.01
Glass Slide	1.1481	1.148	0.01

Group refractive index(ng)

Glass	Ref.	Sample	%Error
Silica	1.4626	1.464	0.105
BK7	1.5201	1.520	0.006
BaLF-5	1.5488	1.547	0.157
SF-2	1.6424	1.642	0.042
BaF-51	1.6490	1.648	0.080
SF-15	1.6909	1.689	0.165
Glass Cover	-	1.5186	-
Glass Slide	-	1.5126	-

From the table 5 above, it can be observed that the error of the thickness measurements is lower than 0.1%, and the lowest thickness error corresponded to the SF-15 sample with 0.010%. The uncertainties can be caused by the different surface finishes that each sample presents because they were polished in batch regardless of the hardness of each type of glass. But also was found that when the OPD of the sample was larger, the error decreased in both, thickness and group refractive index measurement. The SF-15 sample was used to study the variations of *thickness* and n_g measurements compared to the reference values at different distances from fiber tip. Fig.32a shows the corresponding measurements. It can be seen that for L >5 mm the difference between measured and reference values starts to increase but even in such cases the error is lower than that reported in literature using other methods [83, 84]. In the graph of fig. 32b the measurement behavior through an 80-minute period of time is shown, the n_g variations < $1x10^{-4}$ RI units.

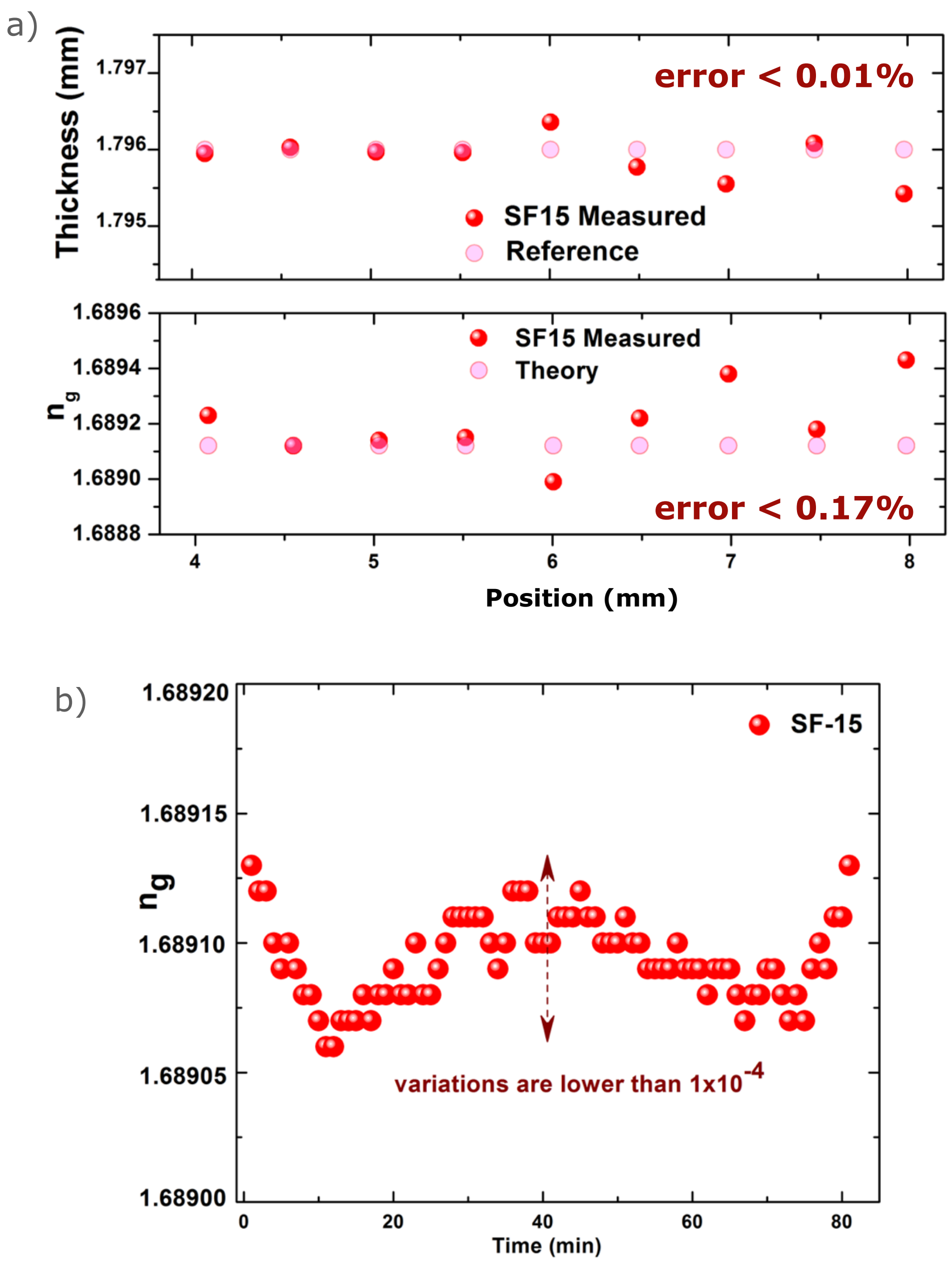

Figure 32. (a) Results of measurements of thickness and group refractive index for SF-15 glass sample, when sample is at different distances from the fiber tip. (b) Variation of the n_g measurements of the SF-15 sample along 80 minutes.

6.3 Thermal expansion and thermo-optic coefficient determination

An application of the tapered-EFPI that arisen after obtaining the measurements described in the last section will be described here, interferometric measurements of the coefficient of thermal expansion (CTE) and the temperature coefficient of the refractive index (dn/dT).

Both CTE and dn/dT can be obtained simultaneously from a single spectrum acquisition which minimizes the errors that can occur in two separate measurements. For example, exact values of these coefficients are necessary in order to calculate thermal lensing of crystal laser cavities [85].

It is known that polydimethylsiloxane (PDMS) elastomer (Dow Corning- Sylgard 184) has a large thermo-optic coefficient, this property allows to investigate the capability of this extrinsic interferometer to measure dynamic changes of the refractive index in parallel to its longitudinal expansion.

6.3.1 Simultaneous measurements and results

First, a rectangular block of polydimethylsiloxane was prepared by mixing the two liquid components and then pouring the mix inside a glass container assembled with glass slides. After the curing time, about 24hrs. at 30°C, the container was disassembled and the polymer block was extracted. Then the experimental setup was arranged as shown in fig. 33a, and also a custom LabVIEW program was developed to control the translation stage to move the fiber tip, acquire the optical spectra from the sm-125, apply the FFT, display the spectrum, search peaks position, and calculate and display simultaneously the refractive index and thickness on the computer's screen. A gold film mirror, in direct contact with the PDMS was used as a reference surface. Then, the fiber was placed in position 1(fig.33a), aside of the polymer, to obtain the reference peak, this is needed only the first time. Then, the fiber was moved to position 2, over the polymer. The corresponding peaks are shown in fig. 33(b).

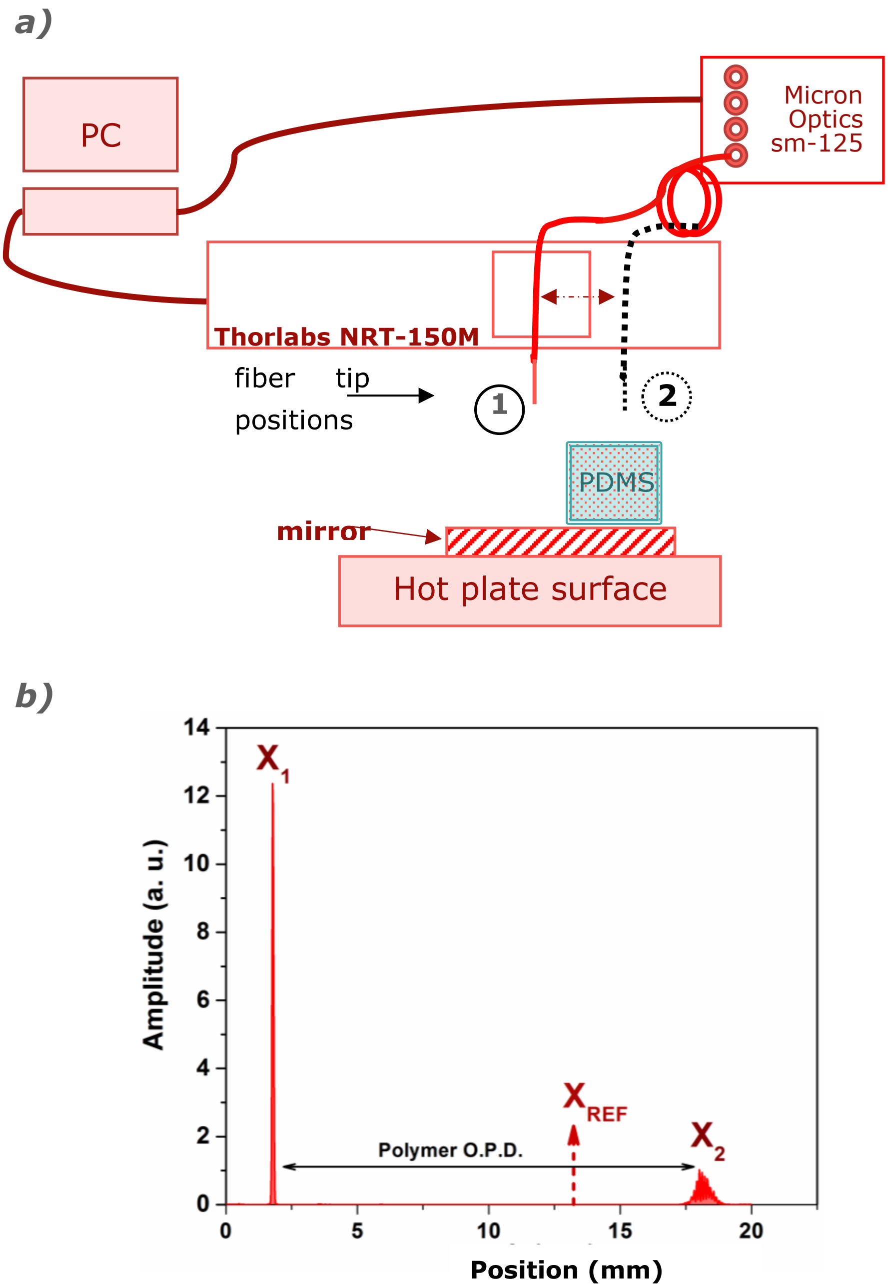

Figure 33. (a) Schematic diagram of the setup used to determine CTE and dn/dT of a PDMS block. (b) Graph of the corresponding Fourier domain peaks, X_{REF} indicates the optical path length in air (fiber position 1 of scheme (a)). X_1 and X_2 appear at position 2, they show the optical path length difference due to the PDMS.

Every peak position was saved, and based on eqs. (13) and (15) it is possible to find the PDMS's thickness, because the polymer is in contact with the mirror (X_2=X_4); and X_3 = X_{REF}. This gives,

$$thickness_{PDMS} = (X_{REF} - X_1) = 11.745mm \tag{16}$$

and

$$n_g = \frac{(X_2 - X_1)}{thickness_{PDMS}} = 1.3983 \tag{17}$$

This refractive index value is very close to the one reported by the manufacturer which is 1.3997 at 1554nm at 25°C.

After obtaining the starting thickness and refractive index of the polymer sample, it was heated, and its temperature went from 25 to 90°C, simultaneously both variables (*t* and n_g*) were* calculated by the program following the equations described and locating peaks X-axis positions as the temperature raised.

Fig. 34 shows the results, a linear change of thickness and n_g due to temperature increase gave a coefficient of thermal longitudinal expansion α= 4.71x10^{-4}/°C and a thermo-optic coefficient dn/dT=−4.67x10^{-4} RIU/°C. The latter value agrees well with the thermo-optic coefficient of the elastomer -4.5x10^{-4}/°C reported in [86]. Since polymer was not comprised in a container it is right to say that this change of the geometrical thickness measured is the actual thermal expansion coefficient.

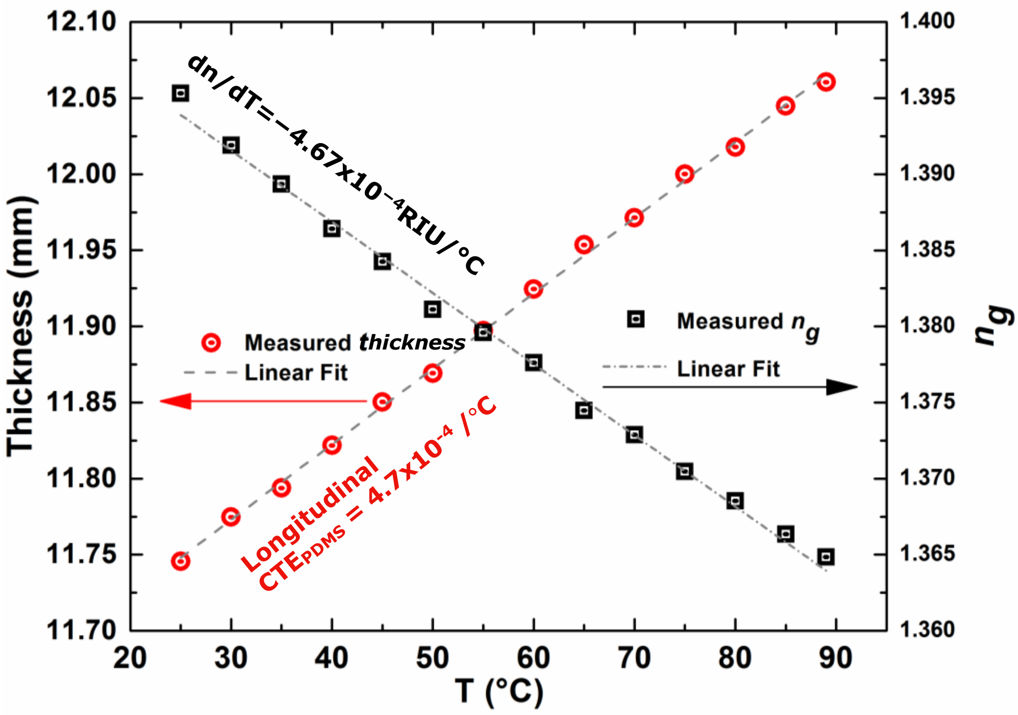

Figure 34. Experimental results for temperature vs. thickness and refractive index of an 11.7mm PDMS block measured with the tapered-EFPI.

6.4 In-depth layer profiling

Using the same interrogating system described previously, the tapered fiber tip was fixed on to a 3 axis motorized stage in order to move the fiber in one direction along the surface of a spectrophotometer flow cell (Starna cell, type 49/G) which consists of two walls of glass and an inner cavity (fig.35b). The process starts by placing the fiber tip at approximately 9 mm away from cell surface, the FFT spectrum presents 4 peaks corresponding to the positions of the first and second surface of the front glass and the first and second surface of the back glass of the sample. The peak positions were identified and saved, then the fiber tip was displaced 0.2 mm along the transversal axis of the sample, the process is repeated for 30 different points along the cell surface. The depth profile of each of the surfaces of the sample was obtained, for instance the mean value for the air cavity obtained from this measurement was L=0.996mm closer to the optical path of 1mm that the manufacturer claims. In fig. 35(c) it is shown an area plot of the different mediums that constitute the cell, the glasses surfaces positions and air cavity dimension. With the setup it can be measured refractive index and thickness of dielectric structures with more than one interface, then it is possible to use it for sample depth profiling/imaging.

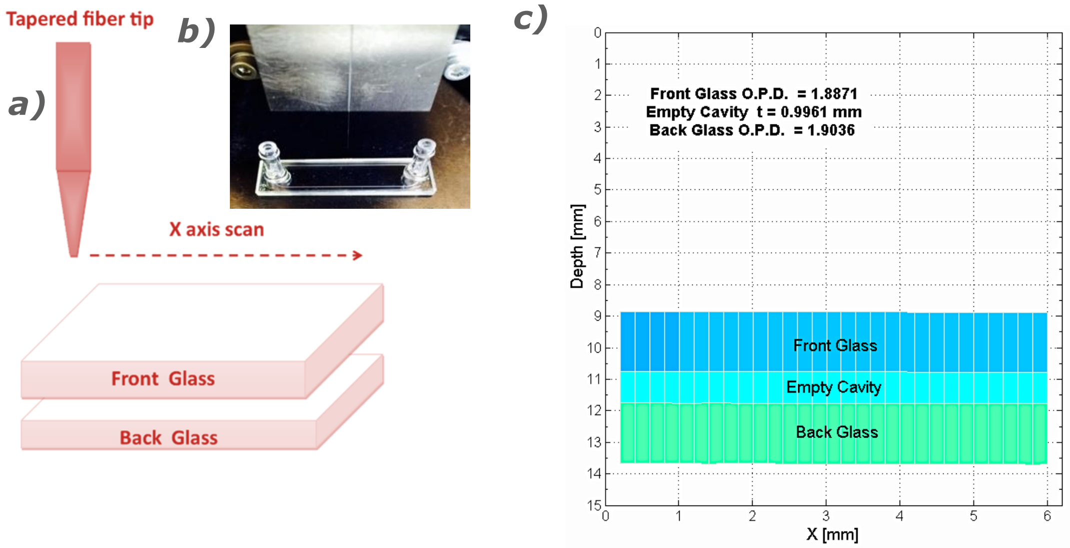

Figure 35. (a) Drawing of the sample and fiber tip showing the scan direction. (b)Picture of the glass cell and mounted fiber. (c) Image obtained by plotting all the points as a surface, the cavity length corresponds to the 1mm path length given by the manufacturer.

6.5 Conclusions

The possibility of carrying out simultaneous measurements of thickness and refractive index of solid samples was demonstrated. Furthermore, differences between measurements with glasses and the actual values are less than 0.17% for the two measurements.

The capabilities of our sensor to measure these two parameters was used to perform simultaneous measurement of the change of refractive index and thickness of PDMS block due to temperature changes. With the values obtained with this experiment the thermo-optic coefficient (dn/dT) and thermal expansion coefficient of the PDMS were calculated. Measurements performed with the PDMS sample to obtain the thermo-optic coefficient (dn/dT) present a difference of $1.7\text{x}10^{-5}$ RIU compared with a previously reported value for λ=1550nm. On the other hand, the calculated valued for the coefficient of linear expansion (α) presents a difference of $1.3\text{x}10^{-4}$ compared to the value provided by the manufacturer, considering ideal curing and mixing conditions.

The tapered-EFPI has several important advantages including flexibility, miniature size and multiplexing capability among others. These advantages can simplify the measurements for thermal expansion and/or dn/dT determination of some materials.

Furthermore, the possibility of in-depth layer profiling was demonstrated. Even though there are specialized systems to make this measurement such as OCT systems, the results obtained give a plus to develop more applications based on the tapered-EFPI system described.

Appendix C contains data of some transparent film thickness measurements made with the same interrogation system but with the sensing lead-in fiber in direct contact with the sample, this is reported here to demonstrate the measurement flexibility of the system.

7 RI MEASUREMENTS OF LIQUID SAMPLES

Here it is proposed and demonstrated a non-contact method to measure the water content in ethanol solutions using fiber optics. The scheme is based on a simple EFPI. To implement it, an optical fiber sensing instrument, a single-mode optical fiber tip, and a liquid container, are required. The light leaving the optical fiber tip traverses the container (a glass flow cell), however, at every interface of the sample-container a small amount of light is reflected and recoupled into the optical fiber tip. These reflected beams contain information of the cell glass cover and liquid sample´s optical properties. Several samples with different proportions of water and ethanol were prepared and measured; the analysis of the reflection spectra was carried out in the Fourier domain which facilitates real-time measurements as described in previous chapters of this dissertation.

The contactless technique here proposed can be used for real time monitoring of water in ethanol solutions but it can also be extended to monitor the water content in other organic volatile compounds.

The demanding purity requirement of ethanol has encouraged the scientific and technological research to develop cost-effective, fast, simple, and reliable sensors for quantifying low content of water in ethanol. As reported by Omido et al., the basic quality control test for ethanol samples is based on the determination of the water content [87]. For this purpose, a number of techniques and detectors based on different technologies, including fiber optics, have been developed so far [87-103]. Optical fibers have some important advantages for determining adulteration of ethanol over other commonly used techniques. They are inherently safe due to the lack of sparks, and a small amount of sample and/or reagent are needed to carry out a test (micro/nano-liter scale). A small sample and/or reagent volume needed to carry out a test is advantageous because the volume of residues is also minimal. An additional advantage of optical fibers is the fact that they are compact, lightweight, and immune to environmental electromagnetic noise. In addition, point or multi-point monitoring systems can be implemented which can be important in an ethanol production line.

Most of the optical fiber sensing schemes proposed until now to determine ethanol adulteration are based on evanescent wave interaction [87, 88, 90-93, 95, 99, 102]. In the simplest scheme, an uncoated fiber device, like etched fiber Bragg grating[92], long-period grating [88], or cladded multimode fiber[90, 93], is used to measure the refractive index changes of solutions due to the changes of ethanol concentration. Another approach is to develop specific ethanol sensors based on chromatic reagent layers [95]. In these sensors the optical fiber is coated with a thin film, for example with silver-graphene nanocomposites[87, 99] or carbon nanotubes[91], whose optical properties are modulated by the ethanol concentration. Although coated-fiber sensors are highly sensitive, they exhibit a slow response time. An important disadvantage of most optical fiber sensors is the fact that the optical fiber is in contact with the solution under test. Therefore, the sensor (optical fiber) must be cleaned before and after each test. In some situations, the cleaning of the sensor can be complicated, or even, impossible. Besides, in the majority of fiber optic sensors the influence of temperature is an issue, since, in general, the refractive index of a liquid varies with temperature. Most optical fiber sensors used for ethanol adulteration reported do not take into account the temperature effects on the measurements.

7.1 Ethanol-water samples preparation and characterization

Water-ethanol solution samples were prepared using distilled water and ethanol (99.5% pure) purchased from Karal (Mexico). They were prepared using two micropipettes with an accuracy of 0.1 µl. Each sample had a total volume of 1 mL. The concentration of water in ethanol was varied by 0.5%, 2%, and 10%, and then in steps of 10% up to 90%. Since water exhibits a strong absorption peak in the wavelength band in which the tapered- EFPI was interrogated, the absorbance of each sample was measured in transmission from 1300 to 1650 nm in a quartz cell with an optical path of 1 mm using a spectrophotometer (Cary 5000 UV-Vis-NIR from Agilent Technologies). In fig. 36 the transmission spectra observed for different concentrations of water in ethanol is shown. It can be noted from the figure that absorption increases as the water content in ethanol increases. The changes in transmission are approximately linear at 1350 and 1550 nm. At 1450 nm the changes in the transmitted spectra are more prominent. Although the aforementioned spectrophotometer can be used to quantify the water content in ethanol in laboratory conditions, it is not suitable for field applications. This was used for calibration purposes only.

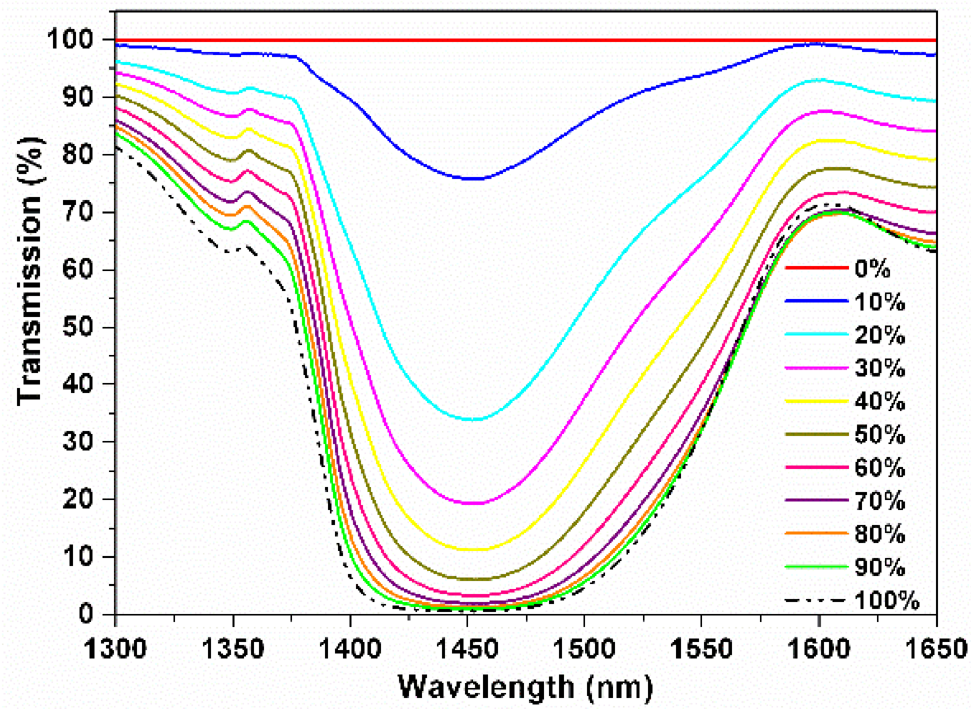

Figure 36. Transmission spectra of ethanol-water samples with different concentrations of water.

7.2 Measurement of optical properties differences of ethanol-water samples

The setup is shown in fig. 37, it consists of a demountable liquid flow cell (Starna, type49) with an optical path length of 1 mm. The cell consists of two parts; the bottom part is a rectangular glass with a machined cavity that defines the path length. The top part is also a rectangular glass but thinner than the bottom one (*t=1.25mm*) and has two glass tubes (in/out ports). The overall cell capacity is 200 µL, but the minimum sample volume to achieve a correct measurement with the system here proposed was 17 µL. An aluminum film with 110nm in thickness was deposited, by physical vapor deposition (PVD), over the inner face of the top part of the cell. Thus, the coated segment of the cell provides a highly reflective surface for the interferometer, see fig. 37. The fiber tip used is a cleaved single-mode fiber which was placed in close proximity with the bottom part of the flow cell. In this way it was ensured that the air cavity between the fiber tip and the bottom part of the cell was smaller than a couple of microns. With this condition it can be considered that the first cavity of the EFPI is the glass and the second one is the sample's cavity that ends at the aluminum mirror.

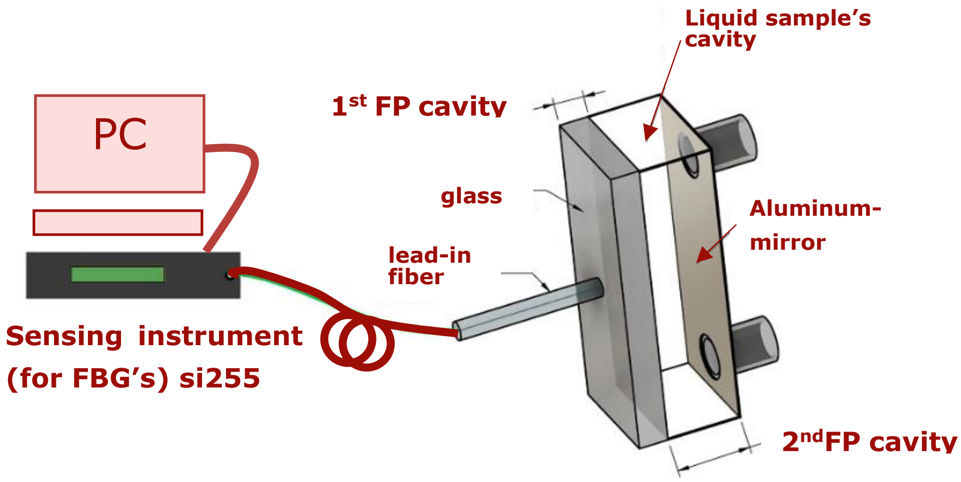

Figure 37. Schematic representation of the dual-cavity EFPI and its interrogation. The position of the optic fiber tip is indicated in contact with the glass.

For interrogating the multiple-cavity interferometer, a fiber Bragg grating sensing instrument (Micron Optics, si255) was used. The latter is composed by a tunable laser (1460-1620 nm) and a synchronized photodetector that acquires 1000 spectra per second (which means 1 kHz sampling rate). Another LabVIEW program was developed to acquire the optical spectra, calculate the FFT, search the position and amplitude of the FFT peaks, and making the refractive index calculations.

Fig.38a shows the typical spectra obtained with this interrogation system when the cell was filled with air, distilled water or ethanol. Fig.38b shows the corresponding FFT peaks for each case. It can be noted that there are two well defined FFT peaks. Peak X_1 represents the glass 1st FP cavity, and it appears first. This peak is expected to maintain the same *X-axis* position along the measurements since there are no perturbations that affect the glass optical properties. Peak X_2 is due to the 2nd FP cavity and its shift is the one that will serve to indicate the optical path length difference due to the sample´s RI compared to air´s refractive index, see Fig. 37. Then, the high-reflectivity mirror of the 2nd FP cavity contributes to increase fringe visibility in order to achieve a higher resolution in the measurements. Because, as mentioned in chapter 5, the interferometric system measurement error is lower when the fringe visibility is high.

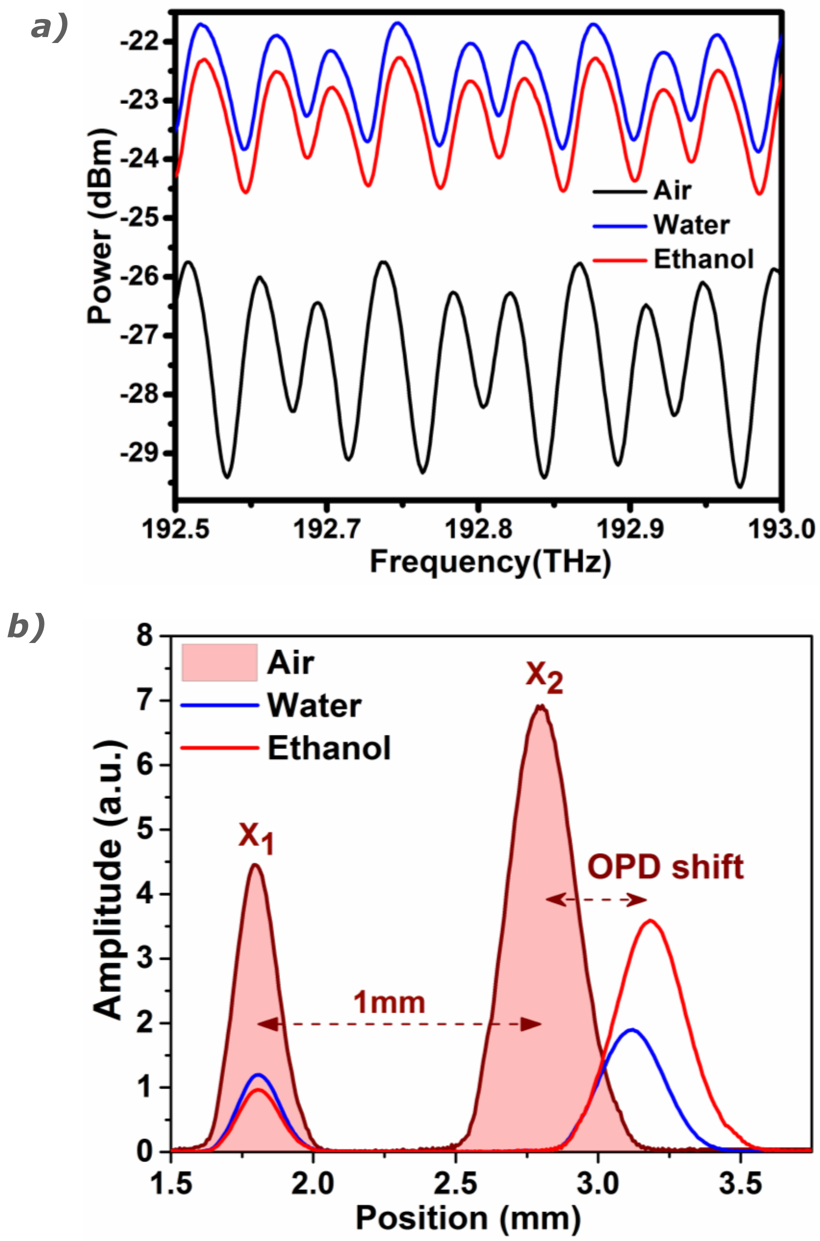

Figure 38. (a) Reflection spectra observed for different liquids in the cell or second cavity of the FPI. (b) FFT of the optical spectra shown in (a). OPD is optical path difference.

When the cell is air filled, it's optical path length is given by the *X-axis* position of X_1 andX_2,

$$sample's\ cavity\ length = X_2 - X_1 \tag{17}$$

For this flow cell the optical path length measured in air using this setup is 1mm, value that agrees well with the reported by the manufacturer.

The cavity length remains constant along the liquid samples measurements, then, it is expected that the peak's X_2 amplitude and position varies for each different sample.

The sample's refractive index is given by,

$$n_g = \frac{X_2 - X_1}{1(mm)} \tag{18}$$

where X_1 and X_2 are the X-axis positions of each one of the peaks in Fourier domain when cavity is full with the sample under test. This relation was used to calculate the group refractive index of liquid samples using this interrogation scheme.

7.3 Results

The samples characterized in the UV-Vis-NIR spectrophotometer mentioned above were used. First, the position of the fiber tip along the flow cell bottom was fixed. Once this was done the reflected interference spectrum of the air filled cell was recorded, black line of fig.38a. As expected, the spectrum is composed by the superposition of two sinusoidal modulations due to the two cavities that form the EFPI. In Fourier domain the two mentioned peaks can be distinguished, fig.38b. Then, using 17 μL of water as sample, the reflected interference spectrum was measured, blue line plot in fig.38a. Different from the optical spectra, in the Fourier domain the variations between the two cases are much more evident. The position of the first peak is unaltered since the glass wall (1^{st} FP cavity, X_1) of the cell does not change (as expected). On the other hand, the amplitude decreases since the reflection coefficient of the interface glass-water is lower than that of an interface glass-air. The notorious shift of the second peak is due to the increment of the optical path length of the cavity, $n_{water} \cdot L > n_{air} \cdot L$. The peak amplitude decreases since the intensity of the beam decreases due to the water light absorption. The measured value was n_{g_water}=1.303. The water was removed and the cavity cell was cleaned with isopropanol and then dried with nitrogen. Such cleaning process was carried out in each measurement. After this, the cavity was filled with ethanol and the reflected interference spectrum was acquired and analyzed. The reflection spectrum is shown in red in the plot of fig.38a. Again the position of the first peak is unaltered, but the intensity decreases since the refractive index of ethanol is higher than that of water. Peak X_2 is shifted and the amplitude increases with respect to the same peak of water. The OPD shift is because $n_{ethanol} > n_{water} > n_{air}$. Then, the measured ethanol refractive index was $n_{g\_ethanol}$=1.3687. About the amplitude, it increases because optical absorption of ethanol is negligible compared with water, see the absorbance spectra of fig.36. As it was mentioned previously, the characteristics of the interference patterns are determined by the refractive index and absorption coefficient of the sample under test.

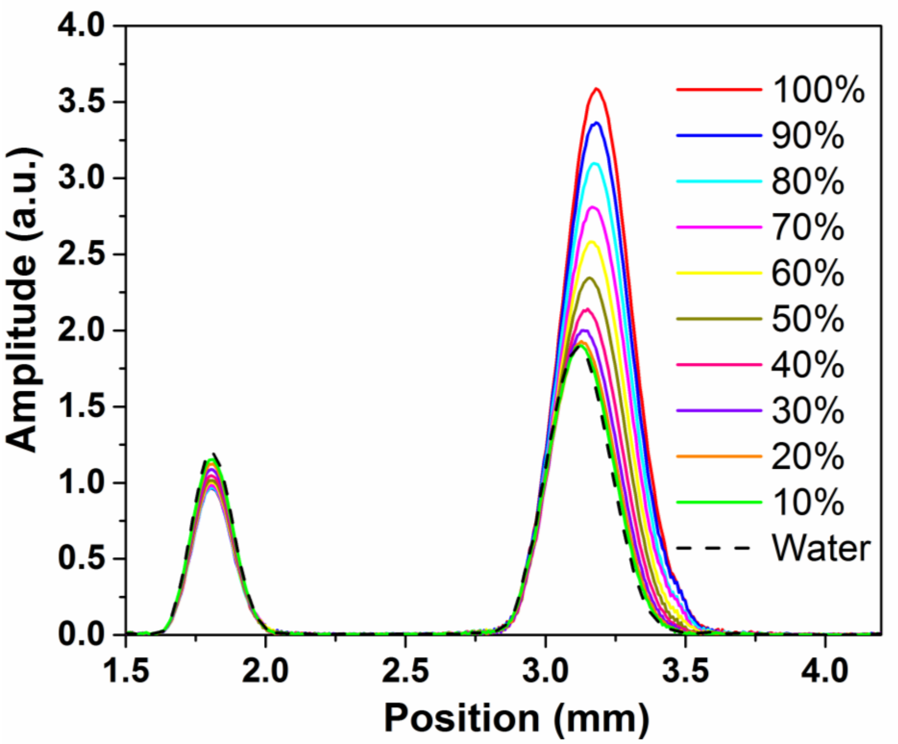

Figure 39. Calculated FFT spectra for the water-ethanol samples. Ethanol (red line) has the 2nd peak higher amplitude and water (black dashed) the lower, as expected.

In fig.39, the different samples' interference spectra in the Fourier domain is shown. There are two peaks; X_1, centered at 1.8mm, is produced by the beam reflected at the interface between the glass and sample. Peak X_2, located around 3.12mm, is produced by the 2nd FP cavity, see Fig. 37. The position and amplitude of the peaks give information about the water-ethanol concentrations. The amplitude of the second peak diminishes as the amount of water in ethanol increases. This is due to absorption of water in the wavelength region in which the spectra were monitored. Note that these measurements agree well with those carried out with the spectrophotometer, see Fig. 36. X_2 peak also shifts towards lower values in the *X-axis* as the water content increases. This shift indicates that the optical path length decreases. Since the physical length of the cavity is fixed (1 mm), the shift is due to the decrement of the refractive index of the sample as the concentration of water increases.

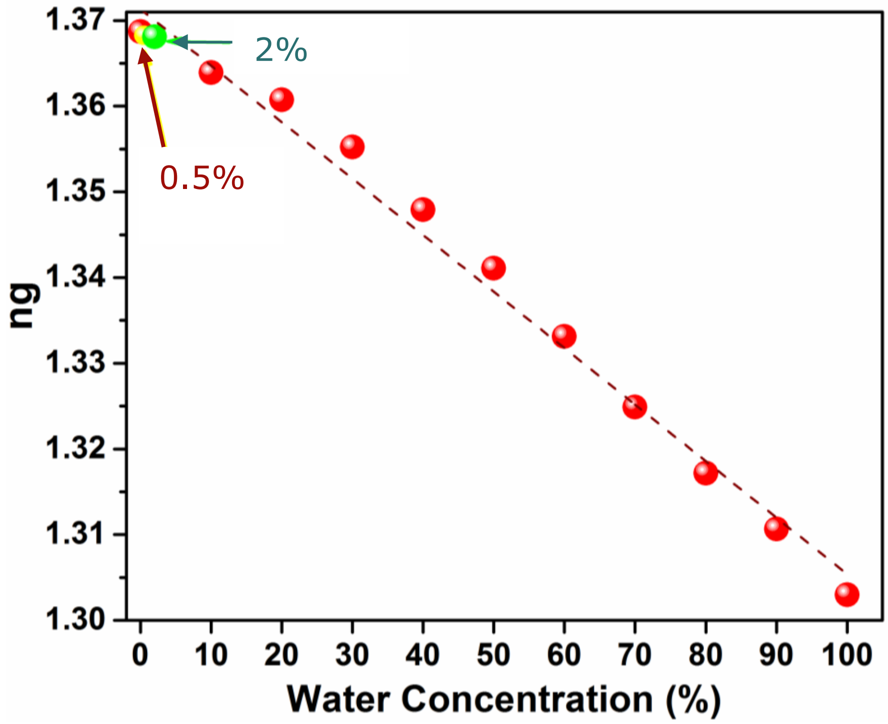

Figure 40. Resulting n_g vs. water concentration

The separation between the two Fourier domain peaks is the sample´s optical path difference (OPD), this difference decreases as the ethanol concentration decreases as fig.40 shows. Also in this figure the position of the peak decreases linearly with the refractive index of the sample. The green and yellow filled points correspond to

2% and 0.5% of water in ethanol, respectively. This small difference concentration can be perfectly differentiated in the data acquired and in the plot, and the linear fit regression gives a Pearson´s R = 0.99. Ten consecutive water measurements were made to obtain the repeatability of the system, obtaining an $n_{g_std.\ dev.}=2x10^{-4}$RIU and an $amplitude_{std.dev.}$=0.143(a.u.). These values provide the confidence for the measures presented in figs.40 and 41.

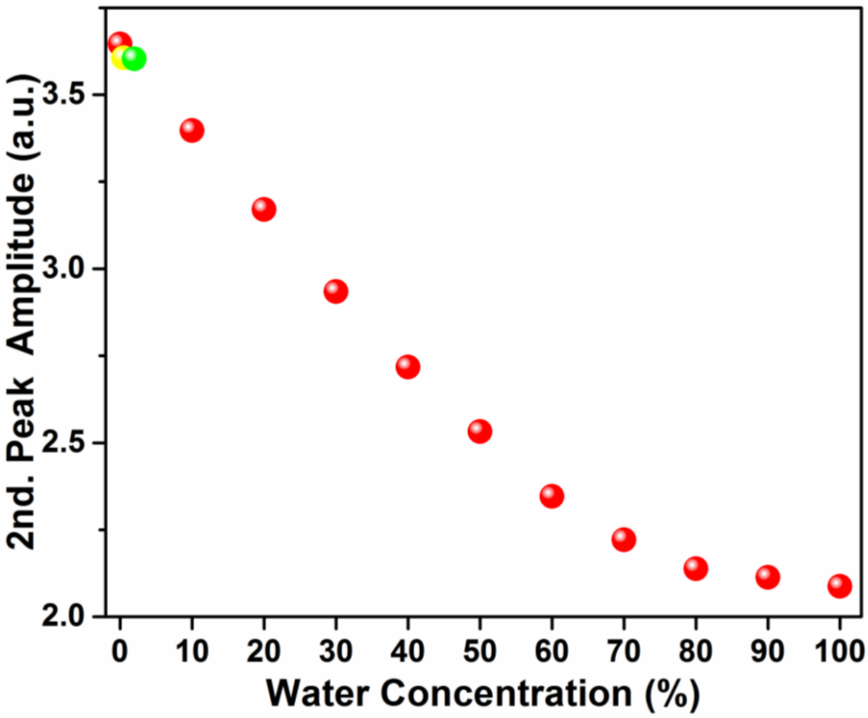

Figure 41. Amplitude of the second FFT peak as a function of water content in water-ethanol solutions.

It is important to notice that this sensor is truly non-invasive since the samples never were in contact with the fiber tip as it is located outside the cell. This unique feature was exploited to demonstrate the capabilities and versatility of the system to carry-out a real-time measurement.

A peristaltic pump (Masterflex 7519, Cole-Parmer) and a volumetric pipette were added to the setup described above. A schematic representation is shown in fig. 42. The fluidic circuit was filled with 8 ml of distilled water, the pump speed was 1ml/s. When water was flowing started the program starts the acquisition and 1ml of ethanol was added for each step of the inline measurement except for the last one that was 2ml. The program was modified to track the amplitude of the highest FFT peak. Fig.43 shows the amplitude of the peak as a function of time for increasing ethanol concentration in water. The changes observed in the amplitude of the mentioned FFT peak are in good agreement with those obtained in the static experiments. From the values of Fig.43 it is possible to determine the time response for the measurements which is around 1 second. This time includes the time of the computational calculus, average filtering, and the display of the graph in the computer. The processing time could be reduced by improving the software routine and/or a faster computer. It is also possible to follow the X-position of the peak and obtain a similar graph.

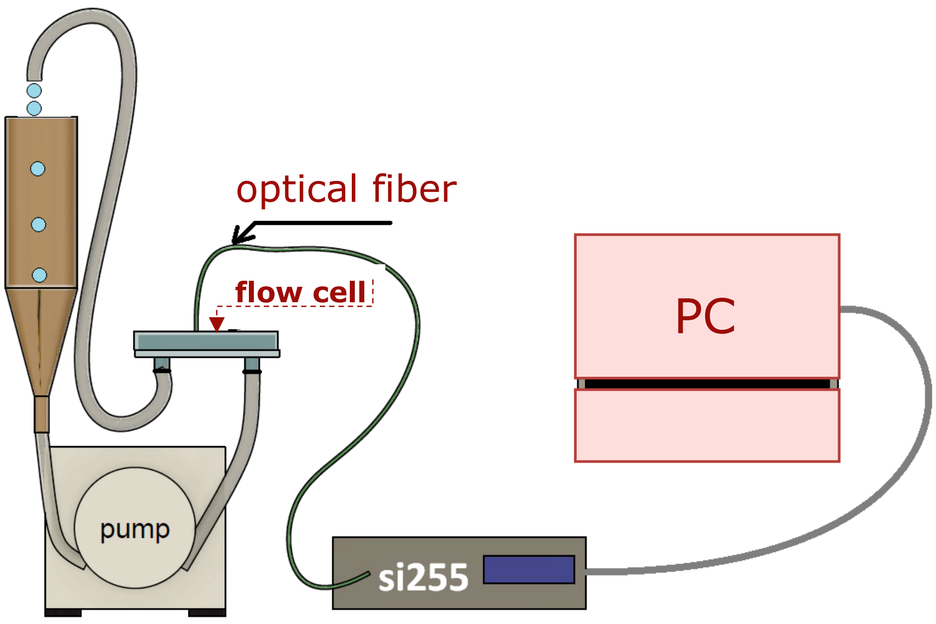

Figure 42. Schematic setup used to measure during a constant flow different water-ethanol concentrations. PC is personal computer.

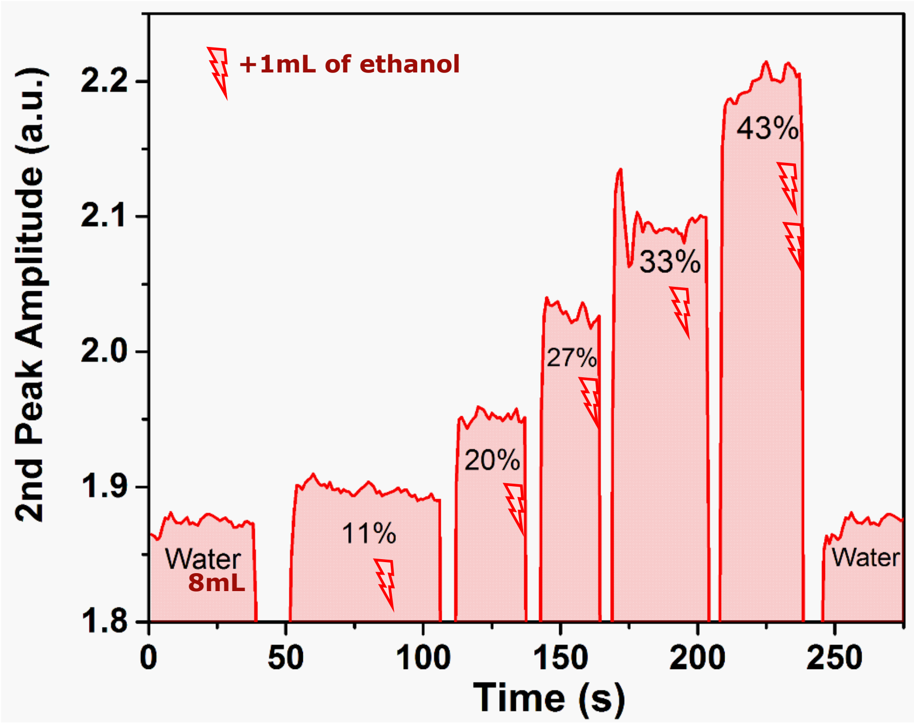

Figure 43. Plot of the Fourier domain 2nd peak amplitude starting with distilled water and adding ethanol to the continuous flow fluidic circuit. Values in black indicate ethanol amount diluted in water.

7.4 Conclusions

A contactless method for monitoring the water content in ethanol solutions has been proposed and demonstrated in this chapter. The method is based on an EFPI. The reflected interference spectra were analyzed in the Fourier domain where the spectra exhibited two well-defined peaks. The changes in the relative position of such peaks as well as on their amplitude provide information of the refractive index changes of ethanol-water samples. Unlike in most sensors proposed so far, in this configuration the optical fiber is not in direct contact with the solution under test which allows to detect real time changes of water content in ethanol. Another novel aspect is that water content is codified in the amplitude of X_2 peak in the Fourier spectra due to absorption in the wavelength span in which the interference patterns were analyzed. The optical absorption of water, in contrast with the refractive index, exhibits low sensitivity to temperature variations, which make the sensor more accurate. It was also demonstrated that it is capable of resolving 0.5% of water content in ethanol.

8 CONCLUDING REMARKS AND FUTURE WORK

8.1 CONCLUSION

A simple extrinsic fiber Fabry-Perot interferometer was implemented with a tapered lead-in fiber and a reflecting surface to achieve contactless thickness and refractive index measurements. First, determining the optimum tapering-down diameter for a fiber tip, both numerically and experimentally. Even though numerical results indicated that the optimum tapering diameter was 51-microns, it was found experimentally that with the 55 μm fiber tip; fringe visibility increased 5 times for the same cavity length compared to a single mode fiber EFPI. Using this tapered lead-in fiber and a high-reflectivity target a displacement sensor was proposed and demonstrated. Where the tapered fiber tip reduces the divergence of the output beam of the optical fiber and couples more efficiently the light reflected from the moving target. These two factors made possible to measure distances from a few micrometers to up to 80 mm.

On the other hand, the increased EFPI's cavity can be used to measure simultaneously, group refractive index and thickness of a sample as well as the position of sample. Differences between measurements here reported and the actual values are less than 0.17% for the refractive index, and thickness measurements and 0.7% for the distance to the sample measurements, this one is higher because it involves the motorized stage positioning error. The simultaneous measurements performed with the PDMS sample led to calculate the dn/dT coefficient. This coefficient presents a slight difference (1.7×10^{-5} RIU) compared with a previous reported value. Otherwise, the calculated value for the coefficient of linear expansion (α) presents a difference of 1.3×10^{-4} compared to the value provided by the manufacturer, and they can be attributed to the measuring method proposed but also to the non-ideal curing and mixing conditions.

Finally, the liquid samples refractive index measurements exhibit a linear behavior with the varying water content. But most important was to demonstrate that the light absorption of the sample can be related to the amplitude of X_2 peak. We expect that this scheme could be used to solve problems in the field of biofuel production process

8.2 SUGGESTIONS FOR FURTHER WORK

The sensing scheme here proposed has shown a broad flexibility for using it to measure different parameters, from distance to refractive indexes of transparent materials. These are some few applications, but is necessary to first review the sensing needs in industrial and medical fields where fiber optic sensors can bring superior performance compared to electronic ones.

Something pending to develop using this measuring setup would be a gas refractometer, with the same principle used for liquid samples.

On the other side, the sensing instruments used such as the sm-125, and si255 from Micron Optics are very expensive for developing solutions for the micro and small manufacturing industries that are scattered all over the Mexican territory. This leads to think about the necessity of creating a novel low cost interrogation system that could work with fiber optic sensors.

Along the sensing setup, the fiber probe can be manufactured with a GRIN lens or even a collimating lens depending on the need. If there is no need of larger cavities, then a single mode fiber could be used.

A OPTICAL FIBER TOOLBOX

The information described in this section has been extracted and summarized from references [45, 104]

A table of applicability based on the results and comparisons between models by tapered optical fiber region is found in [104],pg.106. For tapering an smf-28 fiber to the point where $n_{eff} \geq n_{clad}$ for the fundamental mode (LP_{01} or HE_{11}) the recommended model is the Monérie mode. For standard, commercial, untapered mono-mode fibers the fundamental mode can be obtained with the 2-layer LP, 2-layer HE/EH, and Monérie models.

A.1 The 2-layer model

A.1.1 LP Modes

For the scalar approximation (LP modes) the eigenvalue equation is implemented as the function **eve2LS.m**, and was taken from [105],pg.131, eq. (3.3-26)

$$ha\frac{J_{l+1}(ha)}{J_l(ha)} = qa\frac{K_{l+1}(qa)}{K_l(qa)}$$

where *a* is the fiber's core radius, $h = \sqrt{n_1^2 k_0^2 - \beta^2}$, $q = \sqrt{\beta^2 - n_2^2 k_0^2}$.

A.1.1.1 Mode field

The respective field equations are found in [105],pg.130,131, eq.(3.3-24), (3.3-25) and implemented in **modeFieldLP.m**

In the core, for r<a:

$$E_x = AJ_l(hr)e^{il\phi}\exp[i(\omega t - \beta z)]$$

$$E_y = 0$$

$$E_z = i\frac{h}{\beta}\frac{A}{2}[J_{l+1}(hr)e^{i(l+1)\phi} - J_{l-1}(\mathrm{hr})\mathrm{e}^{\mathrm{i(l-1)}\phi}\exp[i(\omega t - \beta z)]$$

$$H_x \cong 0$$

$$H_y = \frac{\beta}{\omega\mu}AJ_l(hr)e^{il\phi}\exp[i(\omega t - \beta z)]$$

$$H_z = \frac{h}{\omega\mu}\frac{A}{2}[J_{l+1}(hr)e^{i(l+1)\phi} + J_{l-1}(hr)e^{i(l-1)\phi}]\exp[i(\omega t - \beta z)]$$

In the cladding, for r>a:

$$E_x = BK_l(qr)e^{il\phi}\exp[i(\omega t-\beta z)]$$

$$E_y = 0$$

$$E_z = i\frac{q}{\beta}\frac{B}{2}[K_{l+1}(qr)e^{i(l+1)\phi} - K_{l-1}(\mathrm{qr})\mathrm{e}^{\mathrm{i(l-1)}\phi}]\exp[i(\omega t-\beta z)]$$

$$H_x \cong 0$$

$$H_y = \frac{\beta}{\omega\mu}BK_l(qr)e^{il\phi}\exp[i(\omega t-\beta z)]$$

$$H_z = \frac{q}{\omega\mu}\frac{B}{2}[\,K_{l+1}(qr)e^{i(l+1)\phi} - K_{l-1}(\mathrm{qr})\mathrm{e}^{\mathrm{i(l-1)}\phi}\exp[i(\omega t-\beta z)]$$

A.1.2 Exact solutions

For the vectorial solution of HE/EH modes the eigenvalue equation was taken from [105], pg.804, eq.(B-11) , **eve2LS.m**, $n_{eff}<<n_{clad}$

$$\left(\frac{J_l'(ha)}{haJ_l(ha)}+\frac{K_l'(qa)}{qaK_l(qa)}\right)\left(\frac{n_1^2J_l'(ha)}{haJ_l(ha)}+\frac{n_2^2K_l'(qa)}{qaK_l(qa)}\right) = l^2\left[\left(\frac{1}{qa}\right)^2+\left(\frac{1}{ha}\right)^2\right]^2\left(\frac{\beta}{k_0}\right)^2$$

A.1.2.1 Mode field

The mode field equations for this EH/HE solutions where obtained from [39],pg.250, in file **modefield.m**

For the core:

$$e_r = -\frac{a_1J_{v-1}(UR)+a_2J_{v+1}(UR)}{J_v(U)}f_v(\phi)$$

$$e_\phi = -\frac{a_1J_{v-1}(UR)-a_2J_{v+1}(UR)}{J_v(U)}g_v(\phi)$$

$$e_z = \frac{-iU}{\rho\beta}\frac{J_v(UR)}{J_v(U)}f_v(\phi)$$

$$h_r = \left(\frac{\epsilon_0}{\mu_0}\right)^{\frac{1}{2}}\frac{kn_{co}^2}{\beta}\frac{a_3J_{v-1}(UR)-a_4\,J_{v+1}(UR)}{J_v(U)}g_v(\phi)$$

$$h_\phi = -\left(\frac{\epsilon_0}{\mu_0}\right)^{\frac{1}{2}}\frac{kn_{co}^2}{\beta}\frac{a_3J_{v-1}(UR)-a_4\,J_{v+1}(UR)}{J_v(U)}f_v(\phi)$$

$$h_z = -i\left(\frac{\epsilon_0}{\mu_0}\right)^{\frac{1}{2}} \frac{UF_2}{\kappa\rho} \frac{J_v(UR)}{J_v(U)} g_v(\phi)$$

For the cladding:

$$e_r = -\frac{U}{W} \frac{a_1 K_{v-1}(WR) - a_2 K_{v+1}(WR)}{K_v(W)} f_v(\phi)$$

$$e_\phi = -\frac{U}{W} \frac{a_1 K_{v-1}(WR) + a_2 K_{v+1}(WR)}{K_v(W)} g_v(\phi)$$

$$e_z = \frac{-iU}{\rho\beta} \frac{K_v(WR)}{K_v(W)} f_v(\phi)$$

$$h_r = \left(\frac{\epsilon_0}{\mu_0}\right)^{\frac{1}{2}} \frac{kn_{co}^2}{\beta} \frac{U}{W} \frac{a_5 K_{v-1}(WR) + a_6\, K_{v+1}(WR)}{K_v(W)} g_v(\phi)$$

$$h_\phi = -\left(\frac{\epsilon_0}{\mu_0}\right)^{\frac{1}{2}} \frac{kn_{co}^2}{\beta} \frac{U}{W} \frac{a_5 K_{v-1}(WR) - a_6\, K_{v+1}(WR)}{K_v(W)} f_v(\phi)$$

$$h_z = -i\left(\frac{\epsilon_0}{\mu_0}\right)^{\frac{1}{2}} \frac{UF_2}{\kappa\rho} \frac{K_v(WR)}{K_v(W)} g_v(\phi)$$

where $f_v = \begin{cases}\cos(\nu\phi) \\ \sin(\nu\phi)\end{cases}$; $g_v = \begin{cases}-\sin(\nu\phi) \\ \cos(\nu\phi)\end{cases}$; $\begin{cases} even\ modes \\ odd\ modes\end{cases}$

A.2 The 3-layer model

A.2.1 LP Modes

This are valid for large diameter fibers where light does not leave the fiber. The eigenvalue equation is found in [45], eq.(4) for core guided modes where $n_{clad} \leq n_{eff} < n_{core}$. The corresponding function is **eve3LS.m**

$$\frac{[\hat{J}_m(u) - \hat{K}_m(v'c)][\hat{K}_m(v) - \hat{I}_m(v')]}{[\hat{J}_m(u) + \hat{I}_m(v'c)][\hat{K}_m(v) - \hat{K}_m(v')]} = \frac{I_{m+1}(v'c)K_{m+1}(v')}{I_{m+1}(v')K_{m+1}(v'c)}$$

A.2.1.1 Mode field

This equations can be found in [45], as eq.(1), (2)

for a≤r≤b and $n_{clad} \leq n_{eff} < n_{core}$:

$$\psi = A_1 J_m\left(u'\frac{r}{b}\right) + A_2 Y_m\left(u'\frac{r}{b}\right)$$

where J_m, Y_m are the modified Bessel functions.

A.2.2 Exact solutions

This is the solution that takes more computation time due to the calculations needed. The eigenvalue equations are found in [43], as eqs.(5)-(7). The function file is **eve3LS.m**

$$\zeta_0 = \zeta'_0$$

$$\zeta_0 = \frac{1}{\sigma_2}\frac{u_2\left(JK + \frac{\sigma_1\sigma_2 u_{21}u_{32}}{n_2^2 a_1 a_2}\right)p_l(a_2) - Kq_l(a_2) + Jr_l(a_2) - \frac{1}{u_2}s_l(a_2)}{-u_2\left(\frac{u_{32}}{n_2^2 a_2}J - \frac{u_{21}}{n_1^2 a_1}K\right)p_l(a_2) + \frac{u_{32}}{n_1^2 a_2}q_l(a_2) + \frac{u_{21}}{n_1^2 a_1}r_l(a_2)}$$

$$\zeta'_0 = \sigma_1 \frac{u_2\left(\frac{u_{32}}{a_2}J - \frac{n_3^2 u_{21}}{n_2^2 a_1}K\right)p_l(a_2) + \frac{u_{32}}{a_2}q_l(a_2) + \frac{u_{21}}{a_1}r_l(a_2)}{u_2\left(\frac{n_3^2}{n_2^2 a_2}JK + \frac{\sigma_1\sigma_2 u_{21}u_{32}}{n_1^2 a_1 a_2}\right)p_l(a_2) - \frac{n_3^2}{n_1^2}Kq_l(a_2) + Jr_l(a_2) - \frac{n_2^2}{n_1^2 u_2}s_l(a_2)}$$

the variable definitions for this equations are given in eqs. (8)-(19), [43].

A.2.2.1 Mode field

These equations where taken from [43,44], and the corresponding file is called: **modeFieldErogan.m**

In the core:

$$E_r = iE_{1v}\frac{u_1}{2}\left\{J_2(u_1 r) + J_0(u_1 r) - \frac{\sigma_2\zeta_0}{n_1^2}[J_2(u_1 r) - J_0(u_1 r)]\right\}\exp(i\phi)\exp[i(\beta z - \omega t)]$$

$$E_\phi = iE_{1v}\frac{u_1}{2}\left\{J_2(u_1 r) - J_0(u_1 r) - \frac{\sigma_2\zeta_0}{n_1^2}X[J_2(u_1 r) - J_0(u_1 r)]\right\}\exp(i\phi)\exp[i(\beta z - \omega t)]$$

$$E_z = E_{1v}\frac{u_1^2\sigma_2\zeta_0}{n_1^2\beta}J_1(u_1 r)\exp(i\phi)\exp[i(\beta z - \omega t)]$$

$$H_r = E_{1v}\frac{u_1}{2}\{i\sigma_1\,[J_2(u_1 r) - J_0(u_1 r)] - i\zeta_0[J_2(u_1 r) + J_0(u_1 r)]\}\exp(i\phi)\exp[i(\beta z - \omega t)]$$

$$H_\phi = -iE_{1v}\frac{u_1}{2}\{i\sigma_1\,[J_2(u_1 r) + J_0(u_1 r)] + i\zeta_0[J_2(u_1 r) - J_0(u_1 r)]\}\exp(i\phi)\exp[i(\beta z - \omega t)]$$

$$H_z = -iE_{1v}\frac{u_1^2 i\sigma_1}{\beta}J_1(u_1 r)\exp(i\phi)\exp[i(\beta z - \omega t)]$$

B LONG-RANGE TAPERED EFPI SIMULATION

The diagram of the tapered EFPI is shown in Fig.26. Zhang et al.[33] proposed this model for their graded index beam collimator, and because the tapered fiber tip have a similar effect on the beam this was a good starting point. Parting from the two beam interference equation, eq. (1). The two unknown variables are I_R and I_S, then the visibility could be solved (eq. (2)), and this is calculated for different lengths (L).

From eqs.(1) and (2) this is obtained[Zhang]:

$$V = \frac{2\sqrt{P_1 P_2}}{P_1 + P_2}$$

Then, defining a variable k as:

$$k = \frac{P_2}{P_1}$$

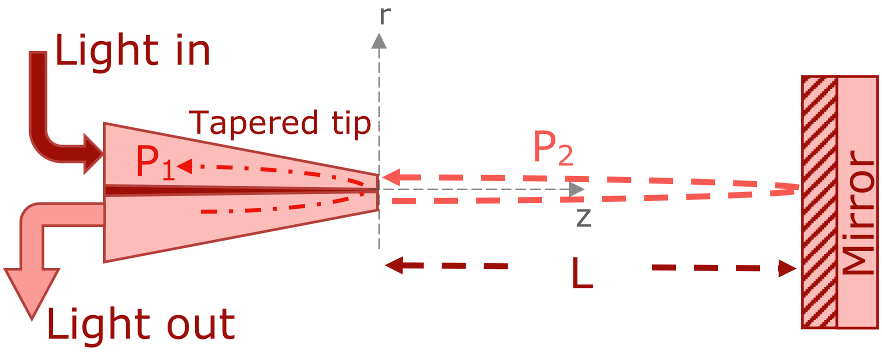

Figure 44. Schematic diagram of the tapered EFPI for long-range measurements.

Substituting k in V, the visibility can be determined as

$$V = \frac{2\sqrt{k}}{1+k}$$

With low finesse EFPIs I_s light amount tends to be smaller than I_R, in this case it was shown that for short lengths the opposite happens.

Using the Gaussian beam approximation, considering the beam at the endface of the fiber (out) with Gaussian intensity profile[18]. Then the radial intensity profile is approximated as [106],

$$I\ (r,z) = I_0(z)e^{\left(\frac{-2r^2}{w(z)^2}\right)}$$

where *r* is the radial distance from de center point of the fiber endface, I_0 the input light intensity, *w(z)* the beam radius at *z* position.
While the beam propagates through the cavity the beam diverges and its radius grows according to w(z)

$$w(z) = w_0\sqrt{1+\left(\frac{Z}{Z_R}\right)^2}$$

where w(z) is the beam radius and the Rayleigh length (ZR) defined as

$$Z_R = \frac{\pi {w_0}^2}{\lambda}$$

where w_0 is the beam radius at z=0 (endface) corresponding to the half of the MFD of the tapered tip.

The first reflection, P_1 can be calculated as follows

$$P_1 = 2\pi R_1 \int_0^a \frac{2P_0}{\pi {w_0}^2} e^{\left(\frac{-2r^2}{{w_0}^2}\right)} rdr$$

where $R_1 = \left(\frac{n_{fiber}-n_{air}}{n_{fiber}+n_{air}}\right)$, is the reflection coefficient of the fiber endface. The light transmitted to the EFPI's air cavity propagates a distance L and then is reflected backwards travelling the same distance to reach again the fiber's endface were it will be partially coupled back-in. This second reflection can be calculated with

$$P_2 = 2\pi e^{\pi} R_2 (1-R_1)^2 \int_0^a \frac{2P_0}{\pi {w_{2L}}^2} e^{\left(\frac{-2r^2}{{w_{2L}}^2}\right)} rdr$$

where R_2 is the reflection coefficient of the thin firm mirror, w_{2L} is the mode field radius at z=2L solved with

$$w_{2L} = w_0 \sqrt{1 + \left(\frac{2L}{Z_R}\right)^2}$$

finally, *V(L)* can be solved by calculating the ratio *k* with the following values:

Table 5. Input values used for the simulations of the tapered EFPI's visibility vs. length.

n_{fiber}	1.4512(n_{eff})
n_{air}	1
R_2	0.99
λ	1.55
MFD_{taper}	14.8
a	1.98
w_0	7.4
P_0	100

This values are the ones that produced the curves shown in Figs.25 and 26. It is worth noting that the first value MFD_{taper}=13.4μm was the one obtained numerically in sec. 3.2, but after several iterations the best fit for the experimental measurements was obtained using 14.8, as shown in Table 5.

C NON-CONTACTLESS MEASUREMENTS

Thickness measurements of a protective transparent coating of two automotive “front fog lamp shields” pieces (shown in Fig.44) were made. Following the method described for glass samples (chapter 6), but for these measurements a single-mode pigtail FC connector was used as sensing tip in contact with the sample at 22 different sampling positions in order to obtain a coating thickness mean value (shown in Fig.45a)

Figure 45. Picture of the both samples used to measure its coating thickness.

C.1 Measurement procedure

By placing an optic fiber on the point of interest(Fig.3a), the light reflected can be analyzed(Fig.3b), since the optical spectrum bandwidth is 160nm it allows to measure small gaps or thin films.

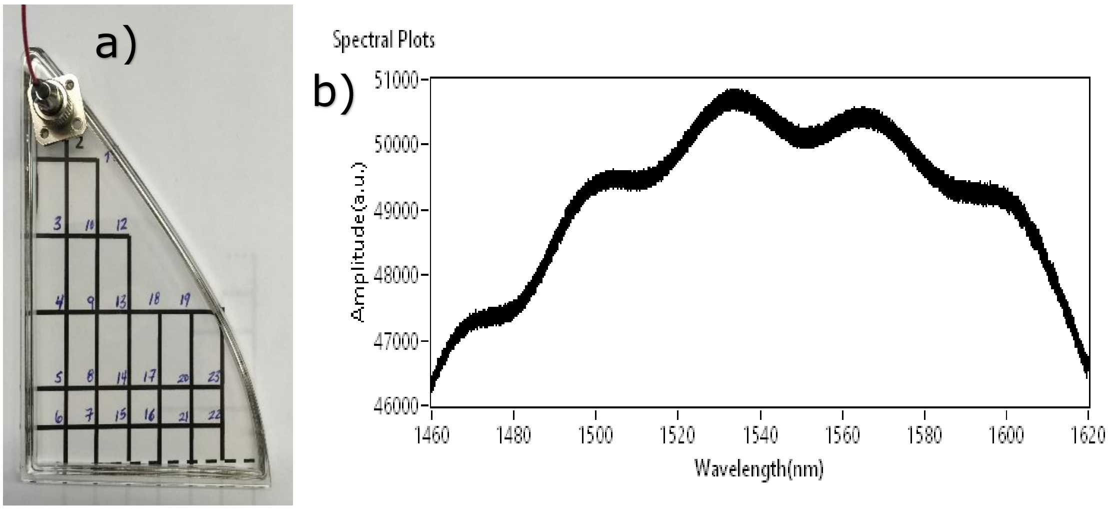

Fig. 46. Optical interference spectrum that shows modulation corresponding to the layer optical thickness.

A customized program analyzes the optical spectrum acquired in real time and shows the Fourier domain plot and identifies the peak due to the layer's optical thickness of interest. (Fig.46)

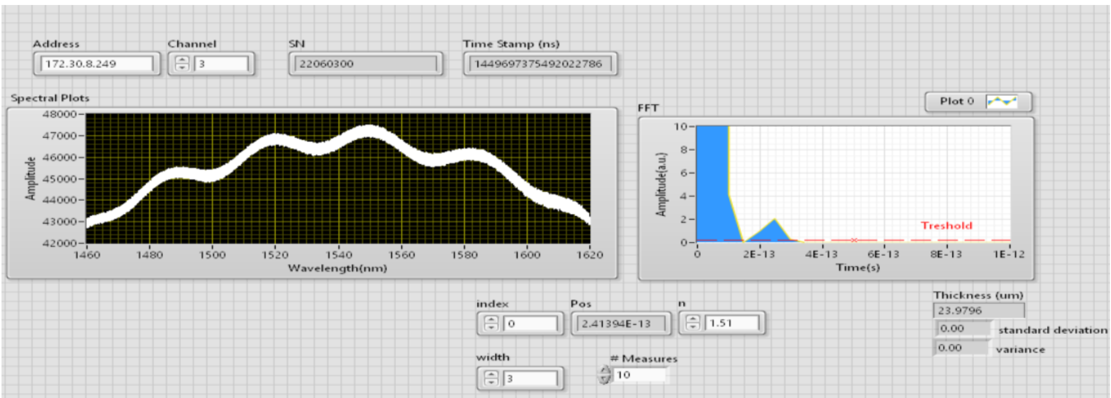

Figure 47. Screen of the program developed to measure the protective coating of these plastic samples.

C.2 Results

Supposing a value of *n=1.51* for the refractive index of the layer of interest we obtained the physical thickness in each measured point.

The optic fiber was placed on every point to obtain one of the columns, and this was repeated two more times, the measurements are shown on the table below.

Automatizing the measurements and designing a stand for sample placement could minimize errors due to fiber scanning over every point.

Table 6. Results for 3 thickness measurements for each point of each sample.

Sample : 561.941.777.C 27/11/2015

Point #	M1	M2	M3	Mean Thickness (um)	Std. Dev. ±(um)
1	18.918	19.717	19.080	19.24	0.42
2	19.840	19.654	19.476	19.66	0.18
3	23.786	23.541	24.511	23.95	0.50
4	22.459	23.890	22.490	22.95	0.82
5	20.799	23.040	23.334	22.39	1.39
6	19.591	19.426	19.154	19.39	0.22
7	19.878	19.948	19.925	19.92	0.04
8	23.922	23.640	21.370	22.98	1.40
9	24.500	25.073	24.860	24.81	0.29
10	24.737	24.179	24.434	24.45	0.28
11	20.006	20.863	19.999	20.29	0.50
12	24.041	24.397	24.619	24.35	0.29
13	24.019	25.756	24.331	24.70	0.93
14	21.607	21.958	23.413	22.33	0.96
15	19.916	20.193	19.900	20.00	0.16
16	19.518	18.843	19.289	19.22	0.34
17	20.185	20.058	20.410	20.22	0.18
18	25.234	24.386	23.832	24.48	0.71
19	23.883	24.349	24.283	24.17	0.25
20	20.607	20.485	20.112	20.40	0.26
21	19.034	18.236	18.120	18.46	0.50
22	18.283	17.151	17.854	17.76	0.57
23	19.739	19.781	20.171	19.90	0.24

Sample : 561.941.778.C 25/11/2015

Point #	M1	M2	M3	Mean Thickness (um)	Std. Dev. ±(um)
1	19.200	19.491	18.839	19.18	0.33
2	20.224	19.965	19.815	20.00	0.21
3	20.749	21.159	21.403	21.10	0.33
4	23.245	23.840	23.788	23.62	0.33
5	22.412	21.826	22.836	22.36	0.51
6	21.913	22.297	23.158	22.46	0.64
7	23.896	23.089	23.340	23.44	0.41
8	23.833	23.809	24.343	23.99	0.30
9	24.208	23.856	23.979	24.01	0.18
10	24.529	23.445	24.611	24.20	0.65
11	20.409	20.254	20.386	20.35	0.08
12	24.484	23.765	24.585	24.28	0.45
13	24.142	24.047	24.729	24.31	0.37
14	23.928	24.091	24.141	24.05	0.11
15	23.297	23.756	23.208	23.42	0.29
16	23.209	22.025	22.981	22.74	0.63
17	20.056	23.548	23.762	22.46	2.08
18	24.818	24.834	24.923	24.86	0.06
19	24.461	23.787	23.578	23.94	0.46
20	20.150	20.545	20.112	20.27	0.24
21	20.359	20.581	20.524	20.49	0.12
22	19.859	20.214	20.372	20.15	0.26
23	21.050	20.109	21.848	21.00	0.87

BIBLIOGRAPHY

1. Miya, T., et al. *Ultimate low-loss single-mode fibre at 1.55 µm*. Electronics Letters, 1979. **15**, 106-108.
2. Bucaro, J.A., H.D. Dardy, and E.F. Carome, *Fiber-optic hydrophone.* The Journal of the Acoustical Society of America, 1977. **62**(5): p. 1302-1304.
3. Culshaw, B., D.E.N. Davies, and S.A. Kingsley, *Acoustic sensitivity of optical-fibre waveguides.* Electronics Letters, 1977. **13**(25): p. 760-761.
4. Hocker, G.B., *Fiber-optic sensing of pressure and temperature.* Applied Optics, 1979. **18**(9): p. 1445-1448.
5. Rugar, D., H.J. Mamin, and P. Guethner, *Improved fiber-optic interferometer for atomic force microscopy.* Applied Physics Letters, 1989. **55**(25): p. 2588-2590.
6. Thylen, L.H., P.O. Andersson, and S.A.R. Persson, *Fibre-optic interferometer*. 1988, Google Patents.
7. *Opsens*. [cited 2016 May 2]; Available from: https://opsens.com/.
8. *Presens*. [cited 2016 May 2]; Available from: www.presens.de.
9. *Fiso Sensors*. [cited 2016 May 2]; Available from: www.fiso.com.
10. *Micron Optics*. [cited 2016 June 28]; Available from: http://www.micronoptics.com/product/optical-sensing-instrument-si255/.
11. Méndez, A. *Fiber Bragg grating sensors: a market overview*. 2007.
12. Ran, Z.L., et al., *Laser-micromachined Fabry-Perot optical fiber tip sensor for high-resolution temperature-independent measurement of refractive index.* Optics Express, 2008. **16**(3): p. 2252-2263.

13. Udd, E. and W.B. Spillman, *Fiber Optic Sensors: An Introduction for Engineers and Scientists*. 2011: Wiley.
14. Zhao, Z., et al., *Modulation functions of the reflective optical fiber sensor for specular and diffuse reflection.* Optical Engineering, 1994. **33**(9): p. 2986-2991.
15. Carpignano, F., et al., *Refractive Index Sensing in Rectangular Glass Micro-Capillaries by Spectral Reflectivity Measurements.* Ieee Journal of Selected Topics in Quantum Electronics, 2016. **22**(3).
16. Caucheteur, C., T. Guo, and J. Albert, *Review of plasmonic fiber optic biochemical sensors: improving the limit of detection.* Analytical and Bioanalytical Chemistry, 2015. **407**(14): p. 3883-3897.
17. Beard, P. and T. Mills, *Extrinsic optical-fiber ultrasound sensor using a thin polymer film as a low-finesse Fabry–Perot interferometer.* Applied optics, 1996. **35**(4): p. 663-675.
18. Arya, V., et al., *Exact Analysis of the Extrinsic Fabry-Perot Interferometric Optical Fiber Sensor Using Kirchhoff's Diffraction Formalism.* Optical Fiber Technology, 1995. **1**(4): p. 380-384.
19. Gangopadhyay, T.K., et al., *Modeling and analysis of an extrinsic Fabry–Perot interferometer cavity.* Applied Optics, 2005. **44**(16): p. 3192-3196.
20. Santos, J.L., A.P. Leite, and D.A. Jackson, *Optical fiber sensing with a low-finesse Fabry–Perot cavity.* Applied Optics, 1992. **31**(34): p. 7361-7366.
21. Donlagic, D.M., SI), Pevec, Simon (Podcetrtek, SI), *FIBER-OPTIC MEASUREMENT SYSTEM AND METHODS BASED ON ULTRA-SHORT CAVITY LENGTH FABRY-PEROT SENSORS AND LOW RESOLUTION SPECTRUM ANALYSIS*. 2016, UNIVERSITY OF MARIBOR: United States.
22. Han, M., *Theoretical and Experimental Study of Low-Finesse Extrinsic*

Fabry-Perot Interferometric Fiber Optic Sensors. 2006, Virginia Polytechnic Institute and State University (Virginia Tech).
23. Chen, J.-H., et al., *Extrinsic fiber-optic Fabry–Perot interferometer sensor for refractive index measurement of optical glass.* Applied Optics, 2010. **49**(29): p. 5592-5596.
24. Hai, X., et al., *Single-crystal sapphire fiber-based strain sensor for high-temperature applications.* Journal of Lightwave Technology, 2003. **21**(10): p. 2276-2283.
25. Egorov, S.A., et al. *Advanced signal processing method for interferometric fiber optic sensors with straightforward spectral detection*. 1998.
26. Born, M. and E. Wolf, *Principles of optics: electromagnetic theory of propagation, interference and diffraction of light*. 2000: CUP Archive.

27. Yin, S. and F.T.S. Yu, *Fiber Optic Sensors*. 2002: CRC Press.
28. A/S, I.P. [cited 2016 June 29]; Available from: http://ibsen.com/products/interrogation-monitors.
29. Ushakov, N., L. Liokumovich, and A. Medvedev. *EFPI signal processing method providing picometer-level resolution in cavity length measurement*. in *SPIE Optical Metrology 2013*. 2013. International Society for Optics and Photonics.
30. Shi-Kay, Y. and C. Asawa, *Fiber Optical Intensity Sensors.* IEEE Journal on Selected Areas in Communications, 1983. **1**(3): p. 562-575.
31. Yu, B., A. Wang, and G.R. Pickrell, *Analysis of Fiber Fabry-Pérot Interferometric Sensors Using Low-Coherence Light Sources.* Journal of Lightwave Technology, 2006. **24**(4): p. 1758.
32. Thurner, K., P.F. Braun, and K. Karrai, *Fabry-Perot interferometry for long range displacement sensing.* Review of Scientific Instruments, 2013. **84**(9): p. 095005.
33. Zhang, Y., et al., *Fringe Visibility Enhanced Extrinsic Fabry–Perot Interferometer Using a Graded Index Fiber Collimator.* IEEE Photonics Journal, 2010. **2**(3): p. 469-481.
34. Chanclou, P., et al., *Expanded single-mode fiber using graded index multimode fiber.* Optical Engineering, 2004. **43**(7): p. 1634-1642.
35. *Corning*. [cited 2016 June 30]; Available from: https://www.corning.com/worldwide/en/products/communication-networks/products/fiber.html.
36. Murphy, K.A., et al., *Quadrature phase-shifted, extrinsic Fabry–Perot optical fiber sensors.* Optics Letters, 1991. **16**(4): p. 273-275.
37. Jedrzejewski, K.P., et al., *Tapered-Beam Expander for Single-Mode Optical-Fiber Gap Devices.* Electronics Letters, 1986. **22**(2): p. 105-106.
38. Snyder, A.W. and J. Love, *Optical Waveguide Theory*. 1983: Springer.
39. Wiedemann, U., et al., *Measurement of submicrometre diameters of tapered optical fibres using harmonic generation.* Optics Express, 2010. **18**(8): p. 7693-7704.
40. Belanov, A.S., et al., *Propagation of normal modes in multilayer optical waveguides I. Component fields and dispersion characteristics.* Soviet Journal of Quantum Electronics, 1976. **6**(1): p. 43.
41. Erdogan, T., *Cladding-mode resonances in short- and long-period fiber grating filters.* Journal of the Optical Society of America A, 1997. **14**(8): p. 1760-1773.
42. Erdogan, T., *Cladding-mode resonances in short- and long-period fiber grating filters: errata.* Journal of the Optical Society of America A, 2000. **17**(11): p. 2113-2113.

43. Monerie, M., *Propagation in doubly clad single-mode fibers.* IEEE Journal of Quantum Electronics, 1982. **18**(4): p. 535-542.
44. Zhang, Z.-j. and W.-k. Shi, *Eigenvalue and field equations of three-layered uniaxial fibers and their applications to the characteristics of long-period fiber gratings with applied axial strain.* Journal of the Optical Society of America A, 2005. **22**(11): p. 2516-2526.
45. K. Karapetyan, e.a. *Optical fibre toolbox for Matlab, version 2.1*. 2010 [cited 2016 July 6]; Available from: https://www.mathworks.com/matlabcentral/fileexchange/27819-optical-fibre-toolbox/content/demo/html/tutorial3ls.html.
46. Love, J.D., et al., *Tapered single-mode fibres and devices. I. Adiabaticity criteria.* IEE Proceedings J - Optoelectronics, 1991. **138**(5): p. 343-354.
47. Love, J.D., *Spot Size, Adiabaticity and Diffraction in Tapered Fibers.* Electronics Letters, 1987. **23**(19): p. 993-994.
48. Alder, T., et al., *High-efficiency fiber-to-chip coupling using low-loss tapered single-mode fiber.* IEEE Photonics Technology Letters, 2000. **12**(8): p. 1016-1018.
49. Weidman, D.L., *Multi-neckdown fiber optic coupler*. 1997, Google Patents.
50. *Vytran*. [cited 2016 August, 15]; Available from: http://www.vytran.com/product/gpx-3000_series.
51. *Centro de Investigaciones en Óptica, A.C.* 2016; Available from: http://www.cio.mx/tecnologia_inovacion.php.
52. Moreno-Hernandez, C.J., et al., *Long-range interferometric displacement sensing with tapered optical fiber tips.* IEEE Photonics Technology Letters, 2015. **27**(4): p. 379-382.
53. Berkovic, G. and E. Shafir, *Optical methods for distance and displacement measurements.* Advances in Optics and Photonics, 2012. **4**(4): p. 441-471.
54. Yang, H.Z., et al., *A review of recent developed and applications of plastic fiber optic displacement sensors.* Measurement, 2014. **48**: p. 333-345.
55. Bravo, M., et al., *Micro-Displacement Sensor Combined With a Fiber Ring Interrogated by an Optical Time-Domain Reflectometer.* IEEE Sensors Journal, 2014. **3**(14): p. 793-796.
56. Baker, C. and X. Bao, *Displacement sensor based on Kerr induced phase-modulation of orthogonally polarized sinusoidal optical signals.* Optics express, 2014. **22**(8): p. 9095-9100.
57. Qi, T., et al., *Cladding-mode backward-recoupling-based displacement sensor incorporating fiber up taper and Bragg grating.* IEEE Photonics Journal, 2013. **5**(4): p. 7100608-7100608.
58. Jasim, A., et al., *A new compact micro-ball lens structure at the cleaved tip of microfiber coupler for displacement sensing.* Sensors and Actuators A: Physical, 2013. **189**: p. 177-181.

59. Ji, C., et al., *Multiplex and simultaneous measurement of displacement and temperature using tapered fiber and fiber Bragg grating.* Review of Scientific Instruments, 2012. **83**(5): p. 053109.
60. Perret, L., et al., *Fiber optics sensor for sub-nanometric displacement and wide bandwidth systems.* Sensors and Actuators A: Physical, 2011. **165**(2): p. 189-193.
61. Azak, N., et al., *Nanomechanical displacement detection using fiber-optic interferometry.* Applied Physics Letters, 2007. **91**(9): p. 093112.
62. Rao, Y.-J., *Recent progress in fiber-optic extrinsic Fabry–Perot interferometric sensors.* Optical Fiber Technology, 2006. **12**(3): p. 227-237.
63. Zhao, Y., et al., *A novel fiber-optic sensor used for small internal curved surface measurement.* Sensors and Actuators A: Physical, 2000. **86**(3): p. 211-215.
64. Wang, T., S. Zheng, and Z. Yang, *A high precision displacement sensor using a low-finesse fiber-optic Fabry-Pérot interferometer.* Sensors and Actuators A: Physical, 1998. **69**(2): p. 134-138.
65. Cook, R.O. and C.W. Hamm, *Fiber optic lever displacement transducer.* Applied Optics, 1979. **18**(19): p. 3230-3241.
66. Liu, G., M. Han, and W. Hou, *High-resolution and fast-response fiber-optic temperature sensor using silicon Fabry-Pérot cavity.* Optics express, 2015. **23**(6): p. 7237-7247.
67. Wang, R. and X. Qiao, *Gas Refractometer Based on Optical Fiber Extrinsic Fabry—Perot Interferometer With Open Cavity.* IEEE Photonics Technology Letters, 2015. **27**(3): p. 245-248.
68. Wang, W. and F. Li, *Large-range liquid level sensor based on an optical fibre extrinsic Fabry–Perot interferometer.* Optics and Lasers in Engineering, 2014. **52**: p. 201-205.
69. Wen, X., et al., *Ultrasensitive temperature fiber sensor based on Fabry-Pérot interferometer assisted with iron V-groove.* Optics express, 2015. **23**(9): p. 11526-11536.
70. Zhang, G., M. Yang, and Y. Wang, *Optical fiber-tip Fabry–Perot interferometer for hydrogen sensing.* Optics Communications, 2014. **329**: p. 34-37.
71. Pevec, S. and D. Donlagic, *High resolution, all-fiber, micro-machined sensor for simultaneous measurement of refractive index and temperature.* Optics express, 2014. **22**(13): p. 16241-16253.
72. Wang, R. and X. Qiao, *Hybrid optical fiber Fabry–Perot interferometer for simultaneous measurement of gas refractive index and temperature.* Applied optics, 2014. **53**(32): p. 7724-7728.

73. Wang, W., et al., *Optical pressure/acoustic sensor with precise Fabry-Perot cavity length control using angle polished fiber.* Optics express, 2009. **17**(19): p. 16613-16618.
74. Sorin, W. and D. Gray, *Simultaneous thickness and group index measurement using optical low-coherence reflectometry.* Ieee Photonics Technology Letters, 1992. **4**(1): p. 105-107.
75. Tearney, G., et al., *Determination of the refractive index of highly scattering human tissue by optical coherence tomography.* Optics letters, 1995. **20**(21): p. 2258-2260.
76. Fukano, T. and I. Yamaguchi, *Simultaneous measurement of thicknesses and refractive indices of multiple layers by a low-coherence confocal interference microscope.* Optics letters, 1996. **21**(23): p. 1942-1944.
77. Chinn, S., E. Swanson, and J. Fujimoto, *Optical coherence tomography using a frequency-tunable optical source.* Optics letters, 1997. **22**(5): p. 340-342.
78. Cheng, H.-C. and Y.-C. Liu, *Simultaneous measurement of group refractive index and thickness of optical samples using optical coherence tomography.* Applied optics, 2010. **49**(5): p. 790-797.
79. Fukano, T. and I. Yamaguchi, *Separation of measurement of the refractive index and the geometrical thickness by use of a wavelength-scanning interferometer with a confocal microscope.* Applied optics, 1999. **38**(19): p. 4065-4073.
80. Ilev, I.K., et al., *Dual-confocal fiber-optic method for absolute measurement of refractive index and thickness of optically transparent media.* Optics letters, 2002. **27**(19): p. 1693-1695.
81. Na, J., et al., *Self-referenced spectral interferometry for simultaneous measurements of thickness and refractive index.* Applied optics, 2009. **48**(13): p. 2461-2467.
82. Wang, X., et al., *Simultaneous refractive index and thickness measurements of bio tissue by optical coherence tomography.* Journal of biomedical optics, 2002. **7**(4): p. 628-632.
83. Kim, S., et al., *Simultaneous measurement of refractive index and thickness by combining low-coherence interferometry and confocal optics.* Optics express, 2008. **16**(8): p. 5516-5526.
84. Zilio, S., *Simultaneous thickness and group index measurement with a single arm low-coherence interferometer.* Optics express, 2014. **22**(22): p. 27392-27397.
85. Waxler, R., et al., *Optical and mechanical properties of some neodymium-doped laser glasses.* JOURNAL OF RESEARCH OF THE NATIONAL BUREAU OF STANDARDS SECTION A-PHYSICS AND CHEMISTRY, 1971(3): p. 163-+.
86. Markos, C., K. Vlachos, and G. Kakarantzas, *Bending loss and thermo-optic effect of a hybrid PDMS/silica photonic crystal fiber.* Optics express, 2010. **18**(23): p. 24344-24351.

87. Girei, S., et al., *Absorbance response of graphene oxide coated on tapered multimode optical fiber towards liquid ethanol.* Journal of the European Optical Society-Rapid publications, 2015. **10**.
88. Possetti, G., et al., *Application of a long-period fibre grating-based transducer in the fuel industry.* Measurement Science and Technology, 2009. **20**(3): p. 034012.
89. Bueno, L. and T.R. Paixao, *A copper interdigitated electrode and chemometrical tools used for the discrimination of the adulteration of ethanol fuel with water.* Talanta, 2011. **87**: p. 210-215.
90. Xiong, F. and D. Sisler, *Determination of low-level water content in ethanol by fiber-optic evanescent absorption sensor.* Optics Communications, 2010. **283**(7): p. 1326-1330.
91. Shabaneh, A., et al., *Dynamic response of tapered optical multimode fiber coated with carbon nanotubes for ethanol sensing application.* Sensors, 2015. **15**(5): p. 10452-10464.
92. Raikar, U., et al., *Etched fiber Bragg grating as ethanol solution concentration sensor.* Optoelectronics and Advanced Material, 2007. **1**: p. 149-151.
93. Xiong, F., et al., *Fiber-optic sensor based on evanescent wave absorbance around 2.7 μm for determining water content in polar organic solvents.* Applied Physics B, 2014. **115**(1): p. 129-135.
94. Beauchaine, J. and J. Briggs, *Measurement of water in ethanol using encoded photometric NIR spectroscopy.* Spectroscopy, 2007. **22**(6): p. 40-+.
95. Mariammal, R., et al., *On the enhancement of ethanol sensing by CuO modified SnO 2 nanoparticles using fiber-optic sensor.* Sensors and Actuators B: Chemical, 2012. **169**: p. 199-207.
96. Neto, Á.C., et al., *Quality control of ethanol fuel: Assessment of adulteration with methanol using 1 H NMR.* Fuel, 2014. **135**: p. 387-392.
97. Omido, C., et al., *Quantification of water in ethanol using a photothermal transparent transducer.* Sensors and Actuators B: Chemical, 2013. **178**: p. 581-585.
98. Fujiwara, E., et al., *Real-time optical fibre sensor for hydro-alcoholic solutions.* Measurement Science and Technology, 2010. **21**(9): p. 094035.
99. Aziz, A., et al., *Silver/graphene nanocomposite-modified optical fiber sensor platform for ethanol detection in water medium.* Sensors and Actuators B: Chemical, 2015. **206**: p. 119-125.
100. Gallignani, M., et al., *A simple strategy for determining ethanol in all types of alcoholic beverages based on its on-line liquid–liquid extraction with chloroform, using a flow injection system*

and Fourier transform infrared spectrometric detection in the mid-IR. Talanta, 2005. **68**(2): p. 470-479.
101. Parke, S.A. and G.G. Birch, *Solution properties of ethanol in water.* Food Chemistry, 1999. **67**(3): p. 241-246.
102. Srivastava, S.K., R. Verma, and B.D. Gupta, *Surface plasmon resonance based fiber optic sensor for the detection of low water content in ethanol.* Sensors and Actuators B: Chemical, 2011. **153**(1): p. 194-198.
103. Omido, C.R., et al., *Water content in hydrated ethanol fuel measured by a photothermal chamber with a transparent transducer.* Fuel, 2015. **157**: p. 122-125.
104. Karapetyan, K., *Single optical microfibre-based modal interferometer*. 2012, Bonn University.
105. Yariv, A. and P. Yeh, *Photonics: Optical Electronics in Modern Communications*. 2007: Oxford University Press.
106. Huang, H. and U. Tata, *Simulation, implementation, and analysis of an optical fiber bundle distance sensor with single mode illumination.* Applied optics, 2008. **47**(9): p. 1302-1309.